HAL
open science

# Etude ultra-sensible en phase de nano-structures par interferométrie optique à balayage en champ proche

Jinmyoung Mok

## To cite this version:

Jinmyoung Mok. Etude ultra-sensible en phase de nano-structures par interferométrie optique à balayage en champ proche. Matériaux. Université de Bordeaux; Yonse Taehakkyo, 2015. Français. NNT : 2015BORD0086 . tel-01266058

**HAL Id: tel-01266058**

**https://theses.hal.science/tel-01266058v1**

Submitted on 2 Feb 2016

**HAL** is a multi-disciplinary open access archive for the deposit and dissemination of scientific research documents, whether they are published or not. The documents may come from teaching and research institutions in France or abroad, or from public or private research centers.

L'archive ouverte pluridisciplinaire **HAL**, est destinée au dépôt et à la diffusion de documents scientifiques de niveau recherche, publiés ou non, émanant des établissements d'enseignement et de recherche français ou étrangers, des laboratoires publics ou privés.

THÈSE EN COTUTELLE PRÉSENTÉE

POUR OBTENIR LE GRADE DE

# DOCTEUR DE

# L'UNIVERSITÉ DE BORDEAUX

# ET DE L'UNIVERSITÉ YONSEI

ÉCOLE DOCTORALE DES SCIENCES CHIMIQUES (Université de Bordeaux)

ÉCOLE DOCTORALE DE SCIENCES PHYSIQUE (Université Yonsei)

SPÉCIALITÉ : PHYSICO-CHIMIE DE LA MATIÈRE CONDENSÉE

Par Jinmyoung MOK

## Etude ultra-sensible en phase de nano-structures par interferométrie optique à balayage en champ proche

Sous la direction de M. Thierry CARDINAL et de M. Seung-Han PARK

Soutenue le : 26 mars 2015

Membres du jury :

| | | |
|---|---|---|
| M. CHO, Kyuman | Professeur, Université Sogang | Président |
| M. DUJARDIN, Christophe | Professeur, Université Lyon 1 | Rapporteur |
| M. KANG, Jin U. | Professeur, Université Johns-Hopkins | Rapporteur |
| M. CARDINAL, Thierry | Directeur de Recherche, CNRS, ICMCB, Bordeaux | Directeur |
| M. PARK, Seung-Han | Professeur, Université Yonsei | Directeur |
| M. PETIT, Yanick | Maître de Conférence, CNRS, ICMCB, Bordeaux | Invité |
| M. KIM, Duck Young | Professeur, Université Yonsei | Invité |

# RÉSUMÉ

## Etude ultra-sensible en phase de nano-structures par interferométrie optique à balayage en champ proche

In this thesis, near-field scanning optical interferometry (NSOI), which combines NSOM with interferometer, is proposed for the phase measurement. The shear-force detection scheme is applied for distance regulation. The hardware of the system is constructed by combining various electronic devices, and the operating software is coded by LabVIEW. Unwanted background signal is removed by simple calculation based on interference theory. By using this, the near-field optical measurement and the ultra-sensitive phase investigation of nano-materials are performed. 2D materials such as graphene and monolayer MoS2 are investigated. It is shown that atomic-scale thickness can be resolved by the NSOI. Especially, the grain boundaries of graphene and the seed of MoS2 can be found by phase detection. In addition, direct laser writing (DLW) on silver-containing glass is observed by using NSOM, and NSOI. For the first time, the writing threshold is correlatively observed in the fluorescence imaging and the near-field phase image.

**les mots clés:** Microscopie optique à balayage en champ proche, Interferométrie optique à balayage en champ proche, Mesure de phase, Différence de longueur de chemin optique (OPD), Materiaux 2D, Graphène, Joints de grains, Sisulfide de molybdène ($MoS_2$), Ecriture laser directe (DLW), Verres photosensibles de phosphate de zinc et d'argent, Cartographie confocale 2D résolue spectralement

## SUMMARY

# A study on ultra-sensitive phase in nano-structures by near-field scanning optical interferometry

In this thesis, near-field scanning optical interferometry (NSOI), which combines NSOM with interferometer, is proposed for the phase measurement. The shear-force detection scheme is applied for distance regulation. The hardware of the system is constructed by combining various electronic devices, and the operating software is coded by LabVIEW. Unwanted background signal is removed by simple calculation based on interference theory. By using this, the near-field optical measurement and the ultra-sensitive phase investigation of nano-materials are performed. 2D materials such as graphene and monolayer MoS2 are investigated. It is shown that atomic-scale thickness can be resolved by the NSOI. Especially, the grain boundaries of graphene and the seed of MoS2 can be found by phase detection. In addition, direct laser writing (DLW) on silver-containing glass is observed by using NSOM, and NSOI. For the first time, the writing threshold is correlatively observed in the fluorescence imaging and the near-field phase image.

**Key Words:** Near-field scanning optical microscope, Near-field scanning optical interferometer, Phase measurement, Optical path-length difference (OPD), 2D materials, Graphene, Grain boundary, Molybdenum disulfide ($MoS_2$), Direct laser writing (DLW), Silver-containing phosphate glass, Confocal 2D spectral mapping

# Etude ultra-sensible en phase de nano-structures par interférométrie optique à balayage en champ proche

## Introduction

L'observation d'objets de petite taille a toujours suscité l'intérêt des hommes et stimulé son imagination. Cette quête s'est naturellement immiscée dans le monde scientifique et a conduit à l'invention de microscopes toujours plus performants permettant de repousser les limites de l'infiniment petit. Le microscope optique a ainsi permis des avancées importantes dans différents domaines scientifiques. Ces microscopes basent leurs principes sur celui des lentilles et sont donc confrontés à la limite fondamentale de la diffraction de la lumière qui correspond de manière simplifiée à la moitié de la longueur d'onde. L'enjeu a ainsi été pour de nombreux chercheurs de dépasser cette limite. La microscopie électronique (à balayage et à transmission) permet d'atteindre des résolutions bien en dessous de celles fixées par les ondes électromagnétiques dans la gamme spectrale optique autour du visible. La résolution en microscopie électronique est ainsi très élevée mais certains désavantages apparaissent. Cette image par faisceau électronique ne donne pas d'information sur la réponse optique et procure des images en échelle de gris. L'échantillon peut également être dans certains cas modifié lors des procédés de préparation (dépôt d'une couche métallique par exemple). La microscopie à force atomique (AFM) permet de visualiser les surfaces avec une grande résolution latérale en détectant la force atomique entre une pointe et l'échantillon. Du point de vue optique, la microscopie confocale a permis d'améliorer la résolution sans contourner la problématique de la limite de diffraction. Depuis quelques années, des techniques comme la déplétion stimulée de l'émission (STED) font leur apparition pour améliorer la résolution spatiale de la mesure. La microscopie en champ proche s'est vite imposée comme une technique de choix permettant d'atteindre des résolutions optiques en dessous de la

longueur d'onde en associant simultanément une réponse optique et une information de la topologie de surface.

Les techniques de type « *near-field scanning optical microscopy* » « NSOM » se sont principalement intéressées à l'amplitude du signal optique. L'étude de la phase associée à l'onde optique est alors inaccessible, alors que celle-ci est cependant riche en information. En effet la mesure de la phase a joué un rôle important dans divers domaines. Cette information sur la phase modifiée par la propriété optique des matériaux (par exemple l'indice de réfraction) avec une résolution spatiale nanométrique peut être obtenue en combinant une imagerie de type NSOM avec des techniques interférométriques. Les premiers travaux ont été menés par Vaez-Iravani et Toledo-Crow en 1993. Ces dernières années, les travaux se sont beaucoup focalisés sur des structures métalliques [[Carney et al., 2012; Deutsch et al., 2008, 2010; Kihm et al., 2010; Kinzel et al., 2012; Schnell et al., 2010].

Dans cette thèse, un nouveau type de mesure de phase en champ proche intitulé NSOI (near-field scanning optical interferometer) est proposé, permettant de mesurer simultanément la topologie de surface, la phase et le signal en champ proche

Les systèmes d'imagerie optique présentent très généralement une résolution spatiale limitée par la diffraction de la lumière, de l'ordre de 0.61λ/N.A., typiquement. Parmi les techniques qui permettent de dépasser cette limite, l'imagerie en champ proche est une des plus importantes méthodes pour étudier les matériaux de dimensions nanométriques. Depuis le premier énoncé du concept de détection en champ proche par Synge, il s'est écoulé quasiment 60 ans avant la réalisation du premier instrument appelé microscope à balayage en champ proche (NSOM, pour l'acronyme en anglais). De nos jours, la technologie NSOM est largement employée dans différents domaines de recherche, et tout particulièrement en biologie et en plasmonique.

## Description des principaux travaux et résultats

La construction d'un NSOM, dans ce manuscrit de thèse, est décrite en détail. La combinaison du système NSOM construit avec un interféromètre est proposée afin d'accéder à des mesures de phase, à la fois de ultra-haute sensibilité mais également de très grande résolution spatiale. Le nom de l'instrument développé est un interferomètre optique à balayage en champ proche (NSOI, pour l'acronyme en anglais). Le principe est basé sur l'utilisation d'un diapason accordable en cristal de quartz, sur lequel se trouve une pointe, afin de sonder le matériau étudié. La mesure de la force de cisaillement de la pointe sonde au voisinage de la surface permet d'assurer la régulation et la stabilité de la distance de positionnement de la pointe par rapport à la surface considérée. Le dispositif est construit en combinant différents éléments électroniques pilotés par un logiciel développé en langage Lab-VIEW. Le bruit de la mesure en NSOI est supprimé par un calcul simple basé sur la théorie de l'optique ondulatoire et des interférences associées. Le système permet de réaliser des mesures optiques en champ proche ainsi que la détermination en haute résolution de la phase du champ optique. L'échantillon SNG01 (l'un des réseaux utilisés pour caractériser notre microscope à balayage en champ proche), ainsi que des disques optiques (CD, DVD and disques blu-ray) ont été utilisés pour tester la faisabilité et les performances de notre système.

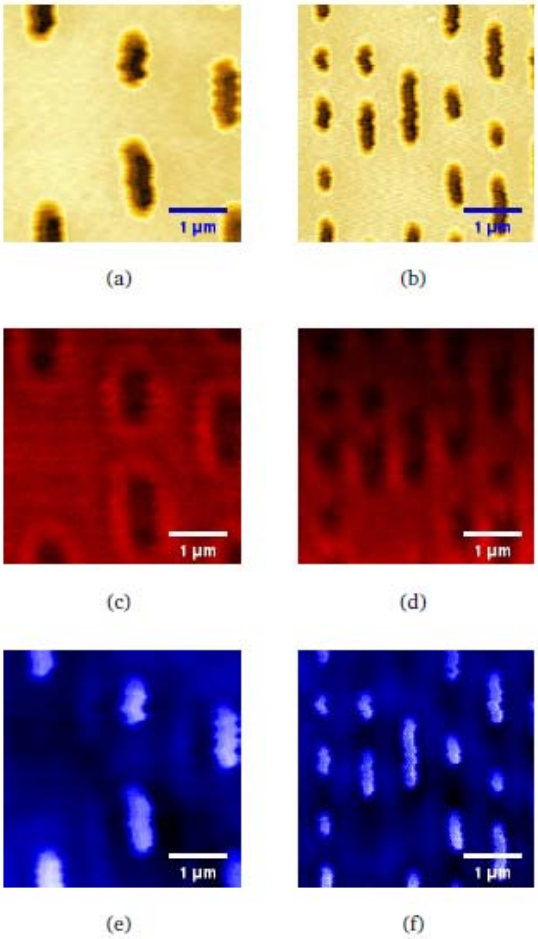


Figure 1 : Résultats obtenus sur CD et DVD, topologie de la surface d'un CD (a), et d'un DVD (b), Cellection d'image en mode NSOM d'un CD (c) et d'un DVD (d). Cartographies calculées de la phase obtenues sur Cd (e) et sur DVD (f).

Nous démontrons que le bruit instrumental qui entache la mesure est supprimé avec succès grâce à une méthode en 2 étapes que nous proposons. Les disques optiques transparents composés de polycarbonates seulement (sans le recouvement par une couche métallique) sont spécialement préparés pour l'étude en champ proche. Parmi ces disques, les disques blu-ray ont des dimensions caractéristiques inférieures à la limite de diffraction. Le motif d'une piste ne peut alors pas être résolu optiquement par des systèmes optiques conventionnels, dont la résolution est intrinsèquement limitée par la diffraction. Cependant,

une information optique résolue spatialement est obtenue grâce à notre approche par NSOI (figure 1). La mesure de traits de réseaux a notamment permis leur observation avec une excellente résolution, inférieure à 95 nm en profondeur.

Le graphène est un réseau bi-dimensionnel (2D), de type nid d'abeille, formé par des atomes de carbone et basé sur la forme simple des feuillets de graphite. A cause de sa structure de bandes électroniques très particulière (structure sans bande interdite), le graphène présente une très haute mobilité électronique, un fort module d'Young, une excellente conductivité thermique, ainsi que des propriétés optiques remarquables. Cependant, à cause de cette structure sans bande interdite, le graphène ne présente pas les caractéristiques d'un semi-conducteur mais celle d'un semi-métal. Ainsi, d'autres types de structures 2D, telles que les monocouches de disulfite de molybdène ($MoS_2$), attirent une très grande attention depuis quelques années. Il est attendu que les monocouches de $MoS_2$ soient utilisables en tant que transistors ou comme dispositifs photoélectriques, de par la nature de leur structure électronique à bande interdite.

Dans ce manuscrit de thèse, le graphène et les monocouches de $MoS_2$ sont étudiés par NSOI. Nous montrons qu'une épaisseur à l'échelle atomique peut être résolue par notre système NSOI, avec l'utilisation de l'algorithme de suppression du bruit de mesure. Les joints de grain du graphène sont observés à grande échelle, via la technique d'imagerie par collection en champ proche et par la réalisation de cartographies de phase. En particulier, les tensions internes à une couche de graphène sont observées, uniquement dans le cas d'une imagerie de phase.

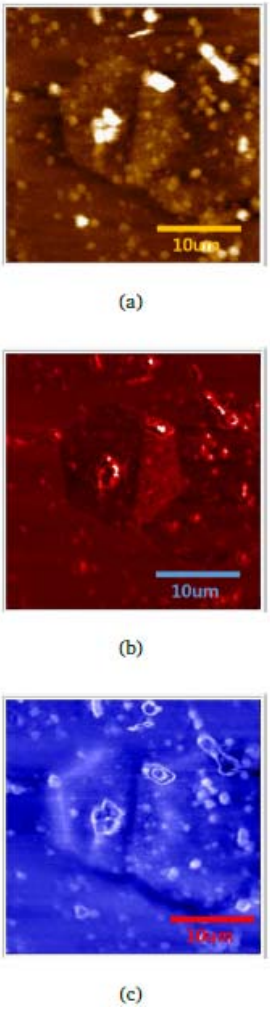


Figure 2 : Mesures obtenues sur un graphite oxydé : topologie de surface (a), Collection du signal par NSOM (b), et par cartographie de la phase (c)

Le vieillissement d'échantillons par immersion dans de l'acétone pendant quelques heures conduit à l'observation de modifications significatives des propriétés du matériau. Une forte réflectivité de flocons de forme hexagonale est observée, suite à ce procédé. Les positions au niveau desquelles 2 flocons se superposent sont étudiées à la fois par NSOM et par NSOI. Une forte transmission est alors observée dans la région du recouvrement. De plus, les images de phase permettent de discriminer quel flocon recouvre l'autre. En effet, sur la figure 2c, il est possible de distinguer clairement que le flocon de droite recouvre le flocon de

gauche. Enfin, il est tout à fait remarquable, dans le cas de $MoS_2$, d'observer le germe utilisé pour la croissance de la particule de $MoS_2$, grâce à la mesure en champ proche en phase. Ce germe n'est en effet pas détectable par des mesures topographiques de surface comme le montre la figure 2(b). De plus, des flocons de faible taille de $MoS_2$ peuvent être observés uniquement sur l'imagerie en champ proche.

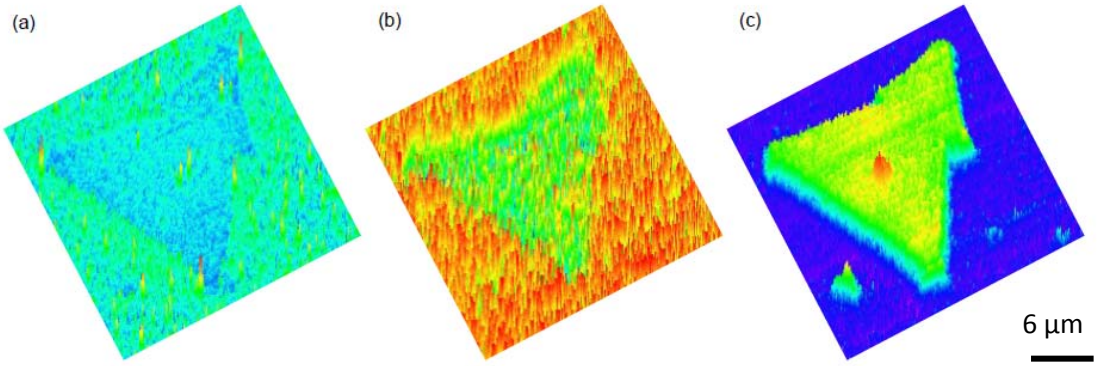


Figure 2 : Vue en 3 dimensions de la topologie de surface (a), en mode de collection NSOM (b) et en mode de détection de la phase (c) laissant apparaitre en rouge la localisation du germe utilisé pour la croissance d'une particule de $MoS_2$

La dernière partie de ce manuscrit de thèse porte sur l'écriture laser directe par laser femtoseconde (DLW, pour l'acronyme en anglais) dans des verres photosensibles non commerciaux, de type phosphates de zinc contenant des ions argent. Les propriétés de fluorescence du motif produit par écriture laser directe sont étudiées par microscopie confocale, et par des approches en super résolution de type NSOM et NSOI. Nous montrons que le mode par illumination en champ proche est plus adapté pour les études en fluorescence, dans notre cas. L'épaisseur des structures fluorescentes est mesurée par excitation NSOM. Les résultats montrent une amélioration par rapport aux mesures précédentes, avec des structures mieux résolues et donc avec des tailles plus fines des parois fluorescentes. Ainsi, des propriétés optiques sont mises en évidence au centre de la

structure fluorescente en forme d'anneau. Les variations de phase associées sont étudiées par NSOI. Pour la première fois, le seuil d'écriture laser est observé de façon corrélative, avec l'imagerie en fluorescence et avec l'imagerie de phase en champ proche. A partir de ce résultat, nous démontrons que le profil de phase est bien relié à la modification des densités de charges et à la création de nouvelles espèces chimiques, en particulier les agrégats d'argent fluorescents qui produisent les anneaux de fluorescence (cf figure 3). Finalement, ceci met en évidence que les profils de phase ne présentent pas de contribution dominante issue d'un effet électrooptique statique, de type effet Kerr, qui serait induit par le très fort champ électrique statique et permanant qui se trouve piégé dans le matériau suite à l'écriture laser femtoseconde dans ces verres photosensibles à l'argent.

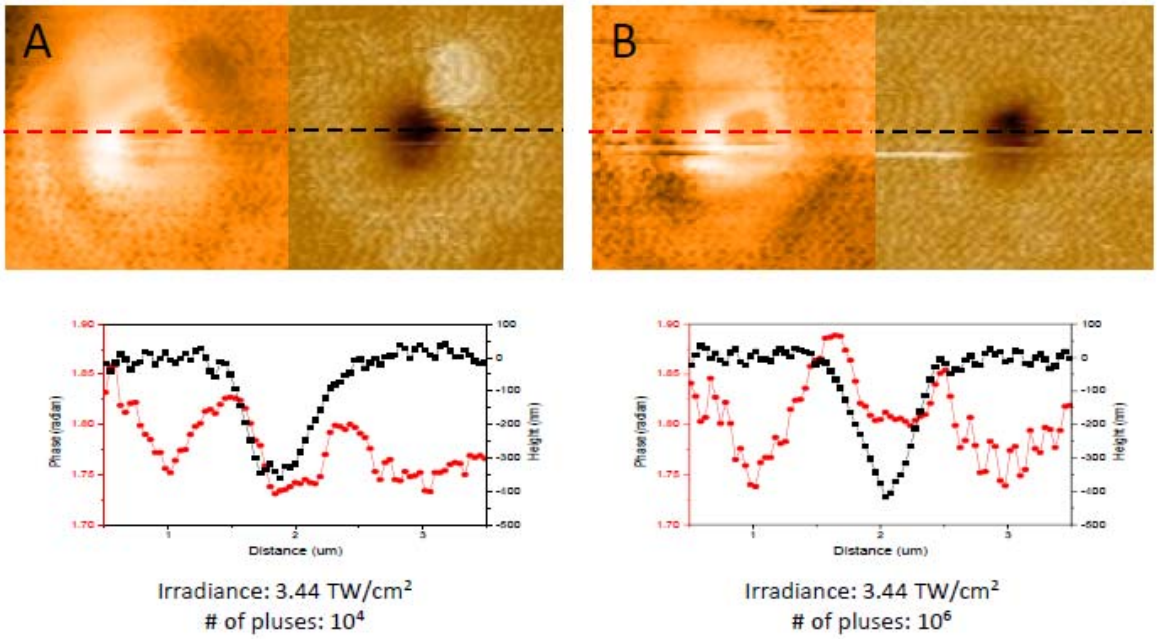


Figure 3 : Section de la structure annulaire produite par irradiation laser femtoseconde au sein d'un verre phosphate de zinc et d'argent pour une même irradiance par impulsion et respectivement l'accumulation de $10^4$ impulsions et $10^6$ impulsions. La courbe noire représente la topologie de surface et la courbe rouge le profil de la phase le long de la section de la structure

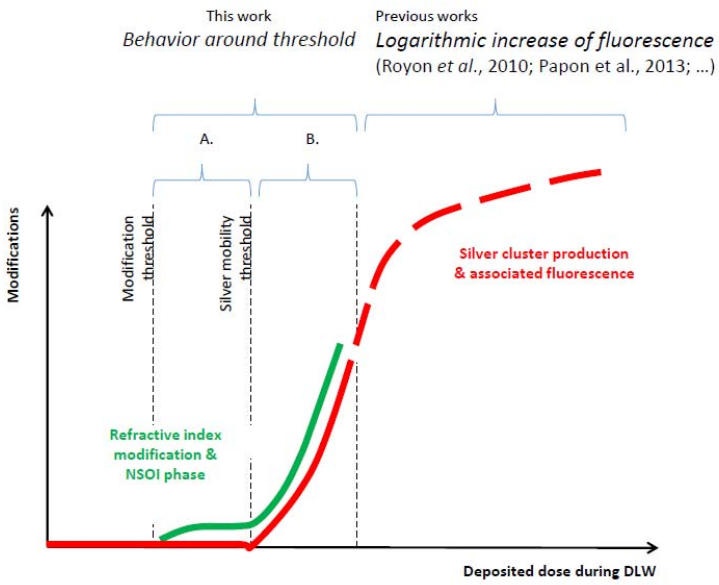


Figure 4 : Modification de la phase associée à la variation de l'indice de réfraction et modification des propriétés de luminescence en fonction de la dose déposée

Les travaux permettent de montrer que la variation de la phase apparait préalablement à la modification des propriétés locales de luminescence en fonction de la dose déposée par l'irradiation laser femtoseconde. La formation de l'anneau luminescent est donc un processus qui intervient après la séparation des charges, l'établissement d'un signal non linéaire d'ordre deux et la variation de la phase et de l'indice de réfraction.

## Conclusion

La technique NSOI combinant la technique NSOM et l'analyse de la phase offre une nouvelle technique ultra-sensible de haute résolution. Elle permet d'apporter de nouvelles informations sur la structure et la morphologie des matériaux. Cette technique NSOI est prometteuse pour l'étude de nano-matériaux et matériaux nano-structurés présentant des motifs optiques difficilement décelable par d'autres techniques.

En termes de perspectives, la thèse démontre que la technique NSOI ouvre la voie à des approches corrélatives en imagerie super résolue. Elle procure des informations optiques inédites sur différents types de matériaux. Cette technique pourrait bénéficier d'évolutions comme la combinaison de différentes longueurs d'onde, le contrôle de la polarisation ou elle pourrait également combiner d'autres techniques optiques comme la détection photo-acoustique, la mesure d'harmoniques élevées.

# ABSTRACT

## A study on ultra-sensitive phase in nano-structures by near-field scanning optical interferometry

Optical imaging system is restricted by diffraction limit around $0.61\lambda/\mathrm{N.A.}$. Among the various attempts to break this limit, near-field imaging is one of the most important methods to investigate nano-scale materials. Since the first proposal about near-field detection by Synge, it took almost 60 years to construct a real instrument called near-field scanning optical microscope (NSOM). Nowadays, NSOM is widely employed to research on various fields, especially, biology and plasmonics.

In this thesis, the construction of NSOM is described in detail, and combining NSOM with interferometer is proposed for the phase measurement. The name of this instrument is near-field scanning optical interferometer (NSOI). The shear-force detection scheme by using a quartz crystal tuning fork is applied for distance regulation between a probe tip and a sample surface. The hardware of the system is constructed by combining various electronic devices, and the operating software is coded by LabVIEW. Unwanted background signal is removed by simple calculation based on interference theory. By using this, the near-field optical measurement and the ultra-sensitive phase investigation of nano-materials are performed. Optical path-length difference (OPD) is selected for illustrating *figure of merit* to the system.

SNG01 (one of test gratings for SPM) and optical discs (CD, DVD and blu-ray disc) are selected to test the feasibility. It is demonstrated that unwanted background

signal from SNG01 sample is successfully removed by proposed 2-step scanning method. Bare transparent optical discs composed of only polycarbonate (not coated by metallic layer) are specially prepared. Among the optical discs, blu-ray disc has sub-diffraction limit pattern. The track pitch cannot be resolved by conventional diffraction limited system. However, highly resolved optical information is obtained by using the NSOI. High depth resolution better than 95 nm in the view point of OPD can be achieved.

Graphene is a two-dimensional (2D) honeycomb lattice structure based on carbon atoms and a basic form of graphitic materials. Because of the special (band-gapless) electronic band structure, graphene shows extremely high electron mobility, high Young's modulus, and thermal conductivity, including interesting optical features. However, because of the gapless structure of graphene, it does not show semi-conducting characteristics but semi-metallic properties. Therefore, another kinds of 2D materials such as monolayer molybdenum disulfide ($MoS_2$) attracted much attention in recent years. It is expected that monolayer $MoS_2$ can be applied to transistor and photoelectric devices because of its direct band-gap nature.

In this thesis, graphene and monolayer $MoS_2$ are investigated by the NSOI. It is shown that atomic-scale thickness can be resolved by the NSOI with background removing algorithm. Grain boundaries in large-scale graphene are observed in near-field collection image and phase map. Especially, the internal stress in graphene layer is found only in the phase map of partially-grown graphene. When aged graphene is immersed into acetone for few hours, its dramatic property change is observed. High reflection of hexagonal shape flakes is observed from this process. The position, which two flakes are overlapped, is investigated by both NSOM and NSOI. The high transmission is observed in the overlapped region. Moreover, the phase images provide the information when a flake covers the other one. Above all, in $MoS_2$ case, the seed is observed in near-field optical signal and phase, which can not be found in

surface topography. In addition, some small-size $MoS_2$ flakes can be observed only by the phase map.

The end of the thesis deals with direct laser writing (DLW) on silver-containing glass. Fluorescence and phase properties of DLW glass pattern are investigated by using confocal spectroscope, NSOM, and NSOI. The fluorescence are measured by illumination and collection mode NSOM. It is shown that the illumination mode is suitable for fluorescence study. The thickness of the fluorescence wall is obtained by NSOM excitation. The thickness of the fluorescence wall is not thin as expected, but the optical property change is identified in the center of the ring pattern. The phase variation is investigated by using NSOI. For the first time, the writing threshold is correlatively observed in the fluorescence imaging and the near-field phase image. From the result, it is demonstrated that the phase profile is related to the modifications of charge densities and new chemical species. Finally, this highlights that these phase profiles do not show predominant static Kerr-like electro-optic effects induced by the buried static electric field that results from DLW in these glasses.

# 국 문 요 약

## 근접장 주사 광학 간섭계를 이용한 나노 구조의 고감도 위상 연구

광학적인 이미징 시스템은 회절에 의해 $0.61\lambda/\mathrm{N.A.}$ 이상의 분해능을 가질 수 없다. 이 한계를 넘어서기 위한 다양한 시도 중, 근접장 이미징은 다양한 분야에서 활용되고 있는 중요한 기술이다. 처음 Synge가 근접장 측정 방법을 제안한 이후, 60여년이 지나서야 근접장 주사 광학 현미경(NSOM)이라는 실제 측정 장비가 개발되었다. 현재 NSOM은 다양한 분야의 연구에서 중요하게 사용되고 있으며, 특히 생물학과 플라즈모닉스 영역에서 그 역할이 더욱 중요해지고 있다.

이 학위논문에서는, NSOM을 구성하는 과정에 대해 자세히 기술하고, NSOM과 간섭계를 결합하여 위상 정보를 측정할 수 있는 방법을 제안한다. 이 장비의 이름을 근접장 주사 광학 간섭계(NSOI)라고 명명하였다. 측정용 탐침과 시료 간의 거리 조절을 위해서 수정진동자를 이용한 근접 저항력 측정 기술을 사용하였다. 여러 가지 전자 장비를 결합하여 시스템의 하드웨어를 구축하였고, LabVIEW를 이용하여 제어를 위한 소프트웨어를 작성하였다. 그리고 기본적인 간섭 이론을 이용한 간단한 계산을 통해 위상 신호에 포함된 배경 신호를 제거하는 방법을 설명하였다. 이를 이용하여 다양한 나노 물질에 대해 근접장 광학 정보 및 고감도 위상 신호에 대한 연구를 진행하였다. 이 새로운 장비의 성능 지수로는 광학 거리 차(OPD)를 사용하였다.

장비의 타당성을 확인하기 위해 SNG01(SPM 시험용 회절격자)과 다양한 광학 디스크(CD, DVD, blu-ray disc)에 대한 위상 신호 측정을 진행하였다. SNG01의 결과로부터, 이 논문에서 제안한 2단계 주사 방식을 이용하면 불필요한 배경 신호를 성공적으로 제거할 수 있음을 확인할 수 있었다. 광학 디스크는 특별히 금속 반사막이 코팅되기 전

폴리카보네이트만으로 이루어진 투명한 시료를 준비하였다. 이 중, 블루레이 디스크는 회절 한계보다 작은 무늬를 가지고 있기 때문에, 회절에 의해 분해능이 제한되는 일반적인 광학 시스템으로는 무늬를 구분해 낼 수 없다. 하지만 NSOI를 이용하여 고분해능 광학 정보를 구할 수 있었다. 이 결과를 통해, 이 논문에서 제안된 시스템이 95 nm OPD 이상의 분해능을 가진다는 것을 확인할 수 있었다.

그래핀은 탄소 원자로 이루어진 벌집모양의 2차원 구조로, 다른 흑연 계열 물질의 기본 형태가 된다. 에너지 틈이 없는 특수한 전자 띠구조 때문에, 그래핀은 뛰어난 전자 이동도, 영의 탄성 계수, 열 전도성을 보이며, 특별한 광학적 성질을 가진다. 하지만 에너지 틈이 없기 때문에, 그래핀은 반도체적인 특성이 아닌 준금속의 특성을 보인다. 따라서 최근에는 단층 이황화몰리브덴($MoS_2$)과 같은, 그래핀 이외의 2차원 물질에 대한 연구 역시 주목받고 있다. 단층 이황화몰리브덴($MoS_2$)은 직접 에너지 틈(direct band-gap)을 가지고 있기 때문에 트랜지스터나 광전소자에 적용될 수 있을 것으로 기대된다.

이 학위논문에서는, NSOI를 이용하여 그래핀과 단층 이황화몰리브덴에 대한 연구를 진행하였다. 이를 통해, 배경 신호 제거 알고리즘을 적용한 NSOI를 이용하여 원자 수준의 두께를 갖는 물질을 성공적으로 구분해 낼 수 있음을 보였다. 대면적 그래핀에 존재하는 결정경계(結晶境界, grain boundary)를 근접장 이미지와 위상 이미지에서 관찰할 수 있었으며, 특히 그래핀 내부적인 스트레스는 위상 이미지에서만 발견할 수 있었다. 또한, 제작 후 오랜 시간이 지난 그래핀 시료를 아세톤에 수 시간 담근 후, 특성 변화를 관찰하였다. 이 과정에서 반사율이 높은 육각형 모양 조각들을 발견하였다. 이 중 두 개의 조각이 겹쳐진 부분에 대해 NSOM과 NSOI를 이용하여 관찰하였고, 겹쳐진 영역에서 큰 투과율을 확인할 수 있었다. 그리고 어떤 조각이 다른 조각을 덮고 있는지를 위상 이미지를 통해 확인할 수 있었다. 무엇보다도, 이황화몰리브덴($MoS_2$)의 경우, 표면 신호에서는 볼 수 없던 시드(seed)를 근접장 광학 신호와 위상에서 관찰할 수 있었다. 또한 위상 결과에서만이 작은 크기의 이황화몰리브덴 조각을 구별해 낼 수 있었다.

학위논문의 마지막은 은을 포함하는 유리에 레이저로 무늬를 새긴 물질에 대해 다루었다(DLW). 공초점 분광기, NSOM, NSOI를 이용하여 DLW 유리에 대한 형광과 위상 특성 측정을 진행하였다. NSOM의 두 가지 모드(illumination mode and collection

mode)를 이용하여 형광 이미지를 측정하였으며, illumination 모드가 형광 분석에 더 적합함을 확인하였다. 이를 통해 형광을 발하는 벽의 두께를 구했다. 형광 벽의 두께는 기대한 것만큼 얇지 않았지만, 링 무늬 중앙에서 광학적 특성의 변화를 확인했다. 위상 변화는 NSOI를 통해 측정하였다. 우선, 형광과 근접장 위상 이미지 사이에 상관관계를 갖는 쓰기 역치를 관측하였다. 이러한 결과로부터, 위상 변화가 전하 밀도 및 새로운 화학적 물질의 생성과 연관되어 있음을 확인하였다. 이는 결과적으로, DLW에 의해 유리 내부에 생성된 정전계(buried static electric field)가 유도하는 커(Kerr) 효과와 같은 정적 전기 광학 효과가 위상 변화의 주요한 원인이 아니라는 것을 나타낸다.

**핵심되는 말:** 근접장 주사 광학 현미경, 근접장 주사 광학 간섭계, 위상 측정, 광경로차, 2차원 물질, 그래핀, 결정경계(結晶境界), 이황화 몰리브덴, 직접 레이저 쓰기, 은을 포함하는 인(燐) 유리, 공초점 2차원 분광 매핑

# 감사의 글

## Acknowledgements

새로운 천년을 맞이할 때 즈음 대학에 들어와 어느 덧 14년, 대학원에 진학한 후 7년 반 이라는 시간이 흘렀습니다. 어쩌면 인생의 가장 찬란한 한 때였을지 모를 지난 7년을 뒤돌아보면, 주위의 많은 분들의 도움으로 무사히 학위과정을 마칠 수 있었음을 느낍니다.

가장 먼저 학위과정 중 아무것도 모르던 저를 세심히 지도해 주신 박승한 교수님께 감사의 말씀을 드립니다. 교수님의 가르침으로 이제 겨우 한 사람의 몫을 할 수 있게 된 것 같습니다. 또한, 부족한 논문이지만 기꺼이 심사해 주시고 조언해 주신 장수경 교수님과 김덕영 교수님께도 감사의 말씀을 드립니다. 그리고 공동학위과정을 진행하는 동안 저를 지도해주시고, 프랑스에서 연구를 진행할 때부터 한국에서 돌아와서까지 항상 신경써주시고 조언해주신 프랑스 보르도 ICMCB의 Thierry Cardinal 박사님과 Yannick Petit 박사님께도 이 자리를 빌려 감사의 마음을 전합니다. Je souhaite remercier à Docteur. Thierry Cardinal et Docteur. Yannick Petit de l'Institut de Chimie et de la Matière Condensée de Bordeaux (ICMCB) pour luer soutien et luer générosité.

처음 연구실에 들어왔을 때 뵈었던 제구출 교수님과 임상엽 박사님부터 김경환 박사님, 김대근 박사님, 이규승 박사님, 김재혁 박사님, 정은희 박사님, 김대규 박사님, 이응장 박사님, 안홍규 예비 박사님, 성수 형, 기혁이 형, 호찬, 강열, 가영, 영은이 형, 경석이 형, 성호, 보람, 창현, 대연, 유미, 모두에게 감사의 말을 전합니다. 정말 좋은 사람들과 함께 할 수 있어서 영광이었습니다. 그리고 새로 들어온 영민, 희승, 시영, 열심히 해서 좋은 결과 있기 바라요. 사무 일을 맡아서 해주었던 혜진, 성희, 그리고 학부 때부터 지금까지 물리학과 사무실을 지켜주신 장현아 씨, 고맙습니다.

무엇보다도 저의 학위기간동안 물심양면으로 저를 지원해준 사랑하는 나의 가족, 아버지, 어머니, 그리고 내 동생 진원이, 항상 고맙고 사랑합니다. 제 가족은 항상 저에게 앞으로 나아갈 수 있는 힘이 되어 주었고, 필요할 때 쉴 수 있는 그늘이 되어 주었습니다.

그리고 10년간 내 옆을 지키며 연구한다는 이유로 잘 만나지도 못했던 나를 항상 응원해준 현진에게 고맙다는 말을 전하며 감사의 글을 맺을까 합니다.

2015 년 1 월 어느 늦은 저녁에,

목진명 드림.

# Contents

**RÉSUMÉ** . . . . . **i**

**SUMMARY** . . . . . **iii**

**RÉSUMÉ SUBSTANTIEL** . . . . . **v**

**ABSTRACT** . . . . . **ix**

**국 문 요 약** . . . . . **xiii**

**Acknowledgements** . . . . . **xvii**

**Contents** . . . . . **xix**

**List of Figures** . . . . . **xxiii**

**List of Tables** . . . . . **xxxi**

**Abbreviations** . . . . . **xxxiii**

**1 Introduction** . . . . . **1**

1.1 History of Near-field Optics . . . . . 1

1.2 What is “Near-field Optics”? . . . . . 6

1.2.1 Diffraction Limited System . . . . . 6

1.2.2 Far-field Optics (Classical Optics) . . . . . 11
1.2.3 Near-field Optics . . . . . 12
1.3 Near-field Scanning Optical Interferometer . . . . . 15
1.4 Thesis Scope . . . . . 17

**2 Experimental System and Operation Program . . . . . 19**
2.1 Introduction . . . . . 19
2.1.1 Distance Regulation Method: Shear-force Detection . . . . . 20
2.2 Composition of NSOM Unit . . . . . 22
2.2.1 Components . . . . . 22
2.2.2 Characteristic Curve Measurement for Tuning Fork Distance Regulation Sensor . . . . . 29
2.3 Operating Program . . . . . 32
2.3.1 Initializing . . . . . 32
2.3.2 Tip Calibrating . . . . . 34
2.3.3 Approaching . . . . . 36
2.3.4 Scanning . . . . . 38
2.3.5 Ending . . . . . 42
2.4 Reference Sample . . . . . 44
2.5 Summary . . . . . 46

**3 Near-field Scanning Optical Interferometer . . . . . 47**
3.1 Introduction . . . . . 47
3.2 Near-field Scanning Optical Interferometer . . . . . 50
3.2.1 Setup . . . . . 50
3.3 Removing Background Signal . . . . . 53
3.3.1 Removing Background Signal . . . . . 53
3.3.2 LabVIEW Program . . . . . 57

3.3.3 Two Examples Which Can Make Phase Difference . . . . . 57
3.4 Test for the Algorithm: Reference Sample and Optical Discs . . . . . 61
3.4.1 SNG01 . . . . . 61
3.4.2 Bare Transparent Optical Discs . . . . . 65
3.5 Summary . . . . . 79

**4 Near-field Investigation of 2-Dimensional Nanomaterials . . . . . 81**
4.1 Introduction . . . . . 81
4.2 Electronic State of Graphene: Tight-Binding Model . . . . . 85
4.3 Phase Measurement for 2-dimensional Nanomaterials . . . . . 91
4.3.1 Graphene . . . . . 91
4.3.2 Molybdenum Disulfide . . . . . 99
4.4 Summary . . . . . 102

**5 Localized Fluorescence and Phase Analysis of DLW Ag Structure . . . . 105**
5.1 Introduction . . . . . 105
5.1.1 Sample Preparation . . . . . 109
5.1.2 Spectral Properties . . . . . 112
5.2 2D Spectral Mapping by using Confocal Spectroscope . . . . . 114
5.2.1 Instrument . . . . . 115
5.2.2 Confocal Spectral Mapping . . . . . 117
5.3 NSOM & NSOI Measurement . . . . . 125
5.3.1 Near-field Fluorescence Image . . . . . 125
5.3.2 Near-field Phase Properties . . . . . 133
5.4 Summary . . . . . 146

**6 Conclusion . . . . . 149**

**Bibliography . . . . . 153**

**Appendix A Bessel function . . . . . 165**

# List of Figures


1-1 Original concept of near-field scanning optical microscope . . . . . 4

1-2 Image formation for diffraction grating . . . . . 6

1-3 Diffraction geometry of an opening aperture . . . . . 8

1-4 Rayleigh criterion . . . . . 11

1-5 Various modes of NSOM operation . . . . . 13

2-1 The concept of distance regulation by using shear force detection . . 21

2-2 The flowchart of electrical signals between the components of NSOM unit . . . . . 23

2-3 Picture of NSOI setup . . . . . 24

2-4 NSOM head . . . . . 24

2-5 Resonance curve of tuning fork with fiber probe. The resonance frequency: 32.269kHz, Q-factor: 3256 . . . . . 30

2-6 Initializing part of operation program. . . . . 33

2-7 Tip calibrating part of operation program . . . . . 35

2-8 Approaching part of operation program . . . . . 37

2-9 Scanning part of operation program . . . . . 39

2-10 (a) Basic principle to tilt the scanning angle. (b) Tilt scanning test for CD surface. . . . . 40

2-11 Ending part of operation program . . . . . 43

2-12 Surface topography for the standard samples: (a) TGQ1 (b) TGX01P (c) Cross section for TGQ1 (d) Cross section for TGX01P . . . . . 45

3-1 Schematic diagram of near-field scanning optical interferometry . . . 51

3-2 Basic concept to remove background signal . . . . . 53

3-3 Phase extraction program constructed by using LabVIEW programming language . . . . . 58

3-4 Two examples to make phase variations. (a) Constant refractive index with different depth and (b) constant depth with different refractive index. . . . . 59

3-5 Surface topography of SNG01 achieved by AFM . . . . . 62

3-6 Surface topography of SNG01 achieved by NSOM . . . . . 63

3-7 The results of NSOI measurement and phase extraction. (a) Surface topography. (b) NSOI measurement. (c) Back ground measurement. (d) Cosine of phase . . . . . 64

3-8 Optical disc fabrication process . . . . . 66

3-9 Optical microscope image of (a) CD and (b) DVD. Objective Lens: 40 ×. . . . . 69

3-10 AFM image of (a) CD and (b) DVD. And the cross section of (c) CD and (d) DVD. The depth of each pit (height difference between red arrows) are 105.3 nm and 114.9 nm for CD and DVD. And the track pitches (distance between green arrows) are 1600 nm and 760 nm. . 70

3-11 SEM images of (a) CD and (b) DVD from the top. SEM cross-section images of (c) CD and (d) DVD. . . . . 71

3-12 NSOI results of CD and DVD. Surface topographies of (a) CD and (b) DVD. Collection mode NSOM images of (c) CD and (d) DVD. Calculated phase maps of (e) CD and (f) DVD. . . . . 73

3-13 Optical microscope image of Blu-ray disc. Objective Lens: 40 $\times$. . . . 75

3-14 (a) AFM image and (b) the cross section of a blu-ray disc. (c) SEM image (top view) and (d) SEM cross section of a blu-ray disc. . . . . 76

3-15 NSOI results of blu-ray disc. (a) Surface topography, (b) collection mode NSOM image and (c) calculated phase map. . . . . 78

4-1 "Mother of all graphitic forms" [Geim and Novoselov, 2007]. . . . . 82

4-2 Three-dimensional representation of the atomic structure of $MoS_2$ [Radisavljevic et al., 2011]. . . . . 84

4-3 (a) A graphene lattice. The sublattices are distinguished by red and blue dots. (b) Reciprocal lattice. . . . . 85

4-4 (a) Band structure of graphene. (b) Cross-section of (a) in direction from $\Gamma$ to K point. Nearest-neighbor hopping with parameter $t = 3.033$ eV, nearest-neighbor overlap parameter $s_0 = 0.129$ and orbital energy $\epsilon_{2p_z} = 0$. . . . . 90

4-5 Graphene transfer process . . . . . 92

4-6 Measured results for fully grown graphene. (a) Surface topography, (b) NSOM collection signals and (c) phase variation. . . . . 93

4-7 Measured results for partially-grown graphene. (a) Surface topography and (b) the cross-sectional view, (c) NSOM collection signals and (d) the cross-sectional view, (e) phase variation and (f) the cross-sectional view. . . . . 95

4-8 Image of graphite oxide with (a) reflection and (b) transmission type microscopy. . . . . 97

4-9 Measured results for graphite oxide. (a) Surface topography, (b) NSOM collection signals and (c) phase variation. . . . . 98

4-10 3D view of (a) surface topography, (b) NSOM collection signals and (c) phase variation of $MoS_2$. . . . . 99

4-11 Measured results for $MoS_2$. (a) Surface topography, (b) NSOM collection signals and (c) phase variation. (d, e, f) are the cross-sectional view of (a, b, c) for the dotted-line. . . . . 101

5-1 Schematic view of the nanostructures formation when DLW is performed in a Ag-containing glass [Bellec et al., 2009]. . . . . 106

5-2 Transverse spatial distributions of fluorescence and EFISHG profiles across the structure [Papon et al., 2013]. . . . . 107

5-3 Correlative EFISHG and fluorescence relative intensities versus DLW incident fluence for $1.1 \times 10^5$ laser pulses (speed of 180 $\mu$m.s$^{-}$1). EFISHG shows a threshold behavior between 3 and 3.5 J/cm$^2$, a very steep increase followed by a plateau above 4 J/cm$^2$ corresponding to the saturation of the buried static electric field [Papon et al., 2013]. . 108

5-4 Sketch of build-up mechanisms, consisting first in a net space charge separation with a saturation plateau, subsequently followed by the growth and stabilization of silver fluorescent clusters with no visible saturation plateau here. We depict the electric field driven growth of silver clusters, and their reduction/oxidation stabilization with the associated electric potential [Papon et al., 2013]. . . . . 109

5-5 Fluorescence image of the directly laser written glass. Microscope: *Olympus* IX71, Objective: (top) UApo/340, 20 $\times$, N.A. - 0.75 and (bottom) LMPlanFI, 100 $\times$, N.A. – 0.80. Excitation source: xenon (Xe) lamp. Fluorescence filter cube: U-MNV2. . . . . 111

5-6 Fluorescence image of the sample by using confocal microscope with oil immersion lens (63 $\times$, NA – 1.4) . . . . . 112

5-7 Normalized fluorescence spectra with ultra-violet and violet excitation, the short-wavelength part of each plot being affected by the cut-off transmission of the respectively used emission filters. . . . . 113
5-8 Confocal principle . . . . . 114
5-9 Schematic diagram for the confocal spectroscope (*Horiba* LabRAM HR800). BF: bandpass filter, NF: neutral density filter, M: mirror, DM: dichroic mirror, OL: objective lens, EF: emission filter. . . . . 115
5-10 (a) Fluorescence spectrum of $Mn^{2+}$ and (b) its correction factors. (c) Fluorescence spectrum of $Cu^{+}$ and (d) its correction factors. In (a) and (c), red lines represent the reference spectrum and black lines are measured one. . . . . 116
5-11 Fluorescence spectrum of the ring shape being excited at 405 nm, measured with the confocal micro-spectrometer (black line) and the related calibrated spectrum (red line). . . . . 117
5-12 (a) 2D fluorescence mapping near fluorescence peak ($\sim$ 500 nm) of the pattern which exists inside of the glass excited at 405 nm and related cross-sections of (a) in (b) horizontal and (c) vertical direction. 50 $\mu$m pinhole is used for mapping. . . . . 119
5-13 (a) 2D fluorescence mapping of the pattern near fluorescence peak ($\sim$ 500 nm) of the pattern which exists inside of the glass excited at 405 nm and related cross-sections of (a) in (b) horizontal and (c) vertical direction. 50 $\mu$m pinhole is used for mapping. . . . . 120
5-14 The different spectra excited at 405 nm, for each position, to generate the fluorescence map of Figure 5-12. . . . . 121
5-15 Localized spectra for fluorescence with excitation at 405 nm. (a) Selected points and (b) related normalized spectra. . . . . 123
5-16 Shapes of (a) thermally-pulled and (b) chemically-etched fiber tips . 127

5-17 NSOM setup for illumination and collection modes. LD: laser diode, OL: objective lens, LPF: long pass filter. . . . . 128

5-18 Near-field images of the ring-shape fluorescence pattern by (a) collection and (b) illumination modes. . . . . 129

5-19 Schematic of multiple reflections of fluorescence at the end of the chemically-etched fiber tip. . . . . 130

5-20 NSOM setup for illumination mode. LD: laser diode, OL: objective lens, LPF: long pass filter. . . . . 131

5-21 Near-field images and line profiles with 405 nm LD (a), (b) and 632.8 nm He-Ne laser (c), (d). These results show that the fluorescence only occurs at 405 nm excitation . . . . . 132

5-22 Z-stack confocal images of the ring structure, excited at 405 nm, where Z=0 corresponds to the sample's surface while positive Z values correspond to focusing conditions inside the glass sample. . . . . 134

5-23 The fluorescence image of the glass using confocal microscope and optical microscope image. The excitation source for confocal image is 405 nm LD. . . . . 137

5-24 The 2D near-field mapping of phase distribution (left) and of the surface topography (right) of the structured glass. . . . . 139

5-25 1D horitzontal cross-sections of the 2D mapping the structured glass, showing depth (black squares) and phase (red dots) line profiles. A, B, C and D represents the same characters in Figure 5-24 . . . . . 141

5-26 Evolution of the laser-induced phase modification versus incident irradiances, for the 3 different numbers of cumulated pulses and the associated average phase plot. Note that the profile of the phase modification differs at the irradiance threshold of 2.64 TW/cm$^2$, above which the phase profile becomes annular, similarly to the profile of the fluorescent ring structures. . . . . 142

5-27 Evolution of the laser-induced mean phase modification (see Figure 5-26) and related fluorescent intensity versus incident irradiances. Note the correlation of the irradiance threshold around 2.64 TW/cm$^2$, above which the fluorescence intensity significantly grows while both phase and fluorescence profiles show an annular ring. . . . . 143

5-28 Sketch of the modification mechanisms for DLW at the sample's surface, consisting first in a bell-shaped modification without significant ionic mobility (area A.), and second in an annular-shaped modification where phase modifications are dominated by the creation of silver clusters related to the thermal activation of the ionic mobility (area B.), while the bell-shape contribution decreases due to such ionic motions. . . . . 145

# List of Tables

1.1 High-resolution microscopy methods . . . . . 3

1.2 Location of maxima and minima of the Airy pattern [Goodman, 2004]. 10

2.1 The configuration of 16-pin adapter [Lee, 2013] . . . . . 25

3.1 Specification of optical discs . . . . . 68

5.1 Conversion of laser writing conditions from applied voltages to focused irradiances . . . . . 135

# Abbreviations

**2D** Two-dimensional

**3D** Three-dimensional

**AC** Alternating current

**ADC** Analog-to-digital converter

**AFM** Atomic force microscope

**ANSOM** Apertureless near-field scanning optical microscope

**CD** Compact disc

**CLSM** Confocal laser scanning microscope

**CMOS** Complementary metal–oxide–semiconductor

**CNT** Carbon nanotube

**CVD** Chemical vapor deposition

**DAC** Digital-to-analog converter

**DAQ** Data acquisition

**DC** Direct current

**DVD** Digital video disc

**DLW** Direct laser writing

**EFISHG** Electric field induced second-harmonic generation

**FWHM** Full-width at half-maximum

**GPIB** General purpose interface bus

**HD** High-definition

**IR** Infra-red

**LD** Laser diode

**MWNT** Multi-wall nanotube

**N.A.** Numerical aperture

**ND** Neutral density

**NSOI** Near-field scanning optical interferometer

**NSOM** Near-field scanning optical microscope

**OPD** Optical path-length difference

**PALM** Photo activated localization microscopy

**PD** Photo-diode

**PI feedback** Proportional-integral feedback

**PMMA** Polymethyl methacrylate

**PMT** Photo-multiplier tube

**SEM** Scanning electron microscope

**SHG** Second-harmonic generation

**SIM** Structured illumination microscopy

**S/N** Signal-to-noise

**SPM** Scanning probe microscope

**SPP** Surface plasmon polariton

**STED** Stimulated emission depletion

**STM** Scanning tunneling microscope

**STORM** Stochastic optical reconstruction microscopy

**SWNT** Single-wall nanotube

**TEM** Transmission electron microscope

**UI** User interface

**UV** Ultra-violet

# Chapter 1

# Introduction

## 1.1 History of Near-field Optics

Small objects have been always interesting subjects to human beings and stimulated one's imagination. People's interest to these *minikins* may come from simple curiosity but makes great scientific progress. Since mankind wants to see what he can not see, an instrument called *Microscope* was invented. Later, people developed this instrument to overcome such a human limitation. After the first conventional optical microscope was invented, it has been playing an important role in various scientific research fields. Fundamentally, conventional microscope is based on optical lens system. However, the resolution of lens-based optical microscope system is essentially limited by diffraction, which is about a half of wavelength.

A lot of researchers have been trying to overcome the limit. Electron microscopes such as SEM and TEM break the diffraction limit by using electrons which have much shorter wavelength than electromagnetic wave. They have very high resolution, but disadvantages are also existed. The images from electron microscopes cannot give us any optical information and only provide black and white images. Moreover, the sample can be modified by preparation processes (for example, metal-

lic coating) which are necessary for electron microscope imaging.

Atomic force microscope (AFM) is a kind of scanning probe microscope (SPMs). It can visualize the surface profile of sample with high lateral resolution. It uses sharp metallic tip with cantilever and measures surface profile by detecting the atomic force between tip and the sample. However, only surface profile can be obtained, and no other information can be collected. Various optical methods have been also tried. By blocking out-of-focused light with a small pinhole, confocal laser scanning microscope (CLSM) can improve the resolution. However, it is also limited by diffraction. In recent years, super-resolution microscopy techniques such as structured illumination microscopy (SIM), stimulated emission depletion (STED), photo activated localization microscopy (PALM), stochastic optical reconstruction microscopy (STORM), etc. were introduced.

Near-field imaging technique is one of the high resolution imaging methods with sub-diffraction limit, and it is widely used in various research areas. By using near-field scanning optical microscope (NSOM), surface profile and optical information can be simultaneously measured. The original concept of near-field detection was proposed by E.H.Synge for the first time [Synge, 1928]. The idea of applying piezo-electricity to microscope was also suggested by him [Synge, 1932]. His idea was based on the fact that the highly resolved optical detection which can overcome the diffraction limit would be possible if a small aperture ($a \ll \lambda$ where $a$ is the diameter of aperture and $\lambda$ is the wavelength of light) is approached to the surface close enough ($z \ll \lambda$ where $z$ is the distance between surface and aperture) (Figure 1-1). He shared this idea with Albert Einstein, and they exchanged letters to each other [Novotny, 2007]. However, at that time, there were not sufficiently advanced techniques to make the concept a real instrument (e.g. laser, making piezo-electric elements, sub-wavelength aperture, etc.). Therefore, the actual near-field measurement was realized much later.

| Classification | Name | Acronym | XY-resolution | Z-resolution |
|---|---|---|---|---|
| Electron Microscopes | Scanning Electron Microscope | SEM | less than 1 nm | |
| | Transmission Electron Microscope | TEM | 50pm[a] | |
| Scanning Probe Microscopes | Atomic Force Microscope | AFM | atomic level | atomic level |
| | Scanning Tunnelling Microscope[b] | STM | 0.1 nm | 0.01 nm |
| Optical Microscopes[c] | Confocal Laser Scanning Microscope | CLSM | 180-250 nm | 500-700 nm |
| | Structured Illumination Microscopy | SIM | 100-130 nm | 250-350 nm |
| | STimulated Emission Depletion | STED | 20-100 nm | 560 nm |
| | Photo Activated Localization Microscopy | PALM | 20-50 nm | 75 nm |
| | Near-field Scanning Optical Microscope | NSOM | 20-120 nm | 10 nm |

[a] Erni et al. [2009]
[b] Bai [2000]
[c] Schermelleh et al. [2010]

Table 1.1: High-resolution microscopy methods

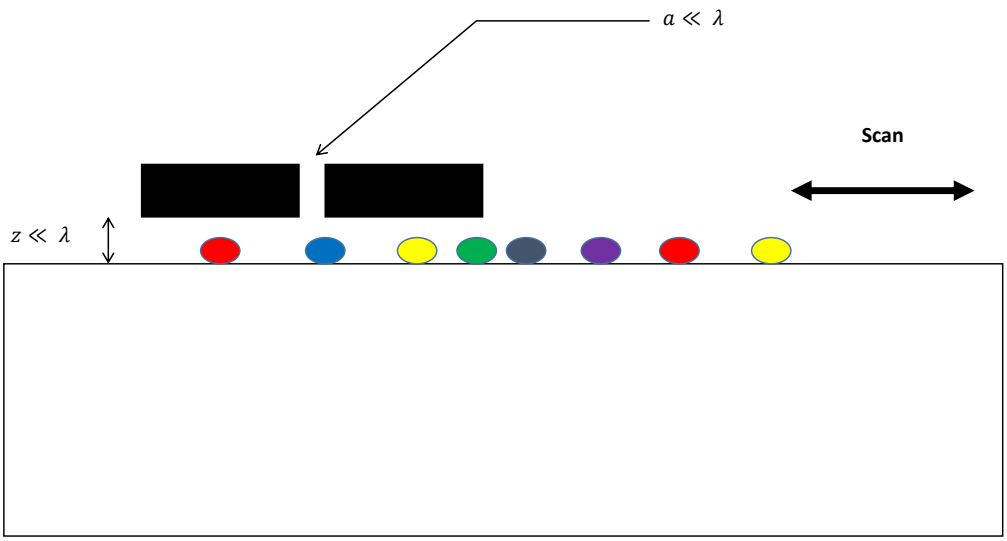


Figure 1-1: Original concept of near-field scanning optical microscope

In 1972, the first near-field measurement in microwave region was performed by Ash and Nicholls [Ash and Nicholls, 1972]. 12 years later, researchers at *IBM Zurich Research Lab* [Pohl et al., 1984] and *Cornell University* [Lewis et al., 1984] achieved near-field detection in optical domain independently. The main ideas of both groups were based on the Synge's proposal. However, there were little differences between the methods proposed by the two groups. *IBM Zurich Research Lab* produced the sharp tip of quartz crystal by chemical etching. This tip was coated by metal and touched by microscope slide. The probe was approached to the sample for each pixel. After the signal detection completed at one pixel point, the probe retracted back and re-approached to the sample at the next pixel. *Cornell University* group made the small aperture using electron beam on the single crystal silicon disc.

In the middle of the 1980s, Betzig et al., in *Cornell University* successfully got a near-field image of a grating, which has the width of 200 nm, by using sharp fiber probe tip [Betzig et al., 1986]. Some groups could detect the evanescent field at the surface by using the total internal reflection [Courjon et al., 1989; Reddick et al., 1989].

In 1990s, various kinds of distance regulation methods were introduced. In order to collect the optical signal near the surface, the aperture should be approached to the surface and maintain the distance. Shear-force detection was one of the most widely applied idea for distance regulation [Karrai and Grober, 1995; Ruiter et al., 1997; Zhu et al., 1996]. They could maintain the distance between sample and probe tip by using resonance characteristics of crystal tuning fork. Another scheme to solve the distance regulation was AFM cantilever method [Akamine et al., 1996].

Moreover, different types of NSOM were proposed by a lot of groups in 1990s. Apertureless near-field scanning optical microscope (ANSOM) was first proposed in 1995 [Gleyzes et al., 1995; Hayazawa et al., 2000; Zenhausern et al., 1995]. This type of NSOM used sharp tip as a scatterer, and they collected the light scattered at the end of the probe tip. Since the scattered field can be influenced by the dipole interaction between sample and the tip, two-dimensional map can be obtained by scanning the surface. Other kind of NSOM did not use probe tip. They trapped a small particle by laser and used that particle as the probe [Kawata et al., 1994; Malmqvist and Hertz, 1992].

Nowadays, NSOM is one of the most widely employed instruments for various research fields, especially, in biology [Eisele et al., 2009; Müller and Dufrêne, 2011; Smith et al., 2013; Zhong et al., 2011] and plasmonics [Aigouy et al., 2011; Cho et al., 2010; Dorfmuller et al., 2011; Minovich et al., 2011; Wang and Zhou, 2010].

## 1.2 What is “Near-field Optics”?

### 1.2.1 Diffraction Limited System

#### (a) Abbe Criterion

A classical imaging system is limited by diffraction. According to Ernst Abbe, *“the object acts as a diffraction grating, so that not only every element of the aperture of the objective, but also every element of the object must be taken into account in determining the complex disturbance at any particular point in the image plane”* [Born and Wolf, 1999]. *Abbe diffraction limit* is widely accepted to define the resolution limit of an image forming system. The basic interpretations for *Abbe diffraction limit* will be explained in this section. This description will follow the book of Lipson et al. [Lipson et al., 2010].

Let’s consider the image formation of diffraction grating which has the pitch of

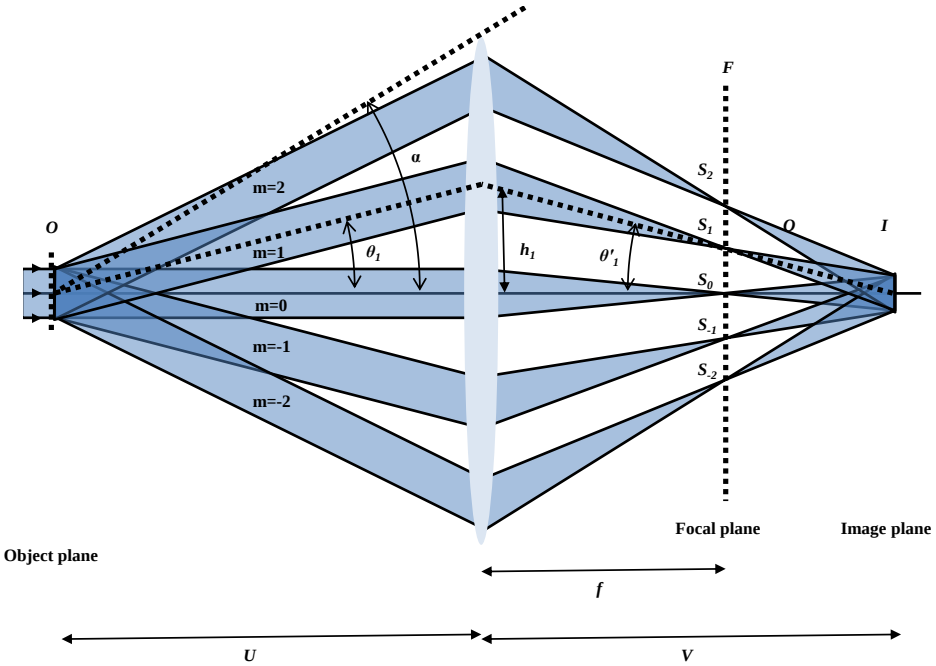


Figure 1-2: Image formation for diffraction grating

$d$ by using a coherent light (Figure 1-2). When a diffraction grating is placed on the object plane ($O$), the incident parallel beam is diffracted with the order of $m$. Each order is described as a plane wave and all the diffraction orders are focused at the focal plane ($F$) by the lens, to finally form an image of the object at the image plane ($I$). Therefore, the Fraunhofer diffraction pattern is observed in $F$.

Let the focused point for each order $m$ be $S_m$. Each $S_m$ behaves like a point source and the image can be considered as their interference. The interference cannot occur only if the zeroth order passes the lens. It means that the pitches of grating cannot be resolved. Therefore, at least +1 and -1 orders should pass the lens for this system in order to resolve the periodicity of grating.

By basic interference theory, the angle of diffraction order $m$ is given by,

$$\sin\theta_m = \frac{m\lambda}{nd} \tag{1.1}$$

Therefore, the resolvable minimum distance between the grating's piths can be described by,

$$d_{min} = \frac{\lambda}{n\sin\alpha} = \frac{\lambda}{\text{N.A.}} \tag{1.2}$$

where N.A. represents the *Numerical Aperture*.

In fact, the resolution limit can be obtained when the objective lens can collect the zeroth and one of the first order (+1 or -1) only. By illuminating the grating with an angle $\alpha$, the maximum resolution can be determined. In this case, the zeroth order only passes to the edge of the lens, so the minimum resolvable period (= diffraction limit) is,

$$d_{min} = \frac{\lambda}{n\sin\alpha} = \frac{\lambda}{2\text{N.A.}} \tag{1.3}$$

This result is called "**Abbe diffraction limit**".

### (b) Rayleigh Criterion

Let a coordinate of aperture be $(x, y)$, and the one of diffraction pattern be $(\xi, \eta)$. And the distance between the aperture and the diffraction is $z$. By Huygens-Fresnel principle, the diffracted field can be written as [Goodman, 2004],

$$U(x,y) = \frac{z}{i\lambda} \iint_{\Sigma} U(\xi,\eta) \frac{\exp(ikr_{01})}{r_{01}^2} \mathrm{d}\xi \mathrm{d}\eta \tag{1.4}$$

where $r_{01}$ is given by

$$r_{01} = \sqrt{z^2 + (x-\xi)^2 + (y-\eta)^2} \tag{1.5}$$

By using binomial expansion, this can be approximated by,

$$r_{01} \approx z \left[ 1 + \frac{1}{2} \left( \frac{x-\xi}{z} \right)^2 + \frac{1}{2} \left( \frac{y-\eta}{z} \right)^2 \right] \tag{1.6}$$

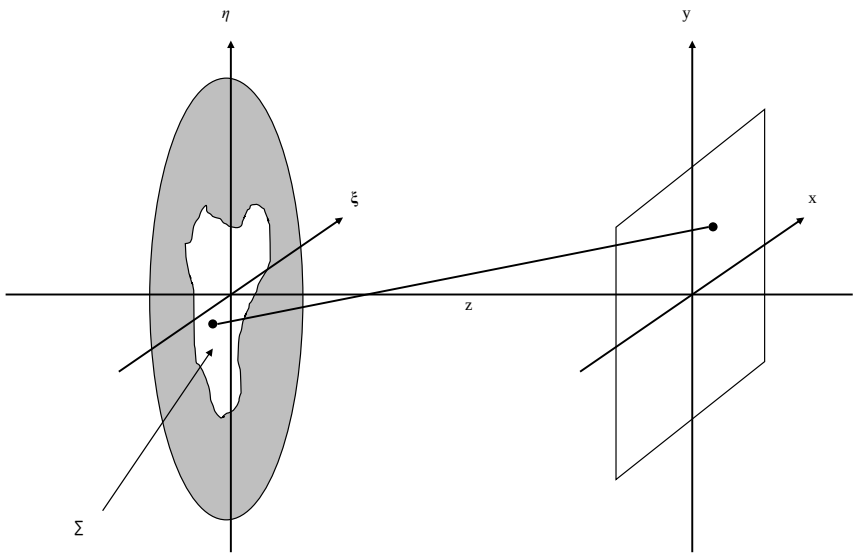


Figure 1-3: Diffraction geometry of an opening aperture

Equation (1.4) is rewritten by,

$$U(x,y) = \frac{e^{ikz}}{i\lambda z} \iint_{-\infty}^{\infty} U(\xi,\eta) \exp\left\{ i\frac{k}{2z}\left[(x-\xi)^2 + (y-\eta)^2\right]\right\} \mathrm{d}\xi \mathrm{d}\eta \tag{1.7}$$

In the region of *Franuhofer diffraction* or the *far-field*

$$z \gg \frac{k(\xi^2+\eta^2)_{max}}{2}, \tag{1.8}$$

equation (1.7) can be described by,

$$U(x,y) = \frac{e^{ikz} e^{i\frac{k}{2z}(x^2+y^2)}}{i\lambda z} \iint_{-\infty}^{\infty} U(\xi,\eta) \exp\left[-i\frac{2\pi}{\lambda z}(x\xi + y\eta)\right] \mathrm{d}\xi \mathrm{d}\eta \tag{1.9}$$

If the rectangular coordinates are replaced by polar coordinates, we can write $x, y, \xi$ and $\eta$ as follows;

$$x = r\cos\theta \qquad y = r\sin\theta \tag{1.10}$$

$$\xi = \rho\cos\phi \qquad \eta = \rho\sin\phi \tag{1.11}$$

Then, equation (1.9) can be written by,

$$\begin{aligned} U(r) &= \frac{e^{ikz} e^{i\frac{kr^2}{2z}}}{i\lambda z} \int_0^{2\pi}\int_0^{\infty} U(\rho,\phi) \exp\left[-i\frac{2\pi}{\lambda z}(r\cos\theta\rho\cos\phi + r\sin\theta\rho\sin\phi)\right] \rho \mathrm{d}\rho \mathrm{d}\phi \\ &= \frac{e^{ikz} e^{i\frac{kr^2}{2z}}}{i\lambda z} \int_0^{2\pi}\int_0^{\infty} U(\rho,\phi) \exp\left[-i\frac{2\pi}{\lambda z} r\rho\cos(\theta-\phi)\right] \rho \mathrm{d}\rho \mathrm{d}\phi \end{aligned} \tag{1.12}$$

Equation (1.12) is related to the first kind of Bessel function (see equation (A.2) in Appendix A),

$$U(r) = \frac{e^{ikz} e^{i\frac{kr^2}{2z}}}{i\lambda z} \int_0^{\infty} U(\rho,0) 2\pi J_0\left(\frac{2\pi}{\lambda z} r\rho\right) \rho \mathrm{d}\rho \tag{1.13}$$

When the radius of the aperture is $w$, equation (1.13) is (see equation (A.6) in

Appendix A),

$$U(r) = e^{ikz} e^{i\frac{kr^2}{2z}} \frac{A}{i\lambda z} \left[ 2\frac{J_1(2\pi wr/\lambda z)}{2\pi wr/\lambda z} \right] \tag{1.14}$$

where $A = \pi w^2$. This distribution is called *Airy pattern*. The first zero of this pattern (table 1.2) exists at,

$$r_0 = 0.61\frac{\lambda z}{w} \tag{1.15}$$

Rayleigh considered the situation that the first zero of a *Airy pattern* matches with the center of another *Airy pattern*. This is the extreme condition for the resolution of system.

Lens can be considered as a circular aperture. Figure 1-4 shows the Rayleigh's idea. Let's assume that the lens has the diameter of $D$. For the case of small angle,

$$\theta \approx \tan\theta = \frac{0.61\lambda z/w}{z} = 1.22\frac{\lambda}{D} \tag{1.16}$$

| x | $\left[2\frac{J_1(\pi x)}{\pi x}\right]^2$ | max, min |
|---|---|---|
| 0 | 1 | max |
| 1.220 | 0 | min |
| 1.635 | 0.0175 | max |
| 2.233 | 0 | min |
| 2.679 | 0.0042 | max |
| 3.238 | 0 | min |
| 3.699 | 0.0016 | max |

Table 1.2: Location of maxima and minima of the Airy pattern [Goodman, 2004].

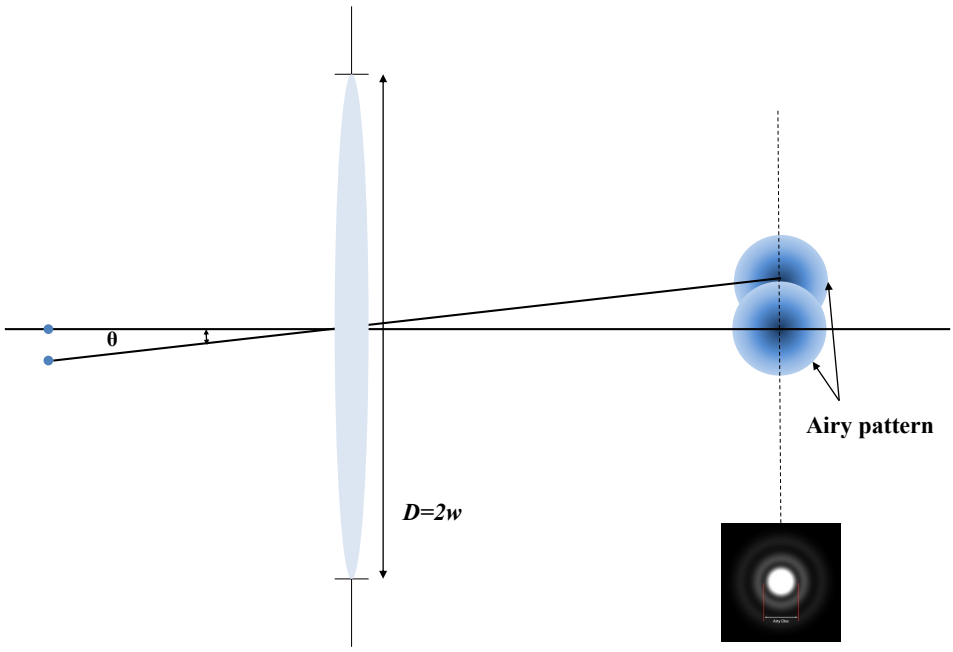


Figure 1-4: Rayleigh criterion

This is "**Rayleigh criterion**", which represents the angular resolution of the system. For a microscope, the distance between the objects and the lens is close to the focal length, indicating

$$\Delta l \approx f\theta \approx 1.22\frac{f\lambda}{D} \approx 0.61\frac{\lambda}{\text{N.A.}} \tag{1.17}$$

### 1.2.2 Far-field Optics (Classical Optics)

In classical optics, the resolution of optical imaging system is limited by diffraction. It is inevitable when the imaging system is based on the lenses. This resolution limits were calculated by Abbe and Rayleigh, resulting in $\lambda/2\text{N.A.}$ and $0.61\lambda/\text{N.A.}$, respectively. From these results, one can notice that the resolution can be improved by increasing N.A. or reducing the wavelength of light.

However, the visible light corresponds to wavelengths spanning between 400 nm (violet) and 780 nm (red). Moreover, it is difficult to fabricate an objective

lens with high N.A., especially in the UV range. The highest N.A., commercially available from *Olympus Co.*, is around 0.95 (which is designed to be used in air; MPLAPON100x) or 1.4 (which is designed for oil-immersion type; MPLAPON100XO). Using Rayleigh's result, the available maximum resolutions for visible light are about 270 nm for N.A.=0.95 or 170 nm for N.A.=1.4.

### 1.2.3 Near-field Optics

Classical optics systems can detect only the Fraunhofer diffraction. Near-field optics represents the investigation of light near the surface of sample. By scanning the surface by using the nanoscopic probe, one can detect the light before diffraction. Therefore, the near-field optical system does not depend on the diffraction. Consequently, the resolution can be extremely improved because of its diffraction-free nature.

In addition, an *evanescent field* can be detected in near-filed optics systems. It is confined only near the surface, and exponentially decayed from the surface. It travels along the surface, so that it can not be detected by classical optics. Near-field optics system can observe this field by coupling with a near-field probe. In the case of aperture type probe, propagating electromagnetic waves in the direction of the aperture can be generated by such coupling of the evanescant wave. The apertureless probe can enhance the scattering field by coupling the probe to the sample.

Various modes of NSOM operation are possible. The sample can be excited by objective lens, and the probe can collect the signal (collection mode). The opposite case is also possible (illumination mode). The probe can also illuminate the sample and collect the signal simultaneously (illumination collection mode). The probe can also illuminate the sample, and the reflected light can be collected by objective

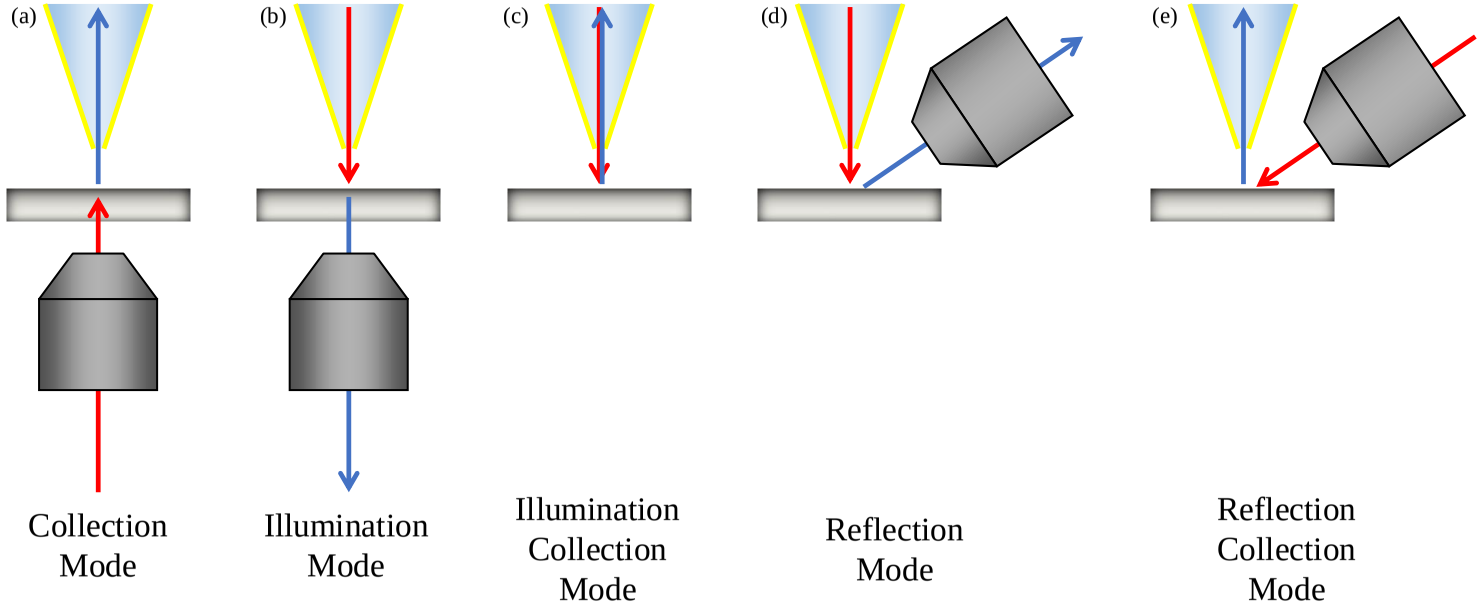


Figure 1-5: Various modes of NSOM operation

(reflection mode). The opposite case is also possible (reflection collection mode). Figure 1-5 illustrates various operation modes for the NSOM.

## 1.3 Near-field Scanning Optical Interferometer

Phase of light has a lot of information about material and environment in the path of light. Therefore, phase measurement has played an important role in various areas. Nowadays, phase measurement for biological structures in cellular scale attracts much attention [Creath and Goldstein, 2012; Kim et al., 2014; Popescu et al., 2004; Taylor et al., 2013].

It is expected that phase information with nanometric-level spatial resolution, caused by optical properties (for example, refractive index) of the sample, can be obtained by combining NSOM's high-resolution imaging system with interferometric technique. For this reason, there have been several attempts to obtain the phase information from the transparent materials with high-resolution and ultra-sensitivity by combining NSOM with interferometer.

First attempt to measure the phase by using NSOM was performed by Vaez-Iravani and Toledo-Crow, 1993. Few years later, IBM's researchers published important papers by using ANSOM [Zenhausern et al., 1995, 1994]. They focused two split laser beams at the surface and detect the interference between them. In 2000, various groups also published the results of near-field phase measurement by using ANSOM [Balistreri et al., 2000; Hillenbrand and Keilmann, 2000; Sasaki and Sasaki, 2000]. In recent years, a lot of groups studied the phase variation of metallic nano-particles or nano-structures, which are associated to the surface plasmon resonances [Carney et al., 2012; Deutsch et al., 2008, 2010; Kihm et al., 2010; Kinzel et al., 2012; Schnell et al., 2010].

Most of the near-field phase measurement are using the scattering (aperture-less) NSOM. In this thesis, a new type of near-field phase measurement system which uses a fiber probe tip with opening aperture is proposed. Not only the surface topog-

raphy and phase but also the near-field signal can be simultaneously measured by collection mode NSOM with the help of the aperture type probe tip. The instrument is called near-field scanning optical interferometer (NSOI).

## 1.4 Thesis Scope

This thesis contains construction of NSOM and NSOI, explanation of phase measurement, and investigation of various nano-materials by using the instrument.

In Chapter 2, the detailed construction of NSOM is described. The distance regulation method and the configuration of NSOM unit are also explained. Then, the LabVIEW program in order to operate the system is outlined. The user interface (UI) and the algorithm of each part of program are also explained in detail.

Chapter 3 illustrates the schematic of the proposed NSOI a method to remove background from the NSOI measurement. It begins with basic principle of interference theory and explains the main process of removing background signal. Reliability test of the phase measurement system is performed for reference sample and optical discs. For the test, SNG01 and various optical discs are selected. Especially, blu-ray discs which have the sub-wavelength track pitch is analysed by using NSOI.

Chapter 4 presents the phase measurement results for the 2-dimensional materials, especially graphene and monolayer $MoS_2$. The band structure of graphene is calculated by tight-binding model. The near-field investigation on monolayer graphene are performed by using the NSOI. The similar experiment performed for monolayer $MoS_2$ is also displayed.

Chapter 5 describes the direct laser writing (DLW) in silver-containing glasses. The explanation for DLW and the fluorescence properties of the sample are presented first. After that, spectral investigations for DLW patterns on a glass by using confocal spectrometer are described. At the end of the chapter, the structural properties of the patterns studied by using NSOM and NSOI are illustrated. The fluorescence measured by illumination and collection mode NSOM and the phase variation investigated by using NSOI are presented. The correlation of phase and

fluorescence measurements is detailed, to get a better understanding of the ongoing processes during DLW.

And finally, chapter 6 concludes the thesis and summarizes the results.

Since NSOI is the combination of NSOM and interferometer, various advantages can be expected. Because of the near-field detection approach, resolution can be extremely increased beyond diffraction limit. Moreover, ultra-sensitive detection of optical path-length difference can be obtained thanks to the interferometric approach. Therefore, promising atomic-layered materials such as graphene and monolayer $MoS_2$ and nanometric refractive index modification can be investigated by using this novel phase detection technique, NSOI. Indeed, new correlative imaging measurements (phase, topography, illumination or collection modes of laser wavelengths or fluorescence) is expected to bring new experimental ability to access relevant knowledge of material fabrication or processing history. It can either include the signature of its synthesis or the result of subsequent modifications, resulting from a desired external structuring (as laser structuring) or from an unwanted material damaging or ageing.

# Chapter 2

# Experimental System and Operation Program

## 2.1 Introduction

Since the first proposal about the basic concept of near-field microscope, it took almost 60 years to realize the realistic near-field microscope. The idea was simple, but technology was not available. The problems were i) how to make the aperture of sub-wavelength scale, ii) how to scan with nano-metric resolution, and iii) how to approach the aperture to the sample and to maintain the distance. The aperture problem (i) was solved by the development of optical fiber fabrication technique. The resolution problem (ii) was solved by using piezo-electricity. However, the distance regulation problem (iii) was not simple. In order to solve the distance regulation problem, a lot of techniques, such as AFM cantilever method [Akamine et al., 1996; Zenhausern et al., 1994] and evanescent field detection technique [Uma Maheswari et al., 1996], were tried. But shear-force detection scheme became the most common method to solve this problem [Betzig et al., 1992; Karrai and Grober, 1995;

Ruiter et al., 1997; Toledo-Crow et al., 1992; Zhu et al., 1996].

### 2.1.1 Distance Regulation Method: Shear-force Detection

"Shear-force" originate from the interaction between the probe tip and the sample surface when the probe tip vibrates laterally. The distance between the probe tip and the surface can be estimated by measuring the shear-force. When a laterally-vibrating probe approaches close to the near-field region, the shear-force starts to act as a damping factor and the vibrating amplitude decreases with the distance. When shear-force detection technique was applied to NSOM system, optical detection scheme was used to detect the variational amplitude of probe [Betzig et al., 1992; Toledo-Crow et al., 1992]. After few years later, piezoelectric tuning fork was proposed to detect the shear-force variation [Karrai and Grober, 1995; Ruiter et al., 1997; Zhu et al., 1996].

Tuning fork method has several advantages compared to optical method. Since it does not need additional optical components for the distance detection, the system can become more compact. Therefore, it can be easier to be implemented in the system. The system can achieve high sensitivity with low price because of the quartz crystal tuning fork. For these reasons, the tuning fork scheme is widely accepted to detect the shear-force. Figure 2-1 illustrates the concept of distance regulation by using tuning fork. During scanning the surface, the distance between NSOM probe and the surface is maintained by monitoring the oscillation amplitude of tuning fork.

Tuning fork is made of quartz crystal, and its typical resonance frequency is 32.768 kHz. The process to measure shear-force is as follows. When a fiber probe tip is glued to one arm of the tuning fork, the resonance characteristic of tuning fork (the frequency and the amplitude) is changed [Karrai and Grober, 1995]. And if the tuning fork starts to detect shear-force, the resonance frequency is slightly shifted

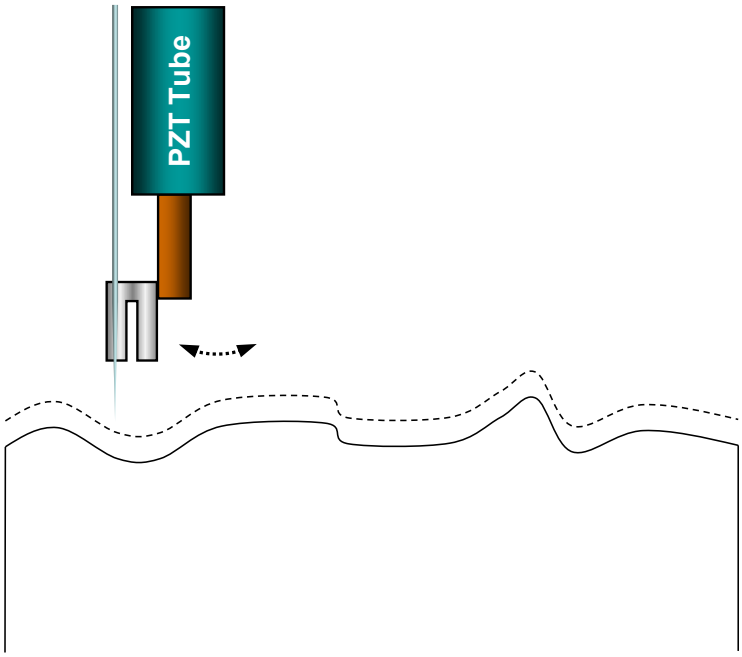


Figure 2-1: The concept of distance regulation by using shear force detection

[Ruiter et al., 1997]. This shift can be detected by using lock-in amplifier. Therefore, the distance between probe and the sample surface can be maintained by proper feedback.

## 2.2 Composition of NSOM Unit

In order to realize the near-field imaging principle, various electronic equipments are required. Figure 2-2 shows the flowchart of electrical signals among the components. This figure shows the brief explanation of how the experiments are performed. Figure 2-3 displays the real setup of the system. The main components consisting of the NSOM unit are head, head controller, proportional-integral (PI) feedback controller, lock-in amplifier, picomotor actuator, nano-positioning stage, detectors and data acquisition (DAQ) board. All these components will be briefly explained in the following sections.

### 2.2.1 Components

#### (a) Head

NSOM head is the most essential and crucial part for the experiment. It is composed of dithering PZT plate, quartz crystal tuning fork, translational PZT actuator for approaching and distance control, and electronic pre-amplifier. Figure 2-4 shows the picture of the NSOM head.

The tuning fork sensor is dithered by applying AC voltage to PZT plate. The oscillation signal of tuning fork is amplified by pre-amplifier. The dithering voltage is supplied by lock-in amplifier and the tuning fork signal is collected by DAQ board. The fiber probe tip approaches close to the surface by PZT actuator. NSOM head controller supplies the approaching voltage. NSOM head communicates with the controller by using 16-pin connector. Table 2.1 shows the configuration of 16-pin adapter.

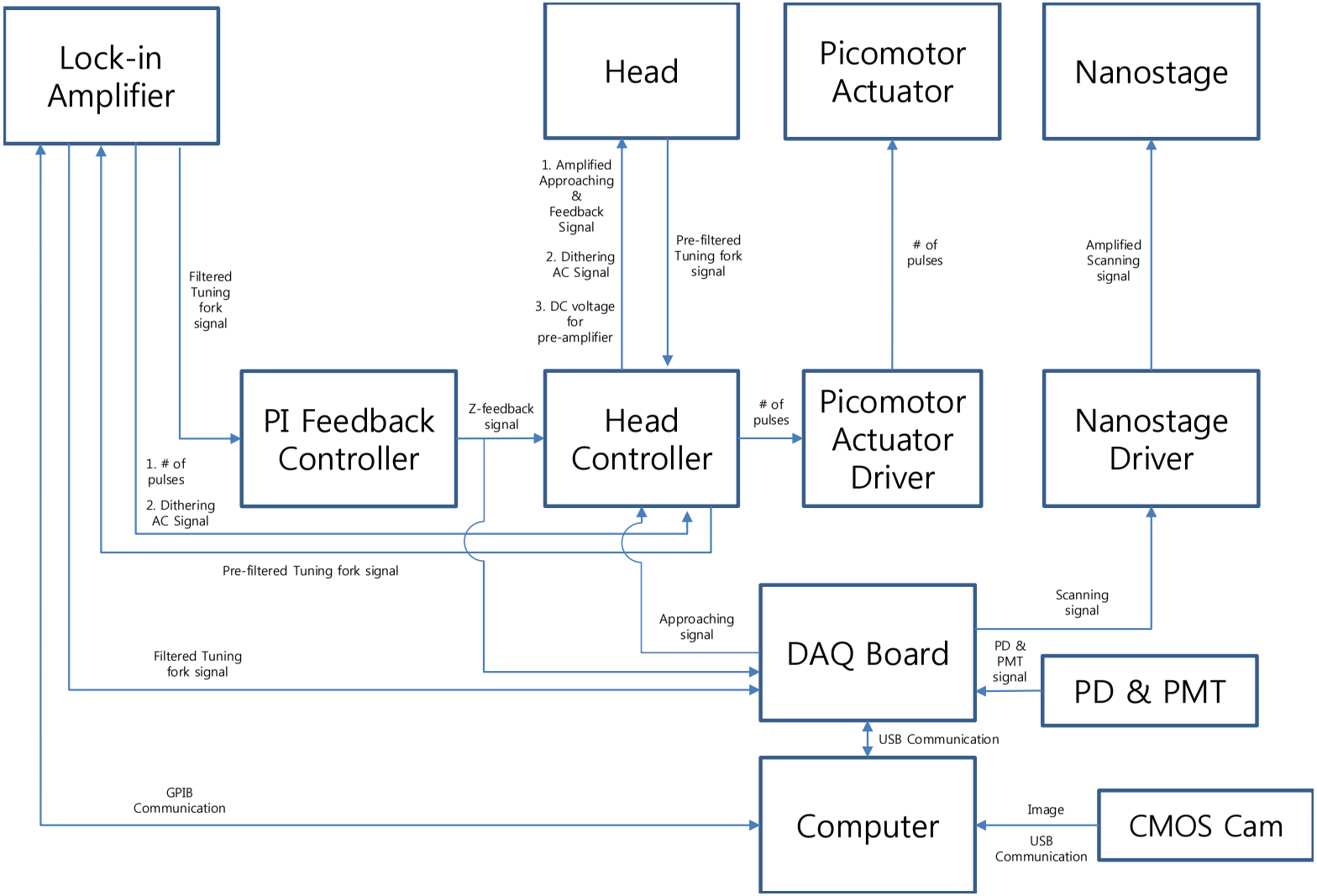


Figure 2-2: The flowchart of electrical signals between the components of NSOM unit

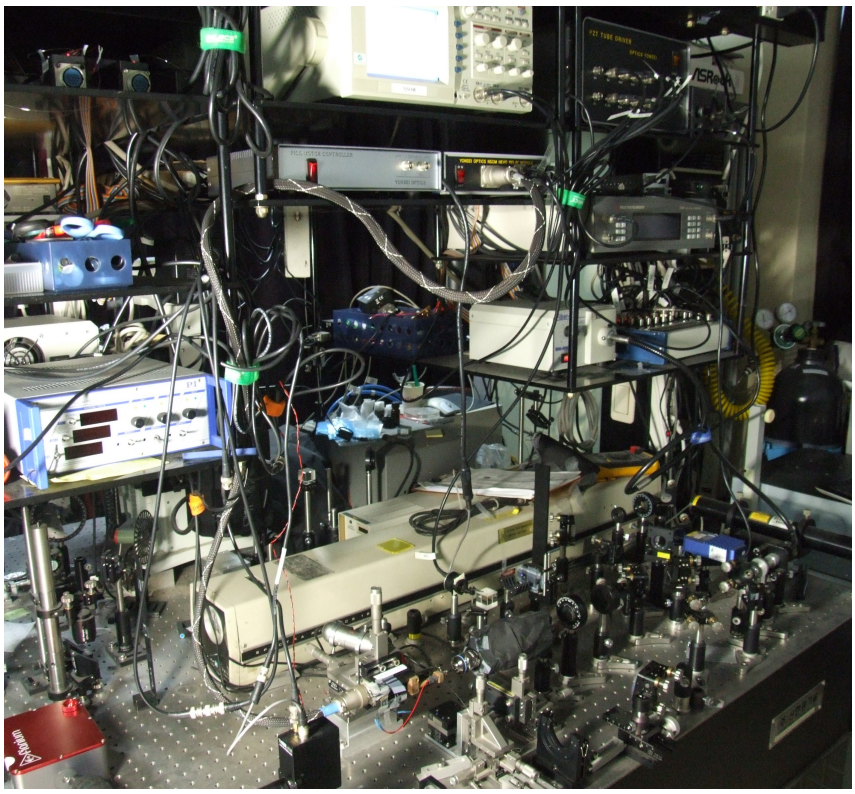

Figure 2-3: Picture of NSOI setup

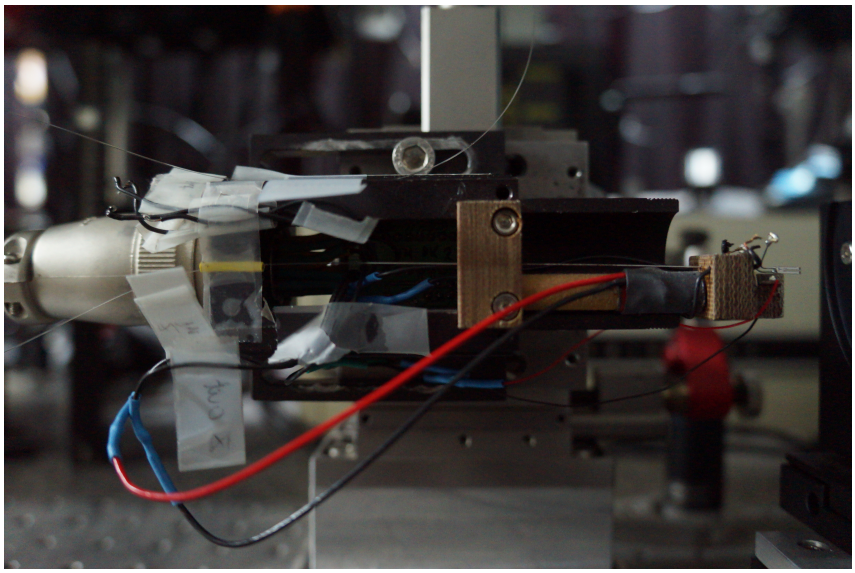

Figure 2-4: NSOM head

| Pin Number | Signal |
|---|---|
| 1 | +x direction voltage of the PZT tube |
| 2 | -x direction voltage of the PZT tube |
| 3 | +y direction voltage of the PZT tube |
| 4 | -y direction voltage of the PZT tube |
| 5 | +z direction voltage of the PZT tube |
| 6 | -z direction voltage of the PZT tube |
| 7 | Oscillation voltage from the tuning fork |
| 8 | PZT plate driving voltage |
| 9 | +15V DC power for the AD524 chip |
| 10 | -15V DC power for the AD524 chip |
| 11 | Ground for the AD524 chip |
| 12 | Ground for the oscillation voltage from the tuning fork |
| 13 | Not used |
| 14 | Not used |
| 15 | Ground for the PZT plate driving voltage |
| 16 | Not used |

Table 2.1: The configuration of 16-pin adapter [Lee, 2013]

### (b) Head Controller

The most of electric signals should pass through the head controller. Head controller communicates with other components by BNC, digital, and 16-pin port. It can be divided by 2 parts; high-voltage amplifier and relay module. They can be combined in one equipment or physically separated.

NSOM head is a composition of multiple electronic and mechanical components. High-voltage amplifier should supply enough voltage to piezo-actuator. It receives the translational voltages from the DAQ board and PI feedback controller and adds them. The voltage is supplied by DAQ board in this system, and the maximum possible voltage is 10 V. However, the traveling displacement of this actuator is 15 μm and the operation voltages should be between 0 V and 1000 V. Therefore, the high voltage supplier is necessary to control the actuator with μm scale. Head controller amplifies the voltage from the output channel of DAQ board with $\pm 30\times$ to positive and negative (ground) poles of BNC cable. As a consequence, the head controller supplies the $60\times$ amplified voltage to the PZT actuator.

Number of pulses for picomotor actuator and dithering AC voltage for PZT plate are relayed by head controller. Head controller receives the digital signals and dithering voltage from the lock-in amplifier and supplies to picomotor actuator driver and PZT plate inside NSOM head. It also supplies DC voltage (15 V) for pre-amplifier in the head.

### (c) PI Feedback Controller

After the fiber probe tip approaches to the surface of sample, the distance between the tip and sample should be maintained without contact. Otherwise, the fiber will be broken by an impact. For this purpose, a feedback loop is necessary to apply the correction voltage to the piezo-actuator in real time. Proportional-integral

(PI) feedback circuit is utilized to the system to satisfy this purpose. When feedback circuit turns on, it receives the oscillation signal of the tuning fork filtered by lock-in amplifier, double the voltage and compare that with reference signal. Since the distance between tip and surface is regulated by maintaining the oscillation amplitude to half of the shear force free state, the input signal to feedback circuit should be doubled. Then, it provides the differential voltage to the head controller continuously. In this case, the reference signal is supplied by output port of DAQ board and the general value is 150 mV. The differential signals are also collected by DAQ board. They are used to plot the surface topography.

**(d) Lock-in Amplifier**

The main purposes of using the lock-in amplifier are 1) applying AC signal with exact frequency what user want and 2) filtering the input signal and amplifying the pre-determined frequency signal. The set-frequency in lock-in amplifier is called "reference frequency". In the NSOM system, lock-in amplifier supplies the dithering voltage to the PZT plate in order to excite the tuning fork resonance. This signal is delivered to the head controller by BNC cable ("OSC OUT" connector) and relayed to the head by 16-pin cable. The oscillation signal of the tuning fork is measured by using the lock-in amplifier. It is received by 16-pin cable and BNC cable (Input "A" connector). This measured signal is used for distance regulation. Lock-in amplifier filters the input signal with excitation frequency and the filtered signals is transferred to PI feedback circuit ("Fast X" connector).

Lock-in amplifier used in our system is *Signal Recovery* model 7265. This model has additional functions for convenience. One of them is the existence of "DIGITAL OUTPUTS" connector. In this system, the digital signals for the picomotor actuator is also generated by the lock-in amplifier and delivered to the head controller. It

communicates with computer by GPIB protocol. It is the only component which directly communicate with computer except DAQ board.

### (e) Picomotor Actuator and Driver

The piezo-actuator has the traveling displacement of only few microns. Therefore, it is almost impossible to travel long-distance with piezo-actuator only. Picomotor actuator can travel almost cm scale with the resolution of a few tens of nm. Picomotor actuator driver receives digital signals from head controller, and it rotates with the number of signals. *New Focus* model 8302 is used. It has better than 30 nm resolution with minimal backlash over 1 inch (25.4 mm) travel range, and can exert a 5 lb (22-N) force. The digital signals for operating the picomotor actuator are generated by the lock-in amplifier, passed by the head controller and delivered to the driver. Finally, the driver can supply the exact number of pulses to control the picomotor actuator.

### (f) Nano-positioning Stage and Driver

NSOM acquires the image by scanning the the sample surface pixel by pixel. It should have the accuracy of nanometer scale at least. Moreover, the scanning areas could be few tens of μm times few tens of μm as well as few μm times few μm. Nano-positioning piezo-stage is a suitable instrument for this purpose. It has nanometer scale precision and its traveling range is over 100 μm.

XYZ piezo stage (*Physik Instrumente(PI)*'s P-611.3 NanoCube®) is used for the scanning system. The traveling range of this stage is up to 120 μm × 120 μm × 120 μm with the resolution of 0.2 nm. The operational voltage is applied by DAQ board to the driver. The driver amplifies voltage and makes the stage moving. This stage is used for the XY scanning of sample.

#### (g) Detectors

To transform the optical signals to electrical ones, 3 different kinds of optical detectors are installed in the system. CMOS usb camera is used for confirming the full-field microscope image and finding the location of the sample. It is directly connected to computer by usb interface. Photo-diode (PD) collects the reflected optical signal from the surface of samples. The signal collected by NSOM fiber is acquired by photomultiplier tube (PMT). PD and PMT signals are collected by the DAQ board.

#### (h) Data Acquisition (DAQ) Board

All the instruments should be controlled by computer. The computer should also can handle the data. DAQ board makes the interface between the computer and the other electronic instruments. USB-6259 BNC (*National Instruments (NI)*) has 4 BNC analog output and 16 BNC analog input channels. One of the output channels supply the reference voltage to the PI feedback controller, and the others are used for controlling the nano-positioning stage (X, Y) and PZT actuator (Z). The input channels are used for collecting the signals. DAQ board and the computer communicates with each other by using usb interface.

### 2.2.2 Characteristic Curve Measurement for Tuning Fork Distance Regulation Sensor

If all the hardwares are prepared, the resonance characteristics for the tuning fork sensor can be achieved. Since the distance sensing is performed near the resonant frequency, it is important to find the resonant frequency and the quality factor. The resonance of free standing quartz crystal tuning fork exists exactly at 32.768 kHz. However, it is shifted when the fiber tip is attached to one prong of the tuning fork.

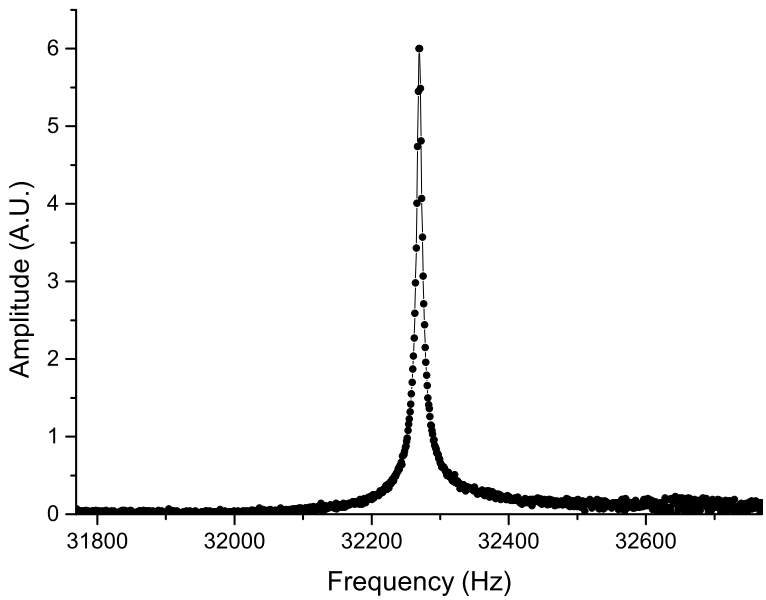


Figure 2-5: Resonance curve of tuning fork with fiber probe. The resonance frequency: 32.269kHz, Q-factor: 3256

First, the fiber-attached tuning fork is attached to a dithering PZT plate. AC voltage is applied to the plate by using lock-in amplifier, and the tuning fork is dithered with the reference frequency. The tuning fork can be oscillated with the reference frequency by using the lock-in amplifier again. The tuning fork's oscillating signal is amplified by a pre-amplifying electronic circuit in NSOM head. This signal is put into the lock-in amplifier again. Since the lock-in amplifier can filter and amplify the input signal which come from the reference frequency signal only, frequency-selective detection of tuning fork signal is possible. By varying the reference frequency of lock-in amplifier, tuning fork signal amplitude versus frequency curve can be plotted. This curve shows the resonance property of the tuning fork with attachment of the fiber tip.

Figure 2-5 shows the resonance curve. Using this graph, the resonance frequency and the Q-factor ($Q \sim \omega_0/\Delta\omega$) can be found. The higher the Q-factor is,

the more sensitive the tuning fork sensor can detect the variation of the oscillating amplitude. Therefore, the Q-factor is the key parameter to maintain the distance between the tip and the surface. It is important to achieve high Q-factor to obtain the height information accurately. In this system, $Q \sim 3000$ can be achieved, which is extremely high value compared to other researches [Ctistis et al., 2011; Yoo et al., 2004].

## 2.3 Operating Program

NSOM system is controlled by several electrical components; head controller, lock-in amplifier, PI feedback controller, picomotor driver, etc.. Electric voltage is applied to the system for approaching the fiber tip to the sample surface and scan the area of interest. Data are collected by PD and PMT, which provide us the electric voltage variation. To control the system and collect the signals more conveniently, it is necessary to use a computer and data acquisition instrument and build a operation program. DAQ board (*National Instruments (NI)*) and LabVIEW programming language are appropriate for this purpose.

The operating program is made by using LabVIEW. The basic interface and operations can be found in detail elsewhere [Lee, 2013]. Here, the differences and the details for NSOI experiment will be explained in following sections.

### 2.3.1 Initializing

When the program starts, it checks the connections of lock-in amplifier. If there is any problem to communicate with lock-in amplifier, the program gives an error message and stops working. Since the commands are only concerning the *Signal Recovery* model 7265, this process should be inserted before starting the experiment.

User can set the instrument by default in this first section of the program. The detailed setting value can be modified for the experimental conditions. But most of the values are already set by default. In ordinary condition, initializing part can be skipped if the previous operation conditions do not altered.

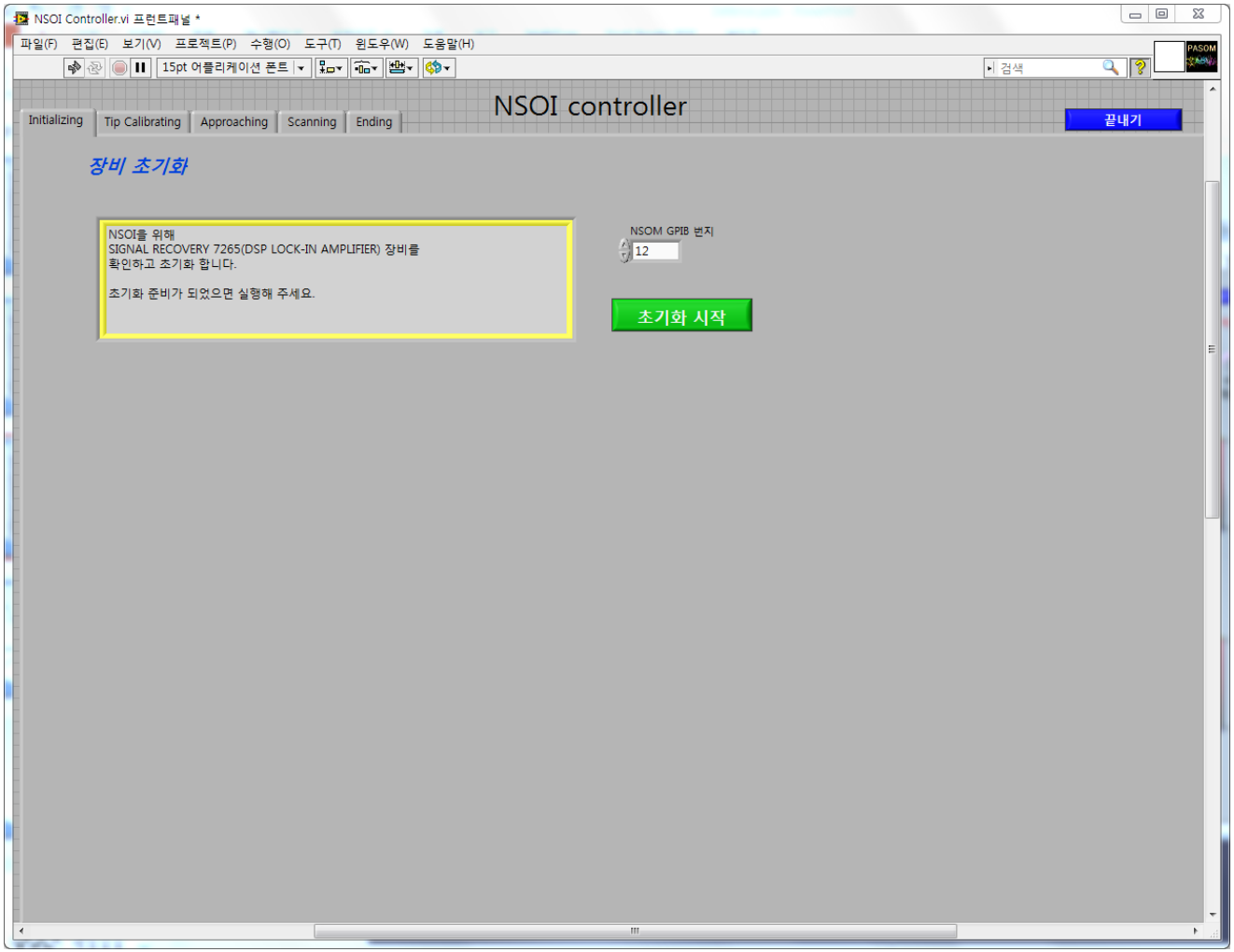


Figure 2-6: Initializing part of operation program.

### 2.3.2 Tip Calibrating

After the initializing is ended, the tab automatically moves to tip calibrating step. This step exists for measuring the characteristic curve of tuning fork. Figure 2-7 shows the tip calibrating section of the operation program.

First, the scanning range and speed should be determined. Three preset values which are mostly used for measurement can be selected. When the tip is attached to the NSOM head, the characteristic curve is obtained roughly. *Rough Test* option has the scanning range of 1000 Hz, the step of 10 Hz, and the duration time between the measurement of 100 ms. With this option, the scanning is performed over wide range of frequencies with fast speed. After that, *1000 Hz Exact Test* option is selected to obtain the exact resonance curve. This option has the values of 1000 Hz scanning range, 1 Hz step, and 1000 ms timing interval. The exact resonance frequency and the Q-factor can be obtained by this option. *20 Hz Exact Test* option has the same preset values with *1000 Hz exact Test* but the scanning range is 20 Hz. When the characteristic is slightly changed, this option can help to find out the exact values quickly.

The Q-factor is calculated by the equation of $Q \sim \omega_0/\Delta\omega$. Tip calibrating section calculates $\Delta\omega$ and Q-factor from the resonance curve. The curve is interpolated to find out the exact frequency at the half maximum of amplitude. With this process, the exact Q-factor can be found.

After finding the exact characteristic curve, lock-in amplifier fixes the frequency at the resonance and starts to set the maximum amplitude to 6 % by varying the dithering voltage automatically. 6 % is the proper amplitude to maintain the distance between sample and tip, which is obtained empirically.

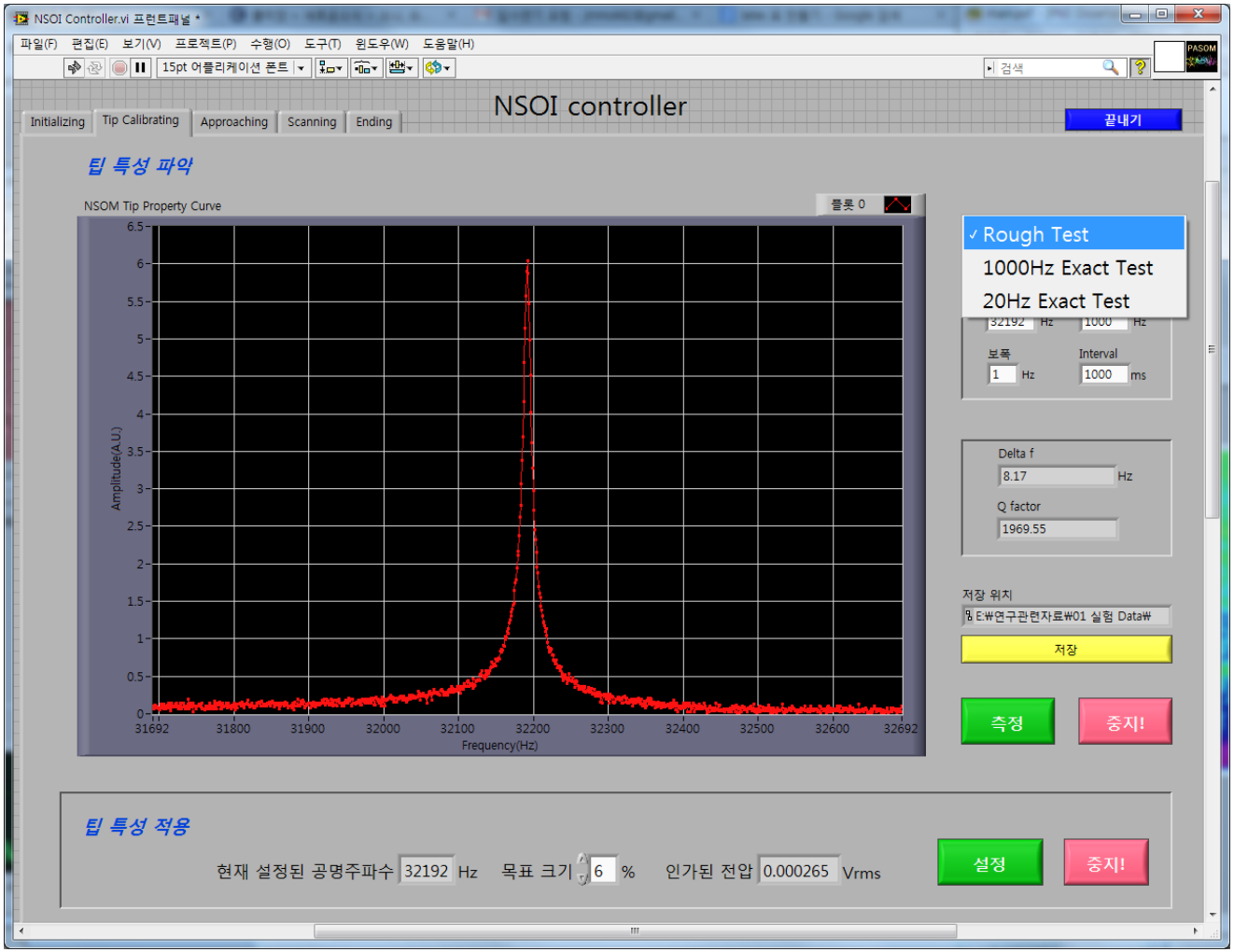


Figure 2-7: Tip calibrating part of operation program

### 2.3.3 Approaching

If it is confirmed that the resonance state of tuning fork attached with fiber probe tip is well enough to scan the surface in the tip calibrating section, the next step is approaching the fiber tip to near the surface.

The oscillation amplitude of the tuning fork rapidly decreases near the surface (especially the starting point to decrease the signal is below 50 nm [Karrai and Grober, 1995; Zhu et al., 1996]). The signal is detected by lock-in amplifier when the NSOM head approaches to the sample surface. When the oscillation amplitude decreases to the prefixed value (generally 3 %, which is half of the maximum amplitude, but it can be changed by the situation), it stops approaching and turns on the feedback circuit.

Picomotor actuators and PZT actuator are used to approach the NSOM head to the surface. Since the PZT actuator can travel only about 5 μm maximum, picomotor actuator takes the role to travel long distance. The NSOM head is attached to the 3-axis translational stage. The micrometer for approaching is replaced by the picomotor actuator.

First, the PZT actuator stretches the length around 1 μm to detect the oscillation signal. If the amplitude is maintained in this travel, the PZT actuator shrinks to the original position. Then, picomotor actuator makes the NSOM head to move about 1 μm, which are the same (in fact, only about 70 to 90 % not to crash the tip to the surface) distance traveled by the PZT actuator. This process is repeated until the oscillation amplitude decreases below the preset value. After the approaching ends, the feedback circuit turns on automatically. This is the final state before scanning the surface.

Figure 2-8 shows the screenshot of the approaching section. The large waveform chart exists to monitor the amplitude of the tuning fork. The maintaining am-

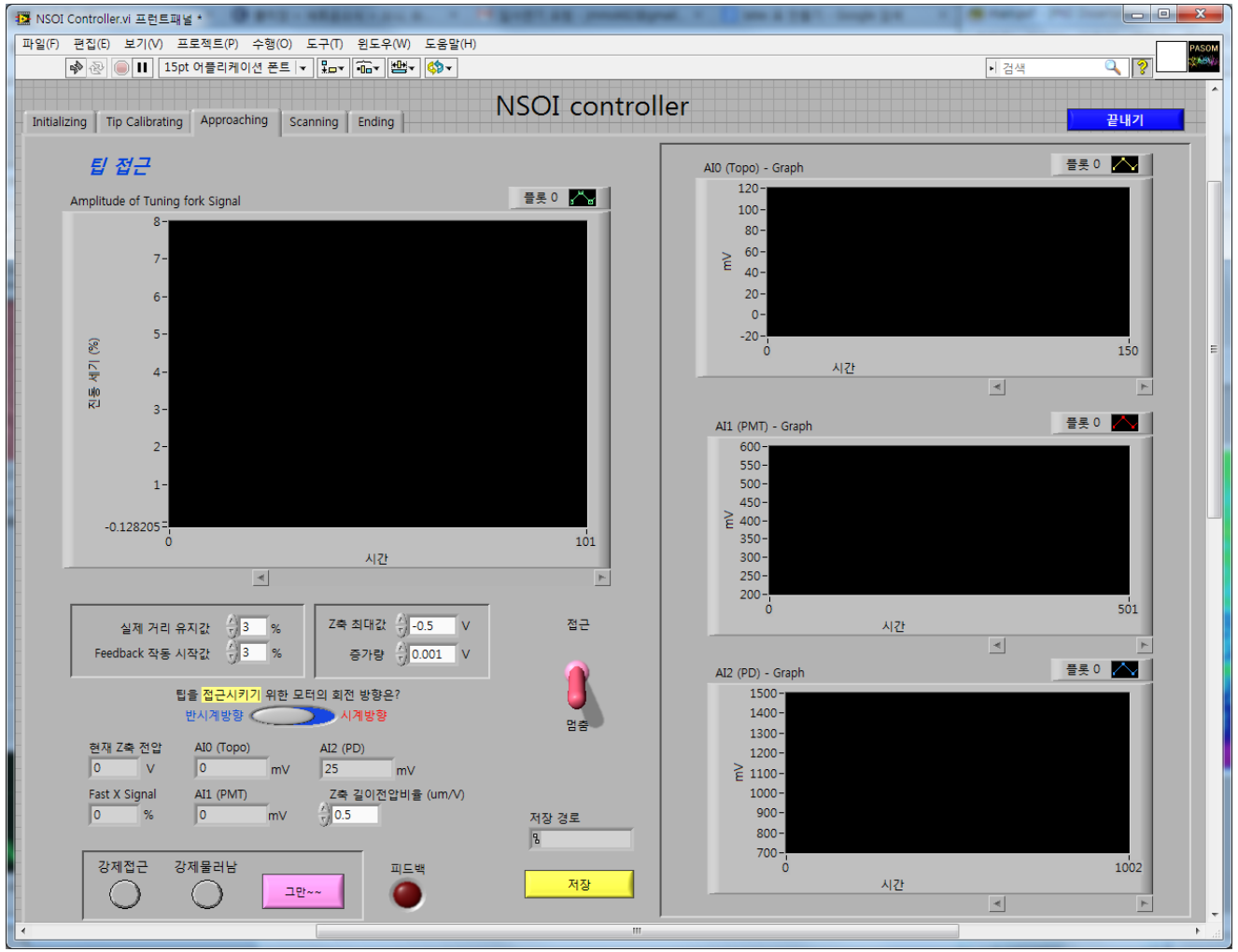


Figure 2-8: Approaching part of operation program

plitude of tuning fork and the starting point to feedback can be set individually. In addtion, the maximum voltage for the PZT actuator and the voltage step and length to voltage ratio can be also set.

The NSOM head can be approached or receded only by using the picomotor actuator. Since it can take too much time to complete approaching with the protocol, the approaching time can be reduced by this function; but this should be carefully used because the distance can not be easily recognized.

The feedback can be manually turned on. On the right side, the applied voltage and optical signals are monitored by the waveform charts.

### 2.3.4 Scanning

Now, it is ready to measure the near-field properties of the samples. In this section, the detailed conditions to scan the surface and measure the properties is described. Figure 2-9 shows the scanning section of the operation program.

Before the scanning starts, the range and the pixel number should be set. Since the length to voltage ratios for each axis can be set (typically 10 μm / V for P-611.3 NanoCube® XYZ Piezo Stage; this value can be manually changed for different instrument), the calculated voltages for changing the length are supplied to the nano-positioning stage by DAQ board. The pixel number determines the precision of the scanning step. Since NI USB-6259 has digital-to-analog converter (DAC) with 16 bits resolution, the minimum voltage step can be 10 V / $2^{16}$ ($\sim$ 0.15 mV) when the output range is set from 0 V to 10 V, indicating that the minimum scanning length step is about 1.5 nm. This range is short enough for the experiment. The scanning is performed line-by-line.

For certain situation, it is necessary to tilt the scanning angle. Therefore, modification of angle is required. Figure 2-10 (a) shows the basic principle to tilt the

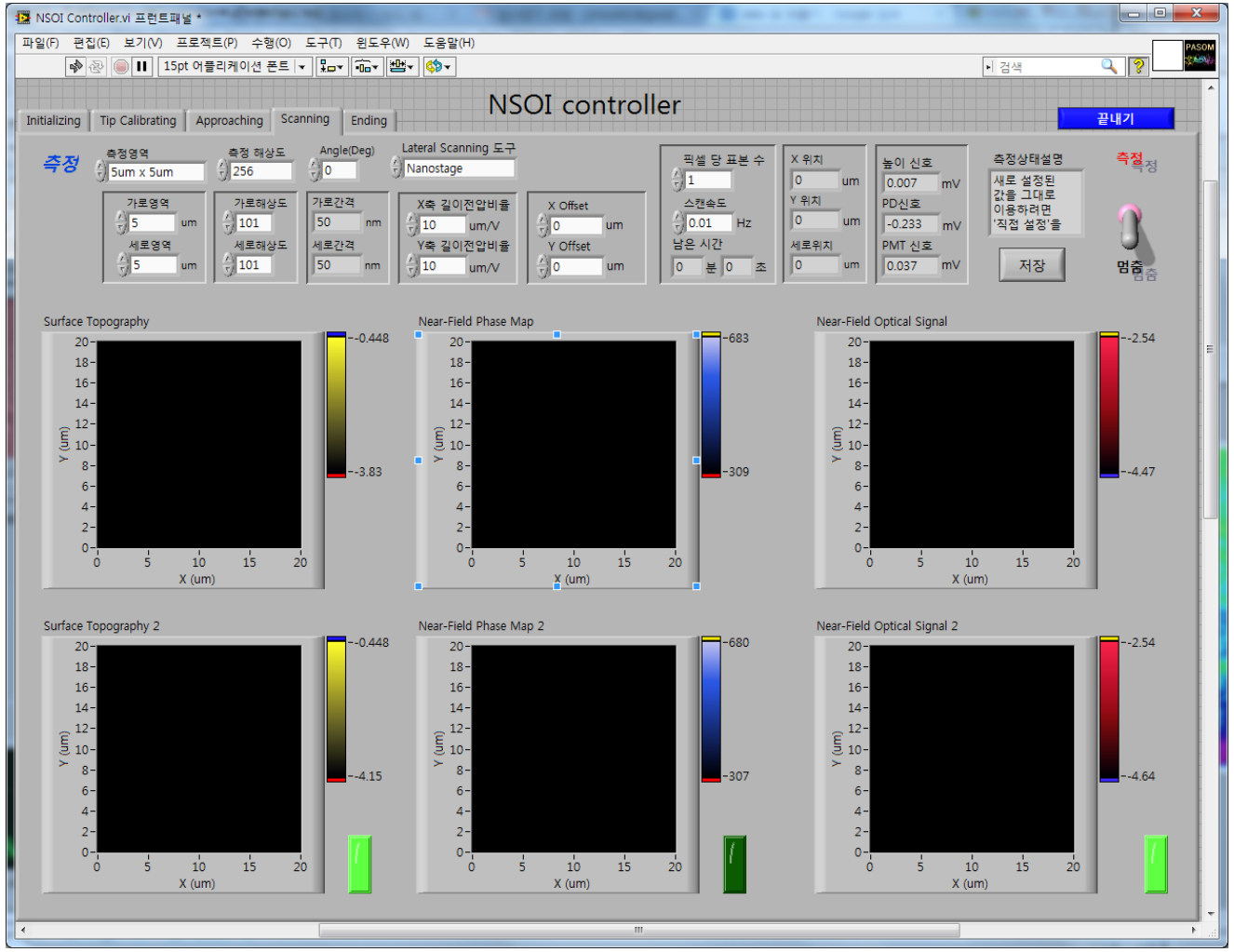


Figure 2-9: Scanning part of operation program

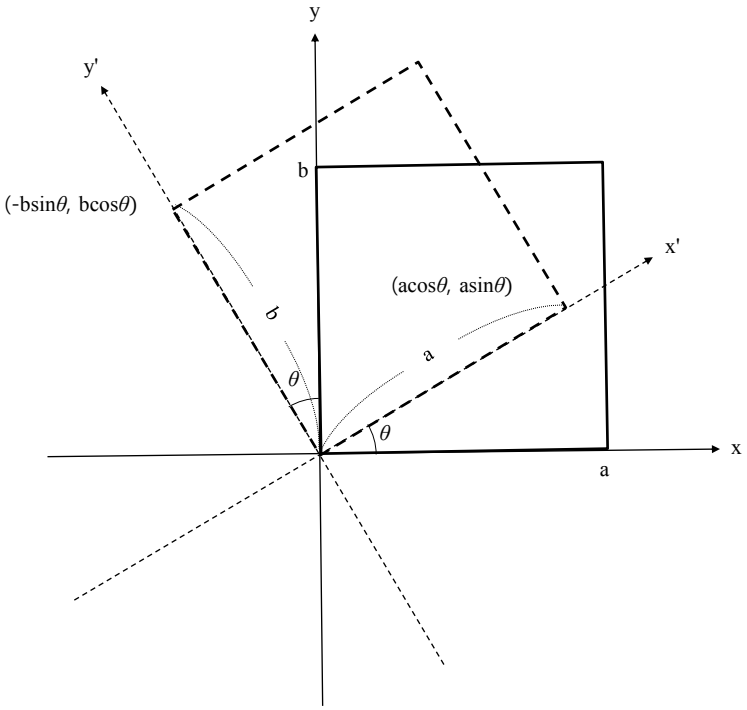


(a)

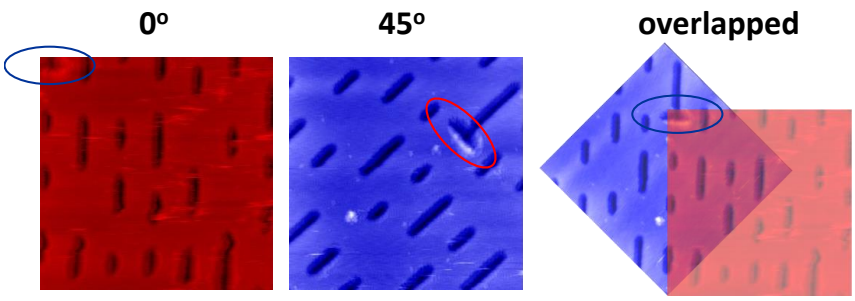


(b)

Figure 2-10: (a) Basic principle to tilt the scanning angle. (b) Tilt scanning test for CD surface.

scanning angle. If the scanning is performed for the direction of square dots not for the solid one, the voltage which is supplied to the two scanning axes should also be changed. Let the scanning steps for each axis are $a$ and $b$. Since tilted length steps for nano-positioning stage can be calculated by multiplying rotational matrix to original coordinates,

$$\begin{pmatrix} x' \\ y' \end{pmatrix} = \begin{pmatrix} \cos\theta & -\sin\theta \\ \sin\theta & \cos\theta \end{pmatrix} \begin{pmatrix} x \\ y \end{pmatrix} \tag{2.1}$$

new scanning step should have ($a\cos\theta$, $a\sin\theta$) and (-$b\sin\theta$, $b\cos\theta$) in order to tilt the scanning angle. If the sample has directionality in lateral plane, the results are expected to be influenced by the direction. Therefore, this function can be helpful.

Figure 2-10 (b) is an example of tilting scanning angle for the CD surface topography. The red and blue images are achieved by scanning the surface of CD starting from the same position. When one of them is rotated by 45 degrees, they are exactly matched.

When the signals are too weak, accumulation of the signals can be useful to enhance the signal-to-noise (S/N) ratio. Therefore, the accumulation option for each pixel is placed in the program. In this program, the minimum to maximum output voltages to translate the nano-positioning stage are divided by the number of pixels. The accumulation number of input signals are collected by the analog-to-digital converters (ADCs) in the DAQ board. The accumulated data are averaged for each pixel.

There are two general scanning schemes; bidirectional and unidirectional. Faster speed can be achieved by using bidirectional scanning, but there can be deformation between alternate lines. In this system, unidirectional scanning scheme is chosen but the two different images for each channel are obtained by both forward and back-

ward directions.

### 2.3.5 Ending

The ending part is used to finish the experiment. It is composed of tip-detachment, PI feedback off and initializing $x, y$ and $z$ positions. Since the probe tip maintains the distance near the surface, tip should be detached after the measurement. This process can be operated by using the PZT actuator or the picomotor actuator. First, the probe should be detached by using the PZT actuator because operating picomotor actuator can make vibration in the system. Feedback-on state is maintained until the detachment process is completed.

At the end of the experiment, it is good to move the nano-positioning stage back to the initial position by applying the voltages to zeros. If not, the final voltages in the previous experiment will be applied to the stage when the instruments turn on. Then the stage will abruptly moves to the final position of the previous experiment. *Initializing x, y and z position* button makes the DAQ board to apply the zero voltages to the stage. Each option can be turned on or off when they are needed, or the whole process can be performed all at once.

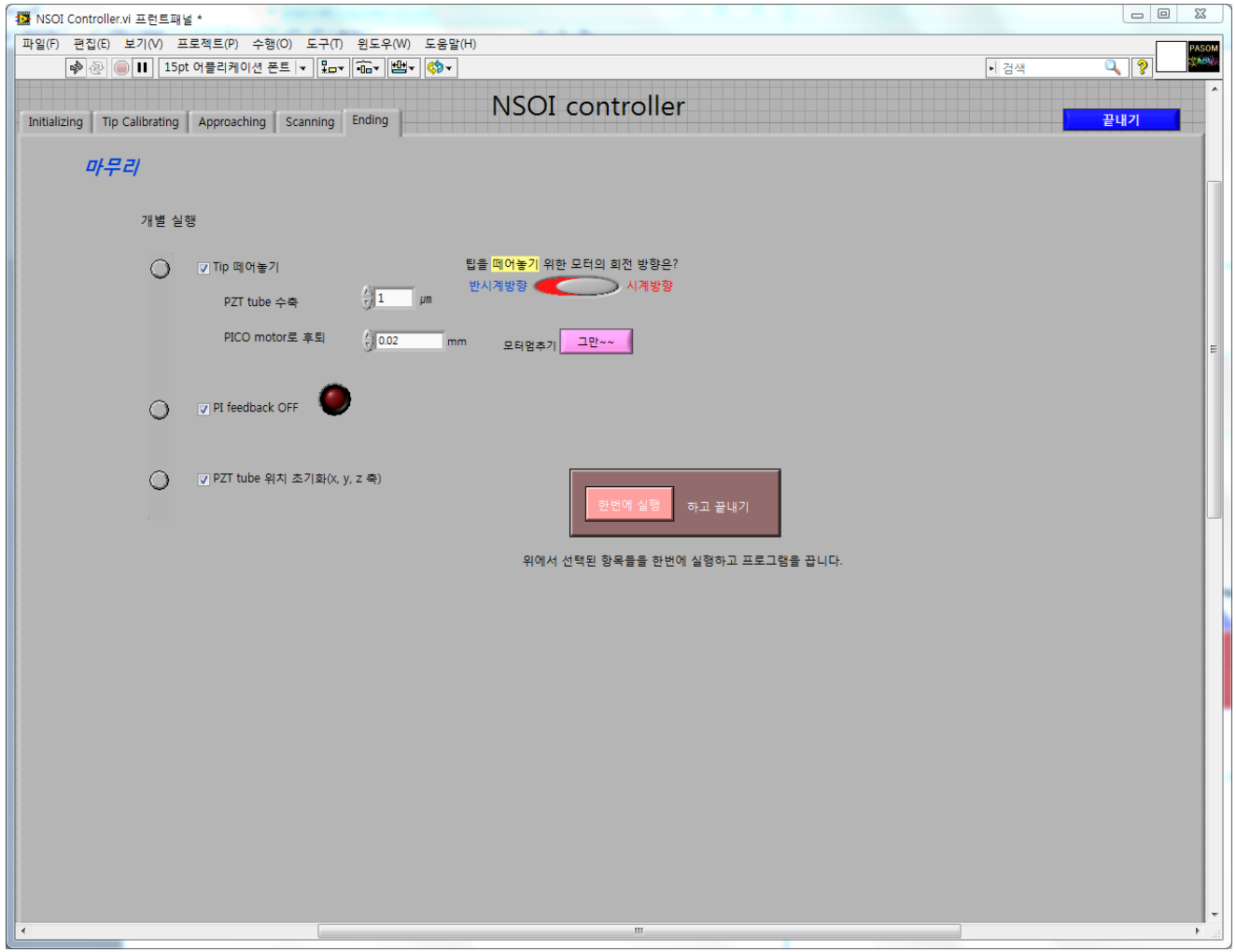


Figure 2-11: Ending part of operation program

## 2.4 Reference Sample

After the hardware and software are all prepared, it should be checked that the system is working well. Two test gratings produced for SPM (*NT-MDT*'s TGQ1 and μ*masch*'s TGX01P) are selected to test the system. TGQ1 is a Si wafer based grating. The patterns are consisted of 3-dimensional array of small rectangles. The height of each rectangle is 20 nm $\pm$ 1.5 nm and the period is 3 μm $\pm$ 0.05 μm. TGX01P is a chessboard-like array of square pillars with sharp undercut edges. The depth is 190 nm and the period is 3 μm $\pm$ 5 nm.

In Figure 2-12, the two dimensional scanning surface topography and the cross section for each grating are shown. The S/N ratio for TGQ1 is not great, but the rectangles with 20 nm height are clearly distinguished. The diameter of the fiber tips ($\sim$ 200 nm) makes this noise. The image of TGX01P exhibits better S/N ratio because the depth of sample is about of 190 nm, $\sim$ 10 times deeper than 20 nm.

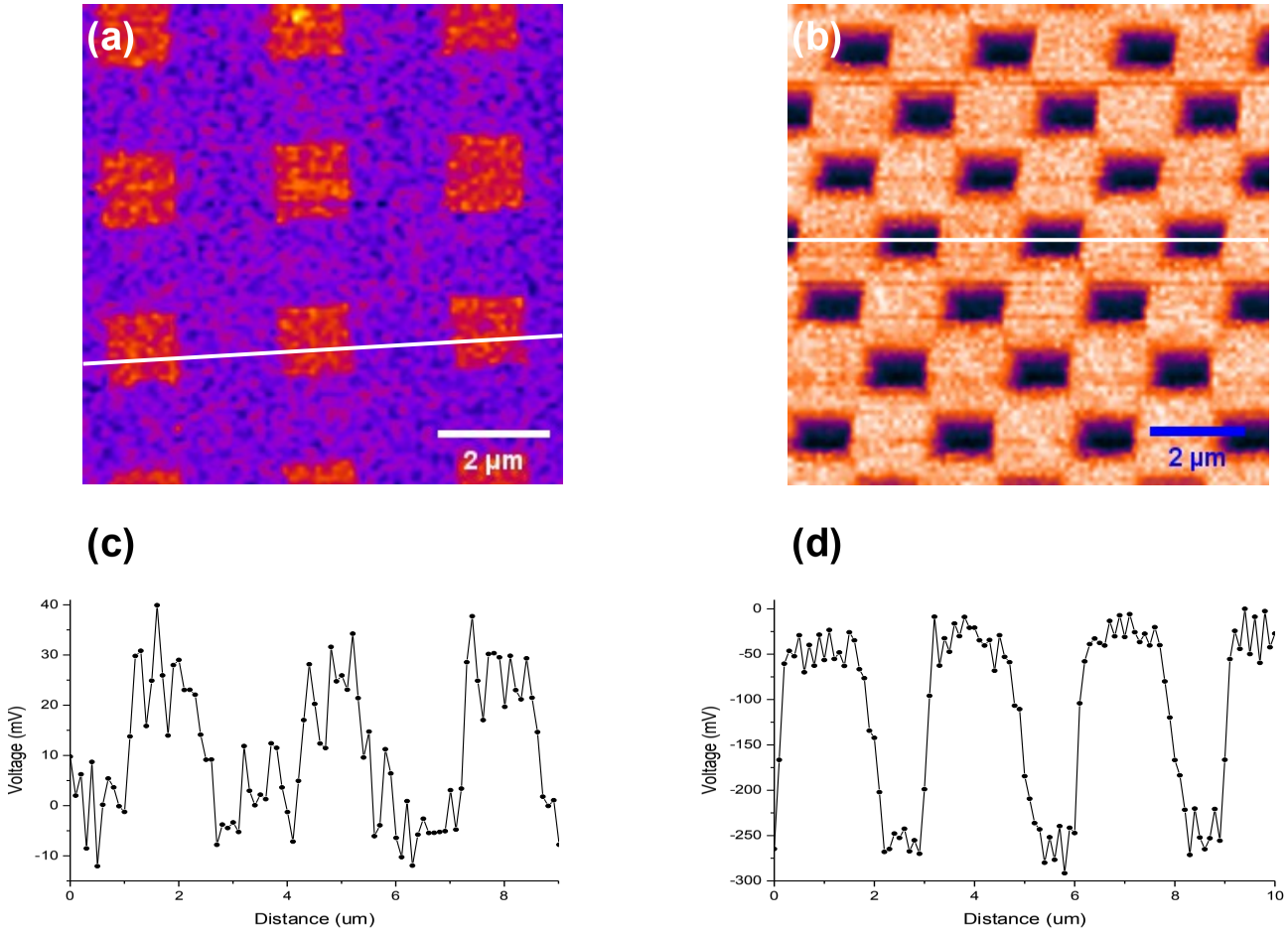


Figure 2-12: Surface topography for the standard samples: (a) TGQ1 (b) TGX01P (c) Cross section for TGQ1 (d) Cross section for TGX01P

## 2.5 Summary

In this chapter, the NSOM system and the operation software are described. The distance regulation system is based on the shear-force detection by using a quartz crystal tuning fork, which has the resonance frequency of 32.768 kHz. The NSOM unit is composed of various electronic devices. Main components are head, head controller, PI feedback controller, lock-in amplifier, picomotor actuator, nano-positioning stage, DAQ board, PD and PMT. They are all connected to each other and usb or GPIB protocol are used for communication. By using this instrument, quality factor of about 3000 can be achieved.

Since the NSOM system is controlled by computer, operating program should be constructed. *National Instruments*' LabVIEW is the programming language to build the operating program. The program is composed of 5 parts: initializing, tip calibrating, approaching, scanning and ending. All the parts are combined organically and they exchange the information with one another.

Two reference gratings used for SPM are tested to confirm the availability of our system. Square patterns are repeated 2-dimensionally for these gratings. The grating patterns are well-measured by the shear-force detection system. The distance regulation system is confirmed by this test. Especially, almost 20 nm resolution in depth of TGQ1 can be achieved.

# Chapter 3

# Near-field Scanning Optical Interferometer

## 3.1 Introduction

Light is not only a particle (photon) but also wave. Therefore, various phenomena such as interference and diffraction can be explained by wave nature of light. Interference displays a fundamental property of wave. Interference in electromagnetic wave (i.e. light) has been a historical issue in natural sciences.

When more than two waves are met, the total intensity is given by the square of the summation of the amplitudes. This is called *linear superposition principle*.

$$I = \left[ \sum_i \vec{E}_i \right]^2 \tag{3.1}$$

The electromagnetic waves can be written by,

$$\vec{E}_i = \vec{E}_{0i} e^{i(\vec{k}_i \cdot \vec{r} - \omega t + \varphi_i)} \tag{3.2}$$

Therefore, the total intensity by interfering two electromagnetic waves in vacuum can be written by

$$\begin{aligned} I &= \frac{1}{2}\epsilon_0 c \left\{ \vec{E}_{01} e^{i(\vec{k}_1\cdot\vec{r}-\omega t+\varphi_1)} + \vec{E}_{02} e^{i(\vec{k}_2\cdot\vec{r}-\omega t+\varphi_2)} \right\} \\ &\quad \times \left\{ \vec{E}_{01} e^{-i(\vec{k}_1\cdot\vec{r}-\omega t+\varphi_1)} + \vec{E}_{02} e^{-i(\vec{k}_2\cdot\vec{r}-\omega t+\varphi_2)} \right\}^* \\ &= \frac{1}{2}\epsilon_0 c \left\{ |\vec{E}_{01}|^2 + |\vec{E}_{02}|^2 + 2\vec{E}_{01}\cdot\vec{E}_{02}\cos(\vec{k}_1\cdot\vec{r} - \vec{k}_2\cdot\vec{r} + \varphi_1 - \varphi_2) \right\} \end{aligned} \tag{3.3}$$

In other words,

$$I = I_1 + I_2 + 2\sqrt{I_1 I_2}(\hat{u}_1\cdot\hat{u}_2)\cos(\alpha_1 - \alpha_2) \tag{3.4}$$

where $\alpha_i = \vec{k}_i\cdot\vec{r} + \varphi_i$ and $\hat{u}_i$ is the unit vector in polarization direction of $\vec{E}_{0i}$. The last term $2\sqrt{I_1 I_2}(\hat{u}_1\cdot\hat{u}_2)\cos(\alpha_1 - \alpha_2)$ can be considered as a *interference term*.

The interference term is maximum when $\hat{u}_1 \,//\, \hat{u}_2$. If the polarizations of two electric fields are perpendicular (i.e. $\hat{u}_1 \perp \hat{u}_2$), the interference term is equal to 0, meaning that there will be no interference regardless of the phase difference.

If the polarizations are parallel to each other (i.e. $\hat{u}_1 \,//\, \hat{u}_2$), the total intensity can be written as,

$$I = I_1 + I_2 + 2\sqrt{I_1 I_2}\cos(\alpha_1 - \alpha_2) \tag{3.5}$$

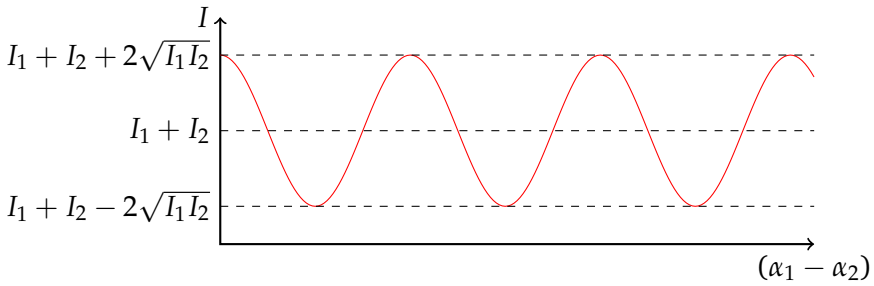


Therefore, the intensity depends on the phase difference $\Delta\alpha = \alpha_1 - \alpha_2$ and varies between $I_{max} = I_1 + I_2 + 2\sqrt{I_1 I_2}$ and $I_{min} = I_1 + I_2 - 2\sqrt{I_1 I_2}$.

Since the fringe visibility is defined as

$$V = \frac{I_{max} - I_{mim}}{I_{max} + I_{mim}}, \tag{3.6}$$

we can get

$$V = \frac{2\sqrt{I_1 I_2}}{I_1 + I_2} \tag{3.7}$$

by using the equation (3.5). If $I_1$ and $I_2$ have the same value $I_0$, $V$ can be the maximum value of 1 and the total intensity is going to be $I = 2I_0(1 + \cos(\alpha_1 - \alpha_2)) = 4I_0 \cos^2 \frac{\alpha_1 - \alpha_2}{2}$.

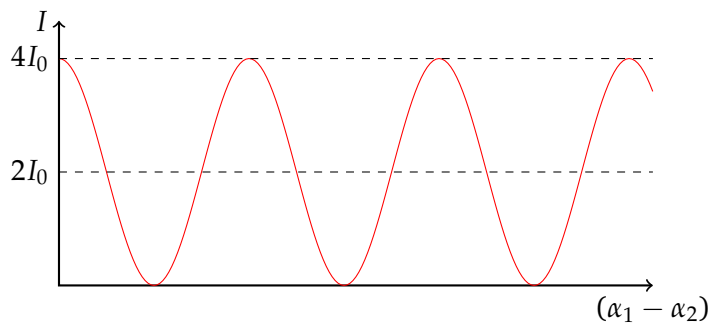

## 3.2 Near-field Scanning Optical Interferometer

When two coherent beams meet in the same area, they can make interference because of phase difference. The phase of light originate from the optical path-length difference (OPD). OPD is defined by

$$(\mathrm{OPD}) = \Delta(nl) \tag{3.8}$$

where $n$ is refractive index of material and $l$ is the path-length. Since the speed of light is defined by $v = c/n$, the light in material travels slower than that in vacuum because of the refractive index $n$,

By measuring the phase difference, the optical property of material can be determined. Near-field scanning optical interferometer (NSOI) is an instrument to detect phase variation by combining NSOM with interferometry. By using the NSOI, the localized phase difference can be measured with nanometric scale. Therefore, NSOI can play an important role for the transparent nano-materials such as biological molecular structure and condensed matter. OPD is chosen for the *figure of merit* of this system. In this chapter, NSOI will be described with the main idea.

### 3.2.1 Setup

First of all, the light beam must be exactly focused on the sample surface. A Twyman-Green interferometric setup is constructed for this purpose. The beam from the light source is divided by beam-splitter. One of them passes through the objective lens and reflects at the sample surface. The other one is reflected at the flat window. The later acts as a reference arm. The good fringe visibility can be obtained when the intensities of the two beams are similar (equation (3.7)). Therefore, not a mirror but a flat window is used to achieve the higher fringe contrast. Moreover, in order

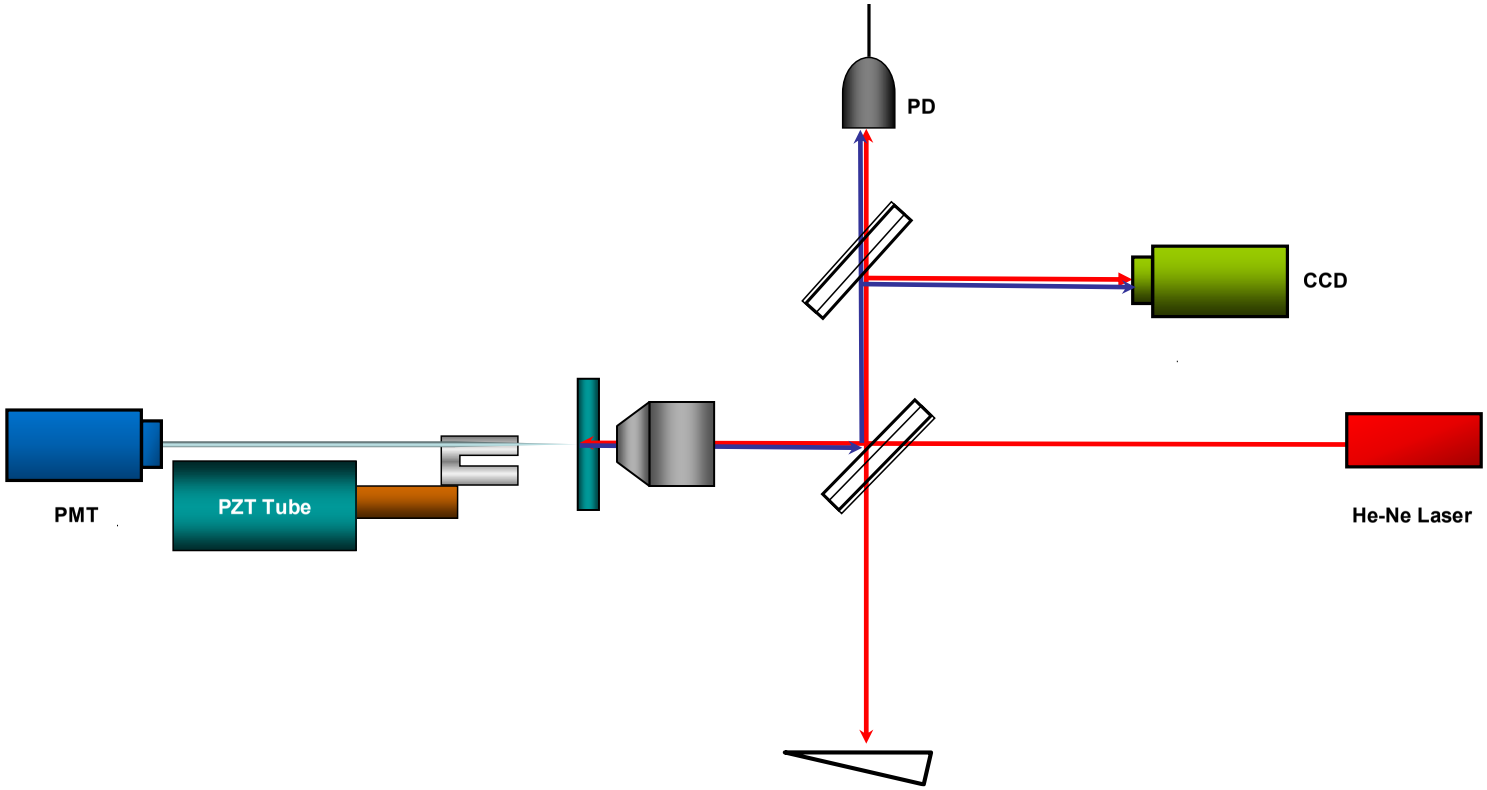


Figure 3-1: Schematic diagram of near-field scanning optical interferometry

to prevent the interruption by reflection from the back side of the window, the edge prism is introduced. If the light is exactly focused on the sample surface, linear fringe pattern can be observed. After getting straight line fringes, beam from the reference arm is blocked. And then, a sharp fiber tip of NSOM is approached to the focal point.

In this setup, reflected light from the tip can be considered as a point-like source. It interferes with the light reflected at the sample surface. The interference pattern may be varied by the phase information of light at each point. And the variation of phase of light should be affected by the optical property of material at that point. Therefore, phase variation of light can be measured by scanning the surface 2-dimensionally with resolution of NSOM. This information is directly related to the localized optical property of the sample surface. Since NSOI uses the same system as NSOM, surface topography, near-field collection signal, and 2D phase map can be obtained simultaneously. Figure 3-1 shows the schematic diagram of NSOI setup.

## 3.3 Removing Background Signal

### 3.3.1 Removing Background Signal

Figure 3-2 shows the basic concept to remove the background signal and extract pure-phase information of light in NSOI measurement. When the NSOM fiber tip approaches to the sample surface and laser beam is focused at the tip's position, some portion of the beam is reflected at the surface (let this field $E_{r,s}$) and remaining portion is transmitted (let this field $E_t$). And some portion of $E_t$ is reflected at the end of the tip. Let this field $E_{r,\mathrm{tip}}$. From equation (3.5), the total intensity which is achieved at the reflection side can be represented by

$$I_{tot}(x,y) = I_{r,\mathrm{tip}}(x,y) + I_{r,\mathrm{s}}(x,y) + 2\sqrt{I_{r,\mathrm{tip}} I_{r,\mathrm{s}}} \cos\left\{\alpha_{r,\mathrm{tip}}(x,y) - \alpha_{r,\mathrm{s}}(x,y)\right\} \quad (3.9)$$

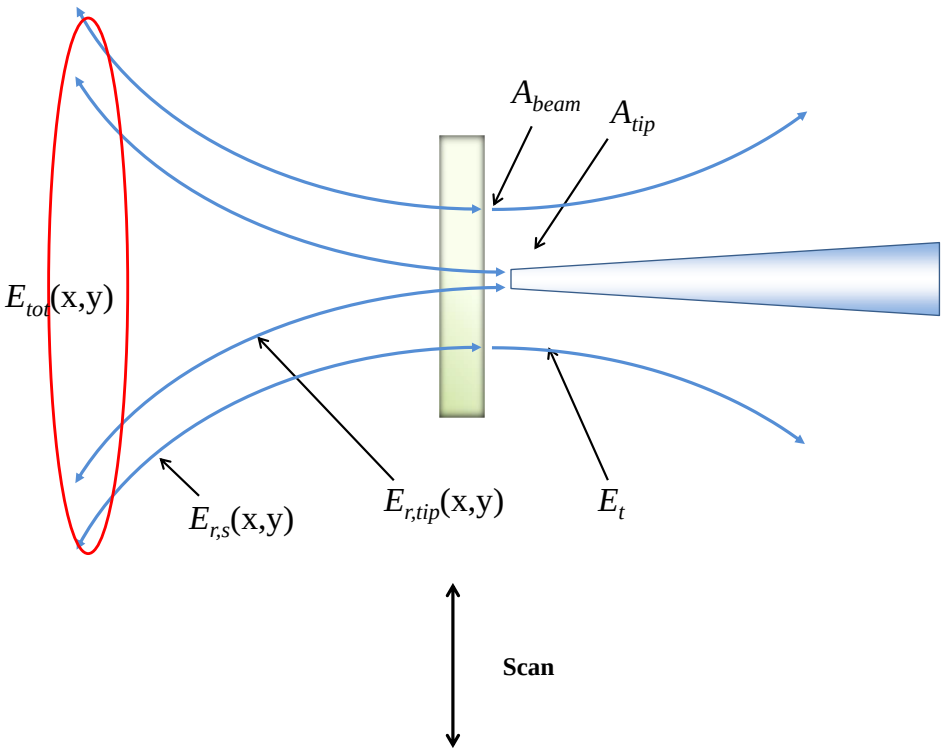


Figure 3-2: Basic concept to remove background signal

In this case, the multiple reflection is not considered and the polarizations are assumed parallel.

Let's assume that $\alpha_{r,s}(x,y)$ is a constant for all the scanning area. This assumption is acceptable in general, because the diameter of tip is much smaller than that of reflection area at sample surface. Then, $\alpha_{r,s}(x,y)$ can be set as 0.

$$I_{tot}(x,y) = I_{r,\text{tip}}(x,y) + I_{r,s}(x,y) + 2\sqrt{I_{r,\text{tip}} I_{r,s}} \cos\left\{\alpha_{r,\text{tip}}(x,y)\right\} \tag{3.10}$$

Therefore, cosine of the phase difference between the fields can be achieved as,

$$\cos\left\{\alpha_{r,\text{tip}}(x,y)\right\} = \frac{I_{tot}(x,y) - I_{r,\text{tip}}(x,y) - I_{r,s}(x,y)}{2\sqrt{I_{r,\text{tip}}(x,y) I_{r,s}(x,y)}} \tag{3.11}$$

Let's assume that the electric field fully transmits the sample after the field is reflected at tip. In real experimental condition, the field cannot be totally transmitted. However, in case of transparent material, the portion of the reflection is small compared to the transmission, and so it can be ignorable. Since the intensity of the light is proportional to the area of the beam, $I_{r,\text{tip}}$ can be represented as,

$$I_{r,\text{tip}}(x,y) = I_t(x,y) \times \frac{A_{\text{tip}}}{A_{\text{beam}}} \times R_{\text{tip}} \tag{3.12}$$

$R_{\text{tip}}$ is the reflectance of the tip.

If the absorption of the material is ignorable, the reflectance and transmittance can be considered as [Griffiths, 2012; Wangsness, 1986],

$$R + T = 1 \tag{3.13}$$

If the sample is thin enough, the effect of sample for transmission can be neglected.

Therefore, equation (3.13) can be written as,

$$\left(\frac{E_{r,\mathrm{s}}(x,y)}{E_i}\right)^2 + \frac{n_{\mathrm{air}}}{n_{\mathrm{sub}}}\left(\frac{E_t(x,y)}{E_i}\right)^2 = 1 \tag{3.14}$$

or

$$\left(\frac{E_t(x,y)}{E_i}\right)^2 = \frac{n_{\mathrm{sub}}}{n_{\mathrm{air}}}\left\{1 - \left(\frac{E_{r,\mathrm{s}}(x,y)}{E_i}\right)^2\right\} \tag{3.15}$$

Let's substitute equation (3.15) to equation (3.12),

$$\left(\frac{E_{r,\mathrm{tip}}(x,y)}{E_i}\right)^2 = \frac{n_{\mathrm{sub}}}{n_{\mathrm{air}}}\left\{1 - \left(\frac{E_{r,\mathrm{s}}(x,y)}{E_i}\right)^2\right\}\frac{A_{\mathrm{tip}}}{A_{\mathrm{beam}}} \times R_{\mathrm{tip}} \tag{3.16}$$

If the denominator and the numerator are divided by $\frac{1}{2}\epsilon_0 c E_i^2$ in equation (3.11), $\cos\left\{\alpha_{r,\mathrm{tip}}(x,y)\right\}$ is going to be,

$$\cos\left\{\alpha_{r,\mathrm{tip}}(x,y)\right\} = \frac{\left(\frac{E_{\mathrm{tot}}(x,y)}{E_i}\right)^2 - \left(\frac{E_{r,\mathrm{tip}}(x,y)}{E_i}\right)^2 - \left(\frac{E_{r,\mathrm{s}}(x,y)}{E_i}\right)^2}{2\frac{E_{r,\mathrm{tip}}(x,y)}{E_i}\frac{E_{r,\mathrm{s}}(x,y)}{E_i}} \tag{3.17}$$

If equation (3.16) is substituted into equation (3.17), $\cos\left\{\alpha_{r,tip}(x,y)\right\}$ can be calculated as,

$$\cos\left\{\alpha_{r,\mathrm{tip}}(x,y)\right\} = \frac{\left(\frac{E_{tot}(x,y)}{E_i}\right)^2 - R_{\mathrm{tip}}\frac{n_{\mathrm{sub}}}{n_{\mathrm{air}}}\left\{1 - \left(\frac{E_{r,\mathrm{s}}(x,y)}{E_i}\right)^2\right\}\frac{A_{\mathrm{tip}}}{A_{\mathrm{beam}}} - \left(\frac{E_{r,\mathrm{s}}(x,y)}{E_i}\right)^2}{2\frac{E_{r,\mathrm{s}}(x,y)}{E_i}\sqrt{R_{\mathrm{tip}}\frac{n_{\mathrm{sub}}}{n_{\mathrm{air}}}\left\{1 - \left(\frac{E_{r,\mathrm{s}}(x,y)}{E_i}\right)^2\right\}\frac{A_{\mathrm{tip}}}{A_{\mathrm{beam}}}}} \tag{3.18}$$

Each term in the right-hand side of equation (3.18) can be explained by physical parameters in real experimental situation. If a photo-detector is located at the reflected side, the measured voltage is proportional to the intensity of the light.

Let's assume two different measurement. One of them is measured by approaching the NSOM fiber tip. In this case, the measured data is related to $E_{tot}^2(x,y)$. On the other hand, $E_{r,s}^2(x,y)$ is related to the situation when the measurement without tip approaching.

If the measured voltage for surface reflection is $V_{r,s}(x,y)$ is proportional to $I_{r,s}(x,y)$ and,

$$\left(\frac{E_{r,s}(x,y)}{E_i}\right)^2 = R_{r,s}(x,y) \tag{3.19}$$

where $R_{r,s}$ is the reflectance of the surface, then,

$$(E_{r,s}(x,y))^2 = R_{r,s}(x,y) \times E_i^2 \tag{3.20}$$

$$V_{r,s}(x,y) \propto I_{r,s}(x,y) \propto (E_{r,s}(x,y))^2 = R_{r,s}(x,y) \times E_i^2 \tag{3.21}$$

If the intensity of the incident light is not changed during the scanning time,

$$\frac{V_{r,s}(x,y)}{R_{r,s}(x,y)} = \text{const.} \tag{3.22}$$

If the reflectance of the substrate is already known, it can be the reference for the whole area. In the case of quartz substrate, the reflectance is around 4 %.

Let the reference position be $(x_0, y_0)$. Since $V_{r,s}(x,y)$ is already measured for the whole scanning area, the reflectance for each point can be calculated by the following equation.

$$\left(\frac{E_{r,s}(x,y)}{E_i}\right)^2 = R_{r,s}(x,y) = V_{r,s}(x,y) \times \frac{R_{r,s}(x_0,y_0)}{V_{r,s}(x_0,y_0)} \tag{3.23}$$

The similar process can be applied to the case of $\left(\frac{E_{r,\text{tot}}(x,y)}{E_i}\right)^2$.

$$\left(\frac{E_{r,\mathrm{tot}}(x,y)}{E_i}\right)^2 = R_{r,\mathrm{tot}}(x,y) = V_{r,\mathrm{tot}}(x,y) \times \frac{R_{r,\mathrm{tot}}(x_0,y_0)}{V_{r,\mathrm{tot}}(x_0,y_0)} \tag{3.24}$$

From this result, the two-dimensional map of $\cos\left\{\alpha_{r,\mathrm{tip}}(x,y)\right\}$ or $\alpha_{r,\mathrm{tip}}(x,y)$ can be obtained by equation (3.18).

### 3.3.2 LabVIEW Program

Figure 3-3 shows the phase extraction program produced by LabVIEW. This program is constructed to calculate the phase from the experimental data for all points of scanning area. Basic algorithm is explained already. Based on the algorithm, $V_{r,s}(x_0,y_0)$ and $V_{r,\mathrm{tot}}(x_0,y_0)$ are required to extract the phase. In realistic experimental situation, the surface scanning should be carried out twice. First, the scanning is performed as usual NSOM experiment which means that the fiber probe tip is approached. This result represents $V_{r,\mathrm{tot}}(x_0,y_0)$. After that, the tip is removed and the only reflected light is scanned over the exact same area as the first scanning. This means $V_{r,\mathrm{s}}(x_0,y_0)$.

This program imports these two data, and calculate the phase based on the equation (3.18). Note that $R_{\mathrm{tip}}, n_{\mathrm{sub}}, n_{\mathrm{air}}, A_{\mathrm{tip}}, A_{\mathrm{beam}}$ should be provided.

### 3.3.3 Two Examples Which Can Make Phase Difference

The phase difference originates from OPD between two positions. When two coherent lights interfere, the phase difference $\alpha$ is given by $2\pi/\lambda \times (\mathrm{OPD})$. Since OPD is defined by $\Delta(nl)$, the simplest cases which can be considered are 1) when the sample has constant refractive index but the depth is different and 2) when the sample is flat but the refractive index is different for measured position. These are illustrated in Figure 3-4.

The measured phase difference is combination of these two cases. NSOI can

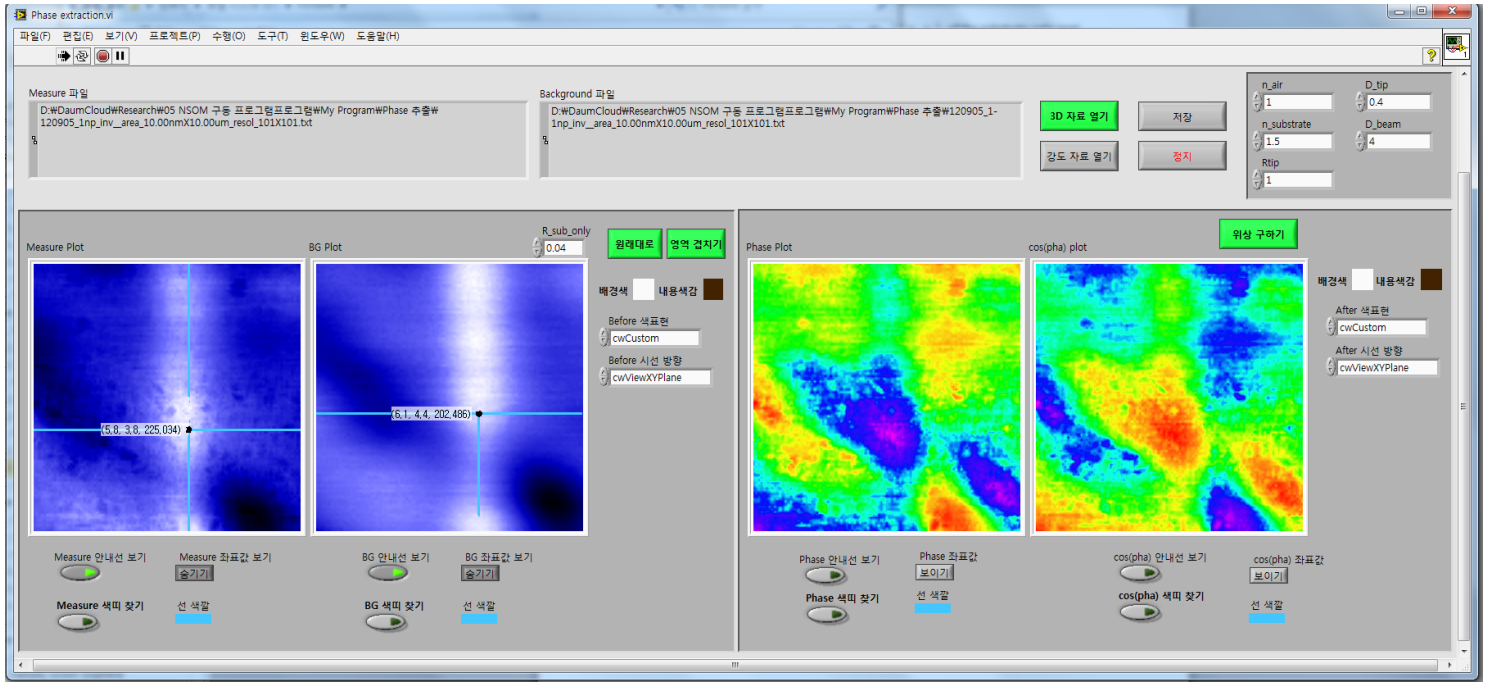


Figure 3-3: Phase extraction program constructed by using LabVIEW programming language

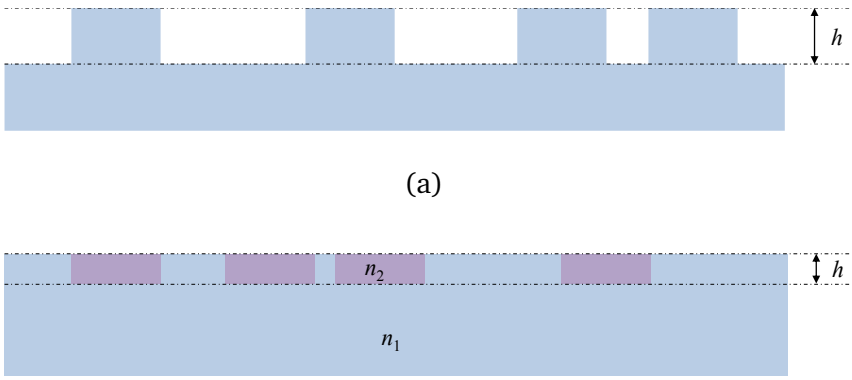


Figure 3-4: Two examples to make phase variations. (a) Constant refractive index with different depth and (b) constant depth with different refractive index.

detect the phase variation with nanometric scale because of the sharp tip-end of the fiber probe.

### (a) Case 1: Constant Refractive Index with Different Depth

If a homogeneous material has height profile, OPD can be deduced by,

$$(OPD) = \Delta(nl) = n\Delta l \tag{3.25}$$

Figure 3-4 (a) shows this case. In this case, the phase $\alpha_1$ is,

$$\alpha_1 = \frac{2\pi}{\lambda} n(\Delta l) = \frac{2\pi}{\lambda} nh \tag{3.26}$$

### (b) Case 2: Constant Depth with Different Refractive Index

If a sample has flat surface but the refractive index varies with the positions, OPD can be deduced by,

$$(OPD) = \Delta(nl) = l\Delta n \tag{3.27}$$

Figure 3-4 (b) shows this case. In this case, the phase $\alpha_2$ is,

$$\alpha_2 = \frac{2\pi}{\lambda}(\Delta n)l = \frac{2\pi}{\lambda}(n_2 - n_1)h \tag{3.28}$$

## 3.4 Test for the Algorithm: Reference Sample and Optical Discs

As explained in the previous section, the sample for NSOI experiment should be transparent. Since the test gratings to check the distance regulation system (TGQ1 and TGX01P) are based on opaque silicon substrate, they are not suitable for this purpose.

SNG01 (*NT-MDT Co.*) is a kind of test grating for scanning probe microscopes (SPMs). Since it has transparent quartz substrate, SNG01 can be a good sample to test the performance of NSOI. Another test samples are specially prepared optical discs. They are composed of uniform material but there are repeated height modifications on the surface. The size of each pattern can be reduced to be about 120 nm (in the case of blu-ray disc). Therefore, optical discs also can be suitable for phase measurement. In this chapter, SNG01 and various type of bare optical discs are employed to verify the phase measurement system.

### 3.4.1 SNG01

#### (a) Surface Profile

SNG01 is widely used for NSOM testing, not for AFM. Since the pattern and the substrate are composed of different material, the atomic force between AFM cantilever tip and the material can be also different. About 20 to 30 nm thick rhombus shape vanadium layers are periodically coated on quartz substrate. SNG01 is suitable to test that the instrument is well working for high-resolution imaging as well as the surface profiling because the transmissions through and reflection from the metal are different from them of the quartz substrate.

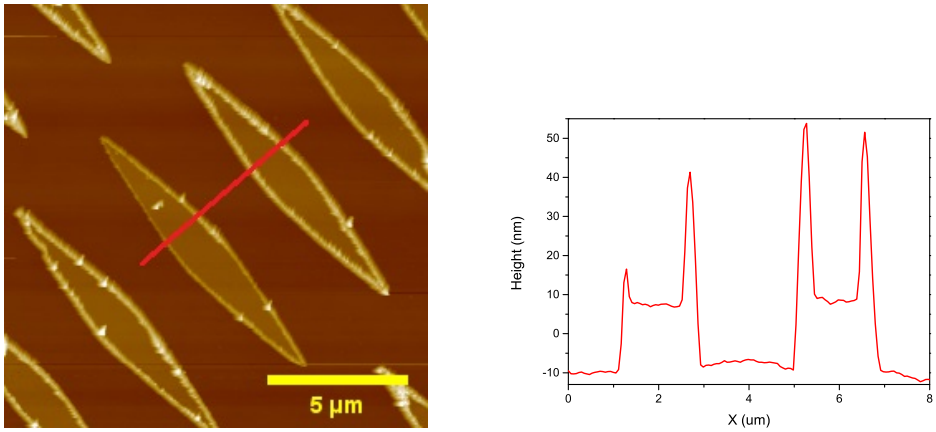


(a) (b)

Figure 3-5: Surface topography of SNG01 achieved by AFM

Figure 3-5 shows the surface topography of SNG01 by using AFM. AFM measurements were performed in non-contact mode in order to minimize damage on the sample during scanning. The vanadium pattern has the height of 20 nm. The rhombus shape can be clearly seen in the surface topography. Besides, there are sharp edges at the interface between the vanadium and the quartz.

Similar topography obtained by AFM can be also acquired by the tuning fork based distance regulation of NSOM. Figure 3-6 shows the surface topography of SNG01 by using NSOM. Periodic vanadium rhombus patterns also can be imaged by the shear-force detection. The shape edges of the rhombus are also detected. Since the NSOM fiber tip has aperture at the end of the tip, the diameter of the NSOM tip is larger than the AFM's one. Moreover, NSOM's tip do not have the spherical tip edge. Therefore, the surface image is not as clear as the AFM measurement, but the similar surface information can be observed.

### (b) Phase Measurement

As interpreted in the previous section, the phase information by the tip-end reflected light is obtained by photo detector in superposed state with the surface reflection. To subtract the phase only, background signals are obtained for the area which the NSOI experiment performed. Figure 3-7 shows the process to obtain phase information of SNG01.

Figure 3-7 (a) shows the surface topography. The optical signal achieved by PD is shown in Figure 3-7 (b). Figure 3-7 (a) and (b) are obtained simultaneously. They have similar variations at the edges of the vanadium patterns. At the end of the rhombus, there are repeated dark spots between the patterns at the map of optical signals. Since these patterns are irrelevant to the existence of the fiber probe, they should be removed.

For this purpose, the surface scanning performed again when the NSOM fiber probe tip moved away. The result is shown in Figure 3-7 (c). Similar dark spots can be found by comparing 3-7 (b) and (c). Therefore, Figure 3-7 (c) can be considered as the background signals which should be removed. These two results are inserted to equation (3.18). Of course, (b) and (c) are corresponds to the $\left(\frac{E_{\mathrm{tot}}(x,y)}{E_i}\right)^2$ and

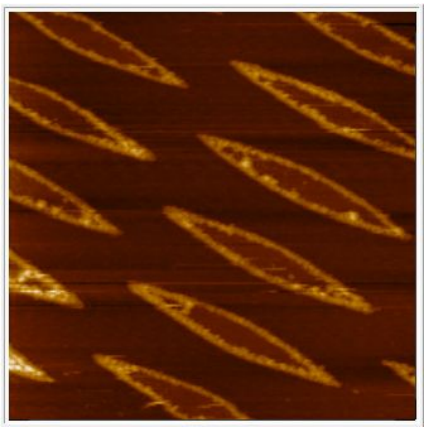

Figure 3-6: Surface topography of SNG01 achieved by NSOM

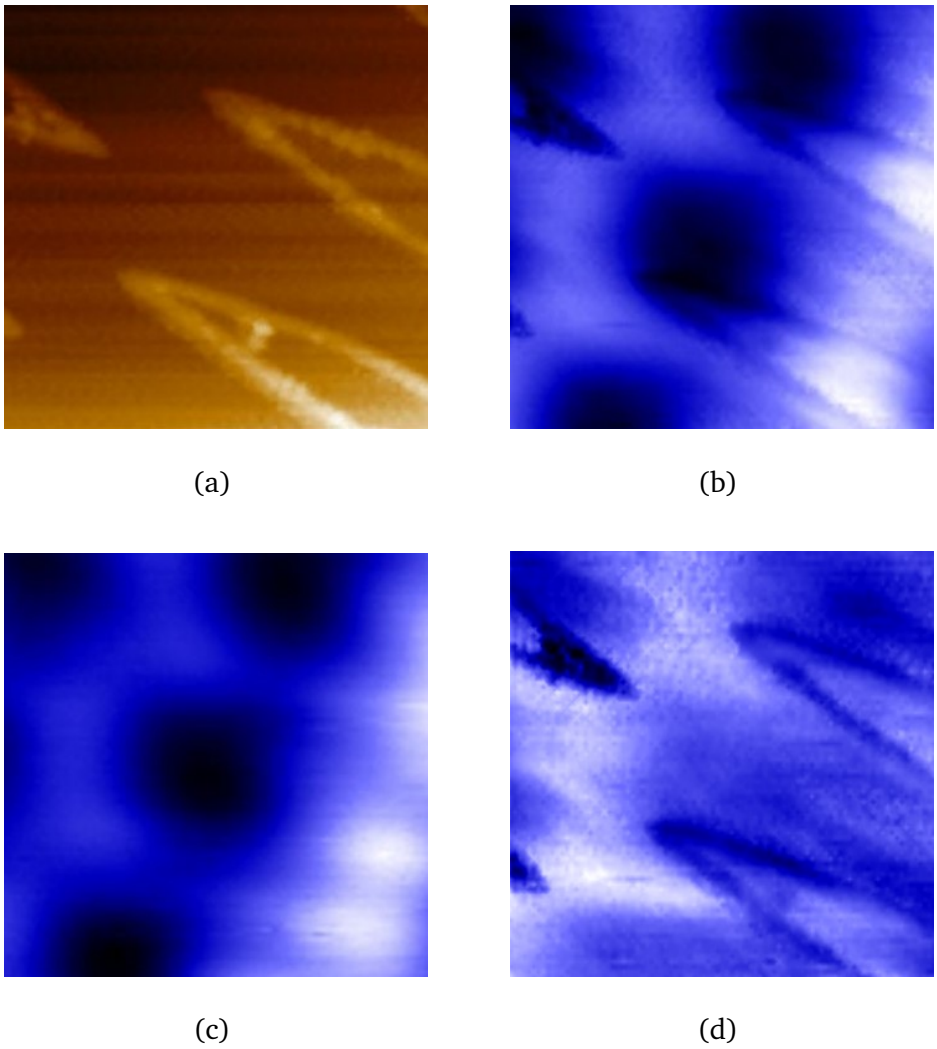


Figure 3-7: The results of NSOI measurement and phase extraction. (a) Surface topography. (b) NSOI measurement. (c) Back ground measurement. (d) Cosine of phase

$\left(\frac{E_{r,s}(x,y)}{E_i}\right)^2$ terms in equation (3.18), respectively.

The cosine of the phase map which is the intension of the experiment is obtained as Figure 3-7 (d). Comparing to (b), the background signals are successfully removed in (d). The contrast is also improved. Since vanadium is a metallic material, its index of refraction has real ($n$) and imaginary ($k$) parts. For the case of 632.8 nm wavelength, $n \sim 3.5$ and $k \sim 2.95$ [Palik, 1997]. Although the imaginary part can affect to the phase change, the phase difference between the materials is clearly distinguished in the result.

The phase difference originated from the optical density of the material can be determined with high depth and lateral resolution from this result. In next section, the phase variation in homogeneous material will be clearly obtained by performing NSOI experiment for the optical discs.

### 3.4.2 Bare Transparent Optical Discs

#### (a) Characteristics of the Sample

An optical disc is a flat, circular disc which has binary data in the form of pits and lands. When the optical disc is read, the reflection of the pits and lands are distinguishable. Pits have the binary value of 0 or off, and lands have the that of 1 or on. Periodic nano-structures are constructed on the polycarbonate substrate.

General optical disc manufacturing process can be divided into two parts: the first step is to make a stamper. The stamper is an original data plate to write data to optical disc. This process is called mastering. The stamper fabrication process is depicted in Figure 3-8 (a).

First, photo-resistor is applied to the polished glass, and data are recorded on the surface by laser beam. This is called *glass master*. Then, nickel (Ni) or silver

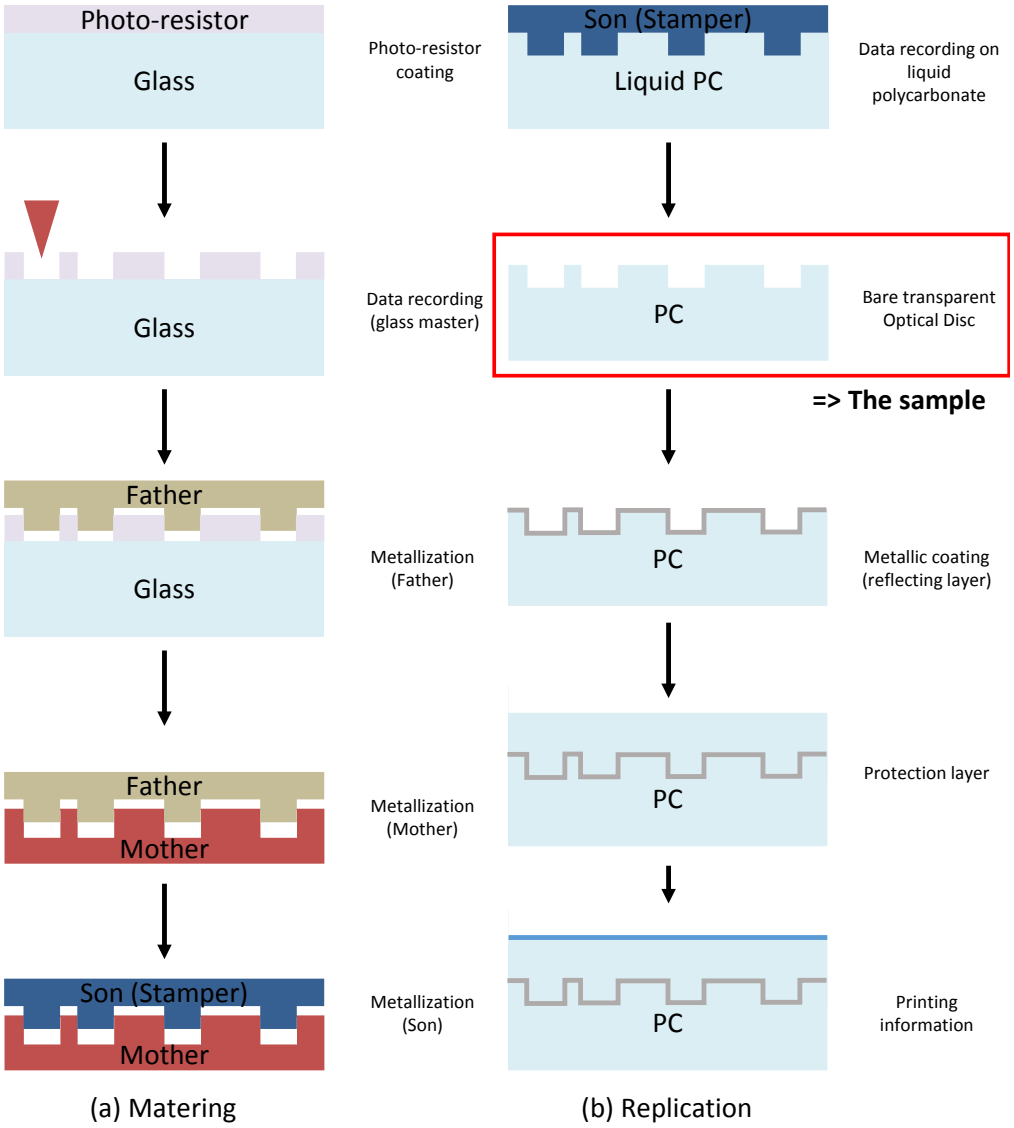


Figure 3-8: Optical disc fabrication process

(Ag) is plated to make the sample conductive. This step is called electroforming. By electroforming, a thick Ni layer is plated on the surface of the glass, and is detached from the glass. This is called *Father*. *Father* is used to create a metallic stamper called *Mother* which has opposite pattern to *Father*. And again, *Mother* is used to create *Son* which has the same pattern with *Father*. *Son* is the mostly used stamper to press the optical discs. After polishing the back-surface of the Ni plate and poring the center as the shape of disc, the stamper is achieved.

Using this stamper, mass production of optical discs is possible. Figure 3-8 (b) shows this process, which is called replication. Data are recorded by pressing stamper on liquid polycarbonate. Aluminum (Al) reflective layer is coated on this disc to read the data by laser diode. Subsequently, protection layer is coated to prevent the loss of data. After necessary information is printed out on the surface, the final optical disc is produced.

The optical discs can be divided by the amount of recordable data. The data storage capacity can be increased by reducing the distance between recorded pits (=track pitch). Various diameter of discs are possible. At present, 12 cm is the most common. The general characteristics for each optical disc is displayed in Table 3.1.

The first generation of optical storage is compact disc (CD). The data storage capacity of CD is 700 MB for a 12 cm disc. 780 nm laser diode is used to read the data. 80 minutes audio data in digital format is the first type of data record on CD.

Digital video disc (DVD) is the second generation of optical disc. It uses 650 nm laser diode to read the data. Data can be recorded in DVD by dual-layer. The single-layer DVD has the capacity of 4.7 GB. However, it can be increased to 8.5 GB when the data is recorded to dual-layer DVD. Video is the most common data format for DVD but other format also can be recorded on it.

Recently, blu-ray disc is commonly used for video recording because of the high-

definition (HD) video formats. It uses 405 nm blue laser diode to read data. It has the data storage capacity of 25 GB per layer. Dual layer discs (50 GB) is the standard for commercial market.

In conventional optical disc manufacturing process, aluminum reflecting layer should be coated on the bare polycarbonate disc to read the data by using proper laser diodes (ex) CD: $\lambda$=780 nm, DVD: $\lambda$=650 nm, Blu-ray Disc: $\lambda$=405 nm). However, NSOI needs the transparent sample to reflect at the tip end of the NSOM. Therefore, uncoated transparent discs (red square in Figure 3-8) are used to measure the phase information due to the pits and lands of the discs. The samples are specially prepared by *JMI Co., Ltd.*.

In this section, high-resolution phase map of the various optical discs are measured by using NSOI, and the results between them are compared.

| | CD | DVD | Blu-ray |
|---|---|---|---|
| Data storage capacity | 700 MB | 4.7 GB | 25 GB |
| Source to read data | 780 nm | 650 nm | 405 nm |
| Track pitch | 1600 nm | 740 nm | 320 nm |
| Minimum pit length | 850 nm | 400 nm | 149 nm |
| Pit width | $\sim$ 500 nm | $\sim$ 270 nm | $\sim$ 120 nm |
| Pit depth | $\sim$ 100 nm | $\sim$ 100 nm | $\sim$ 100 nm |

Table 3.1: Specification of optical discs

**(b) CD and DVD**

Track pitches (which means the distance between the center of adjacent tracks) of CD and DVD are larger than diffraction limit of the visible light (see Table 3.1). Therefore, each track can be easily distinguished by conventional microscope. Figure 3-9 shows the clearly resolved CD and DVD images from the conventional reflection type microscope by using objective lens of 40 ×. Each pit is observed like black spot as expected.

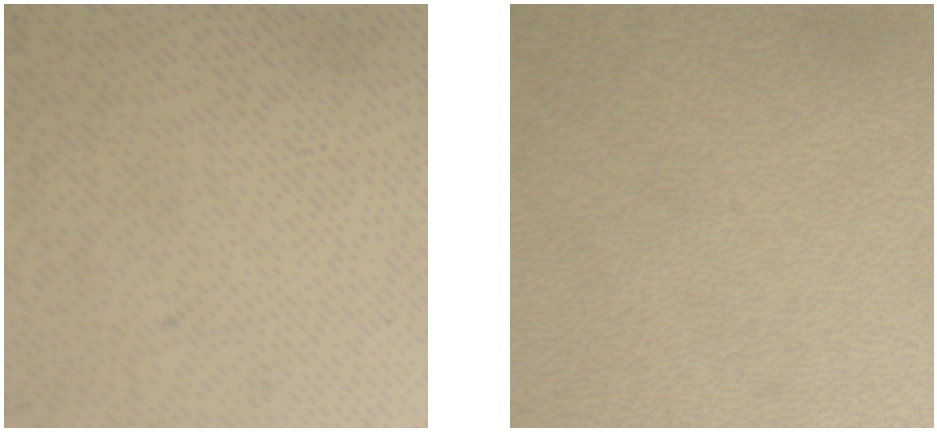

(a) (b)

Figure 3-9: Optical microscope image of (a) CD and (b) DVD. Objective Lens: 40 ×.

(i) AFM and SEM Measurements

Each disc is analyzed by AFM and SEM to get the fine image with better spatial resolution. Figure 3-10 (a) and (b) represent the surface profile of CD and DVD which are measured by AFM with non-contact mode. Since polycarbonate is a soft material, non-contact mode was selected to prevent scratches by the cantilever tip of AFM.

AFM images show the clear surface profiles of both CD and DVD. Depth and

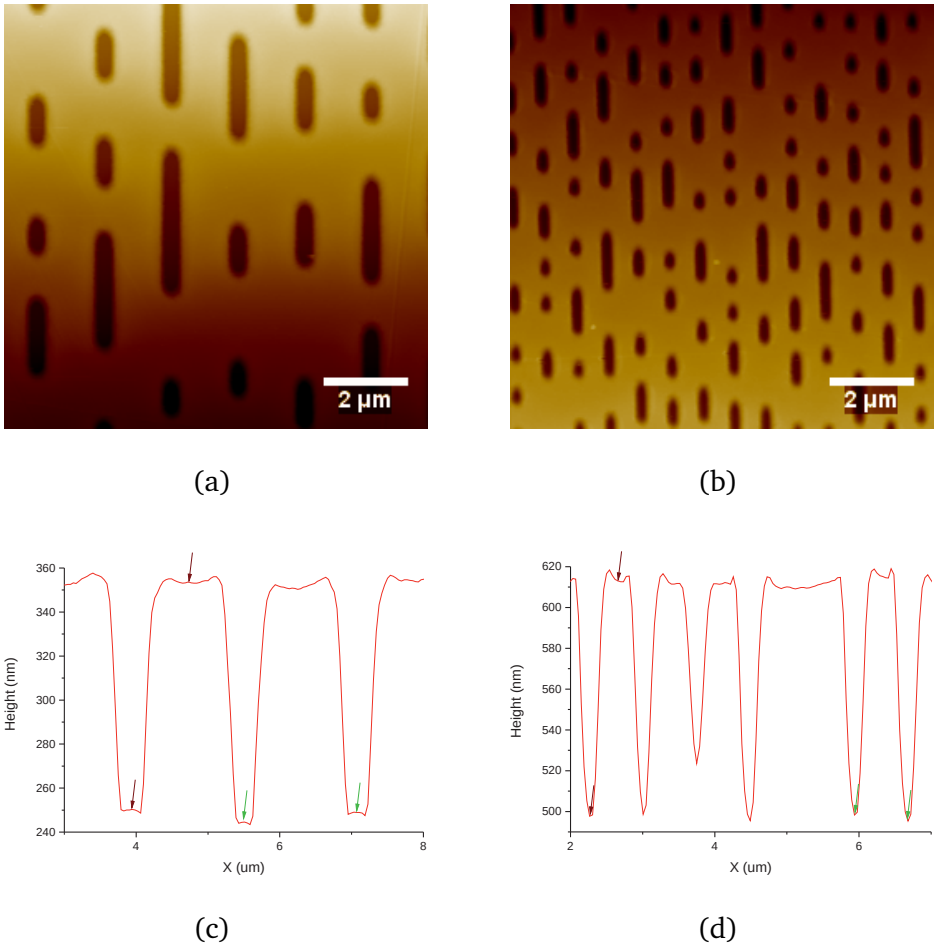


Figure 3-10: AFM image of (a) CD and (b) DVD. And the cross section of (c) CD and (d) DVD. The depth of each pit (height difference between red arrows) are 105.3 nm and 114.9 nm for CD and DVD. And the track pitches (distance between green arrows) are 1600 nm and 760 nm.

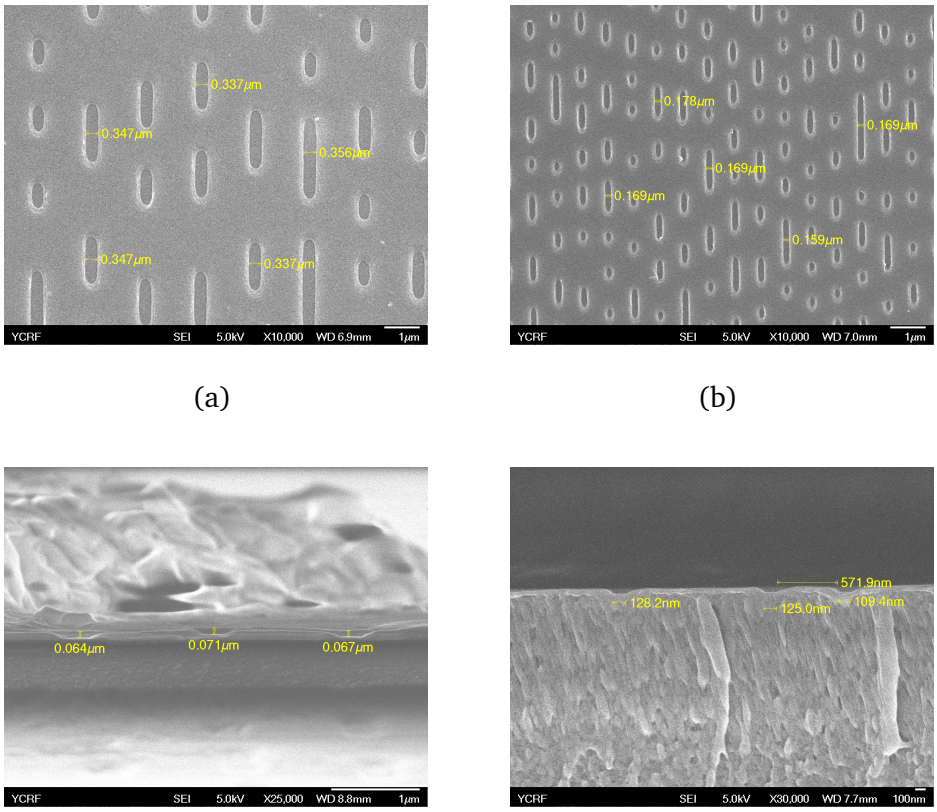


(a) (b)

(c) (d)

Figure 3-11: SEM images of (a) CD and (b) DVD from the top. SEM cross-section images of (c) CD and (d) DVD.

width of the pits can be determined by the cross-section of AFM measurement. The depth of each pits for both discs are around 100 nm. However, the track pitches of CD and DVD are different. From this results, it was confirmed that the optical discs they were manufactured properly upon our request.

Figure 3-11 (a) and (b) show the SEM images of CD and DVD from the top of the samples. Thin metallic layer is coated at the surface of polycarbonate to make the interaction with electrons. The pit width for both discs are shorter than that measured by AFM. Generally, SEM image tends to be enhanced at the edges of structures because of the strong interaction between the electrons from the gun and the edge. Therefore, these shrink of width are expected.

Taking a SEM image in the cross-sectional direction is difficult for optical disc because of the softness of the sample. The softness of optical disc makes hard to cut the medium clearly. Therefore, cutting the optical discs with clear cross-section is not easy. To solve this problem, liquid helium are used to froze the polycarbonate material. After immersing the disc into liquid helium for few seconds, the frozen optical discs are cut by a knife as fast as possible. The direction to cut should be perpendicular to the lines of tracks, i.e., from center to edge of a circular disc. Figure 3-11 (c) and (d) are the cross section of the CD and DVD.

(ii) NSOI Measurements

NSOI measurements are performed for CD and DVD. Figure 3-12 shows the measurement results. Surface topography and the collection mode NSOM images are achieved at the same time. Phase maps are extracted by scanning the same area twice with different conditions.

All three images for each sample have similarities in the general point of view. However, the details are quite different. First of all, the surface topographies re-

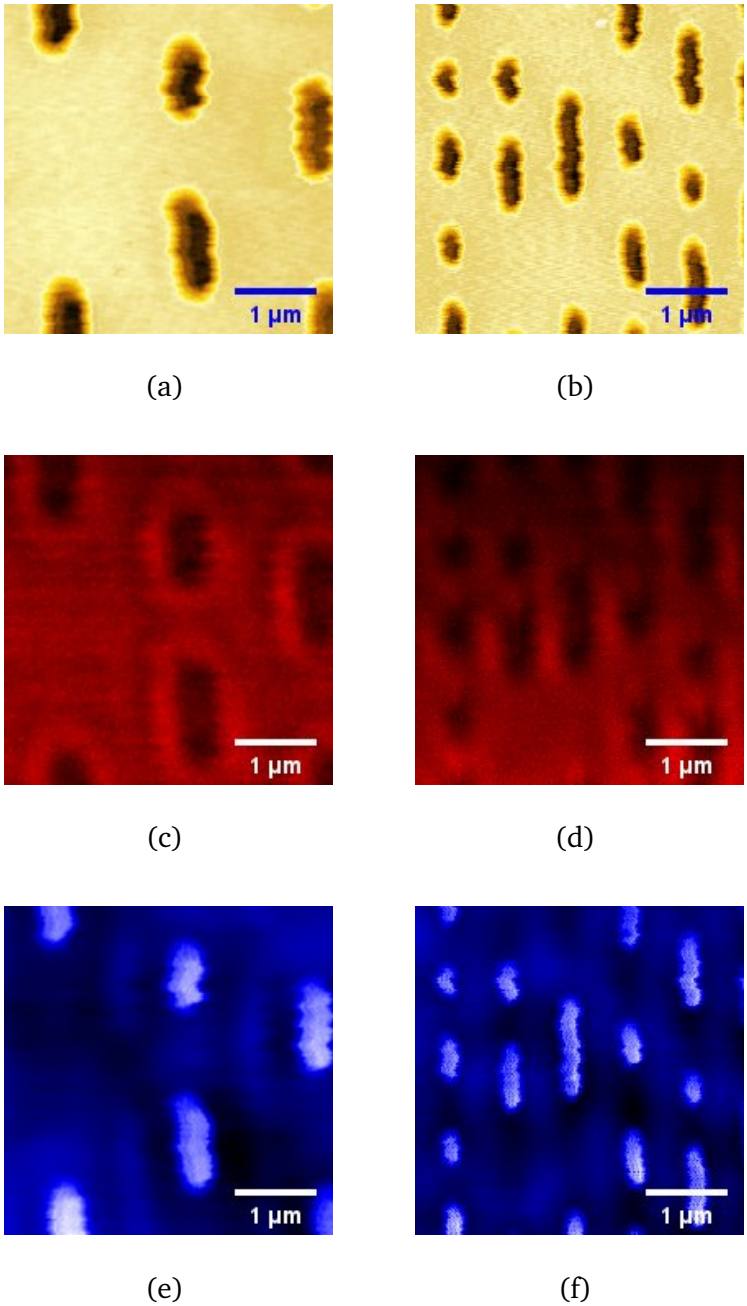


Figure 3-12: NSOI results of CD and DVD. Surface topographies of (a) CD and (b) DVD. Collection mode NSOM images of (c) CD and (d) DVD. Calculated phase maps of (e) CD and (f) DVD.

semble the AFM images in Figure 3-10 because the shear-force detection can also provide the depth profile of samples. NSOM collection images show lower resolution compared to the others. NSOM collection mode basically measures transmission difference between pixels. Since optical discs for this experiments are homogenous in the whole area, the difference of transmission between pits and lands must be similar. The diffraction at the edges of pits clearly observed in these figures. Comparing the CD and DVD cases (Figure 3-12 (c) and (d)), the closer the pits become, the harder the patterns are to be resolved.

On the contrary, the phase maps give much better information compared to NSOM collection images. Even for the DVD sample, the clearly resolved image can be obtained from the phase map of the field (Figure 3-12 (f)). Since the refractive index of polycarbonate at 632.8 nm is 1.580 [Kasarova et al., 2007], one can expected that (OPD) $\sim$ 160 nm in z-direction can be definitely resolved by NSOI.

**(c) Blu-ray Disc**

Unlike the CD and DVD, blu-ray disc has sub-wavelength structure (Table 3.1). Therefore, it is hard to obtain clear optical image by conventional microscope. Figure 3-13 shows the white light optical microscope image by using the same instrument as Figure 3-9. Nothing can be distinguished in this figure, because the track pitch of blu-ray is too small to be resolved.

(i) AFM and SEM measurements

The images taken by AFM and SEM are presented in Figure 3-14. AFM image (Figure 3-14 (a)) is taken by non-contact mode because of the same reason as CD and DVD. The sample for cross-sectional SEM image is prepared by the same process as CD and DVD cases.

Figure 3-13: Optical microscope image of Blu-ray disc. Objective Lens: 40 $\times$.

The depth of the pits of blu-ray disc can be determined by the line profile of AFM image (Figure 3-14 (b)). It is about 60 nm. This value is smaller than that of the other optical discs. This is related to the difficulty of fabrication. But the track pitch is smaller than that of DVD. This feature makes the extremely enhanced capability of blu-ray disc compared to the previous generations of optical discs.

The top view SEM image (Figure 3-14 (c)) shows the edge effect again. The edge of each pit shines brightly like the CD and DVD cases. The outlines of pits are more rough than previous generations. This result indicates the difficulty of fabrication process. Currently, there are no mass-productive blu-ray pressing manufacturer in our country. In Figure 3-14 (d), the lines of tracks are hardly distinguishable. The track pitches are too small and the condition of pits are not perfect, as one can see in Figure 3-14 (b).

One interest thing is the pit width. The pit width of blu-ray is not much different compared to DVD. Commercially known value is about 120 nm but, in this case, about 180 nm. However, the track pitch shows the blu-ray property decidedly. The

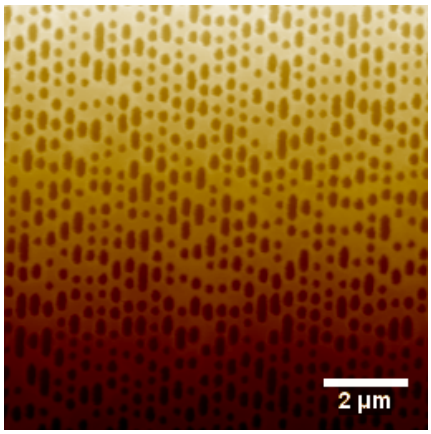


(a)

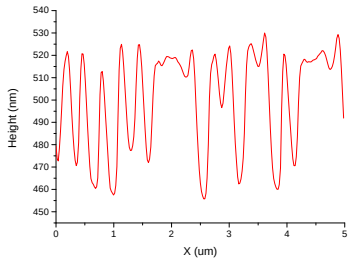


(b)

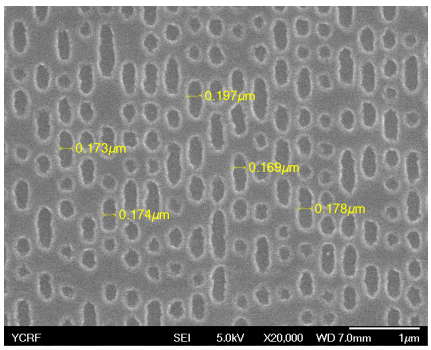


(c)

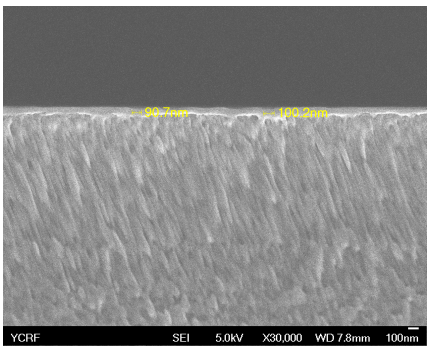


(d)

Figure 3-14: (a) AFM image and (b) the cross section of a blu-ray disc. (c) SEM image (top view) and (d) SEM cross section of a blu-ray disc.

disc is specially prepared by *JMI Co., Ltd.*. The fabrication process technique is not open to the public. This may be the reason why pit widths between the commercial and experimental ones are different.

(ii) NSOI Measurement

Figure 3-15 shows the simultaneously measured results for blu-ray disc. From the image of Figure 3-15 (a), it can be confirmed that the distance regulation system works well because of intaglio printed patterns (which means that the patterns are etched into the surface) with sub-wavelength scale as well as relief printed ones.

Each pattern on the disc can not be resolved by NSOM collection image (Figure 3-15 (b)) because of the homogeneity of material and the sub-wavelength track pitch. One can notice that there exist some variations at the surface, but it can not be resolved clearly in NSOM collection mode.

However, each data pit can be easily distinguished by the phase image. Figure 3-15 (c) shows the enhanced contrast compared to the NSOM collection image. In the CD and DVD cases, the capability of NSOI in vertical direction is confirmed. From blu-ray disc measurement, it is shown that NSOI has nanometric resolution not only for the height but also lateral dimension. Especially, the AFM result tells us that the depth of blu-ray disc is about 60 nm. Therefore, the depth resolution of NSOI is about 95 nm in the view point of OPD.

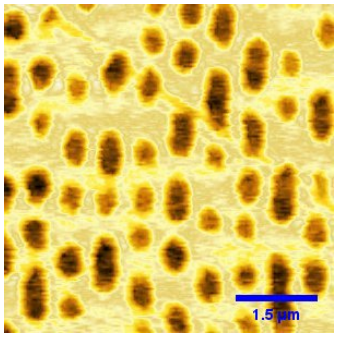


(a)

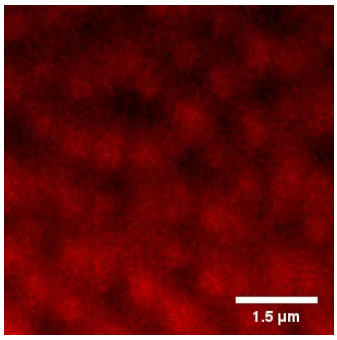


(b)

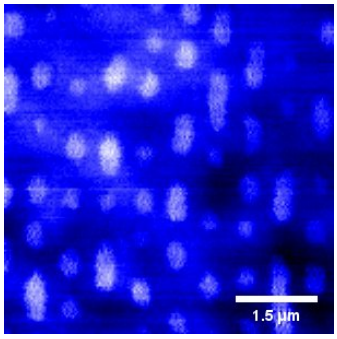


(c)

Figure 3-15: NSOI results of blu-ray disc. (a) Surface topography, (b) collection mode NSOM image and (c) calculated phase map.

## 3.5 Summary

In this chapter, the phase detection method is described and the feasibility of the system is confirmed by measuring the phase of SNG01 and various bare transparent optical discs.

NSOI is constructed by combining the NSOM with the interferometer. The idea of NSOI is based on the interference between the light from the sample surface and the reflection from the NSOM tip-end. The measurements are also performed for the same area without tip approaching. The relative phase can be calculated by these two results. Not only phase variation but also the surface topography and near-field collection signal can be achieved simultaneously.

For SNG01, the vanadium and quartz are well distinguished in the phase measurement. The surface topography can be also achieved by using shear-force detection method. In particular, the background can be successfully removed by the proposed method.

Phase measurement of optical discs provides well-established feasibility of the system. Bare transparent discs are provided by *JMI Co., Ltd.*. They are specially prepared in the middle of fabrication process. The phase informations of all the three generations of optical discs (CD, DVD and blu-ray disc) are obtained by the NSOI. Surface topography and the collection mode NSOM image can be acquired simultaneously. The phase map for each disc is obtained by the phase extraction method. Especially, blu-ray disc has the sub-wavelength structures. From the results, OPD of 95 nm resolution in depth and sub-wavelength in lateral resolution are successfully achieved for this new phase measurement concept.

# Chapter 4

# Near-field Investigation of 2-Dimensional Nanomaterials

## 4.1 Introduction

Carbon (C) is the chemical element which has atomic number Z = 6. There are several allotropes of carbon. Their properties are distinguishable according to their structures. The well-known carbon allotropes are graphite, diamond, and amorphous carbon. Especially, graphite has the structure of multiple stack of honeycomb lattice.

In 2004, Andre Geim's group in *University of Manchester* fabricated the first monolayer carbon honeycomb lattice by using scotch tape [Novoselov et al., 2004]. Until then, it was presumed that two dimensional materials can not exist because of thermodynamical issues [Geim and Novoselov, 2007]. At that time, only curved structured like fullerenes ($C_{60}$) [Kroto et al., 1985] or carbon nanotubes (CNT) [Iijima, 1991] had been discovered or fabricated. After 1 year later, Philip Kim group in *Columbia University* observed half-integer quantum-Hall effect in graphene exper-

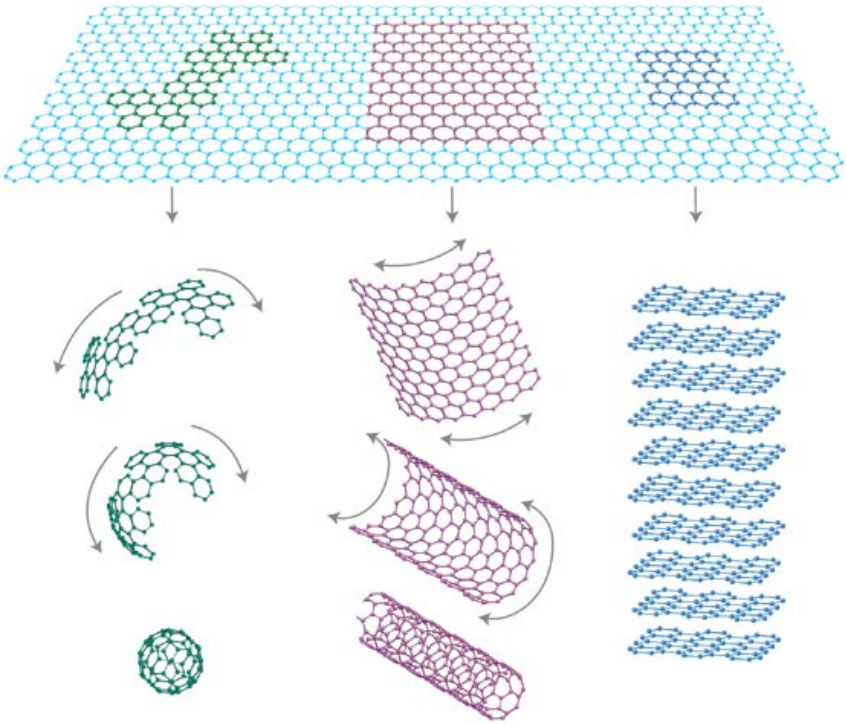

Figure 4-1: “Mother of all graphitic forms” [Geim and Novoselov, 2007].

imentally [Zhang et al., 2005]. After then, graphene became one of the most attractive materials to study in solid state physics. Researches on low-dimensional materials were explosively increased after this publication. For instance, Andre Geim and Konstantin Novoselov, who are the main authors of the 2004 paper, received Nobel prize in physics in 2010.

Graphene has two-dimensional (2D) honeycomb lattice structure with carbon atoms and the basic form of other graphitic materials (eg. fullerenes, CNTs, graphite etc.. Figure 4-1). Fullerenes have the carbon structure in the form of a hollow shpere, ellipsoid, tube, etc.. Especially, the most common fullerene structure is a zero dimensional sphere-like structure with 60 carbon atoms being rolled like a soccer ball. When the graphene sheet bonds in cylindrical shape, it is called CNT. CNTs were first discovered by Iijima in 1991 [Iijima, 1991]. They can be categorized by the number of walls, for example, single-wall (SWNT) or multiwall (MWNT) [Volder

et al., 2013]. The graphite is multiple stack of graphenes.

Since 2004, graphene receives much attention because of their extremely high electron mobility [Bolotin et al., 2008; Morozov et al., 2008], high Young's modulus [Lee et al., 2008], and thermal conductivity [Balandin et al., 2008]. Optical properties of graphene have also been researched widely [Mak et al., 2012, 2008; Nair et al., 2008; Stauber et al., 2008; Thongrattanasiri et al., 2012]. In recent years, graphene plasmon is one of the most actively studying topics [Bostwick et al., 2010; Chen et al., 2012; Fei et al., 2012, 2013; Polini et al., 2008].

Graphene shows semi-metallic properties because of its band-gapless structure. Therefore, there is an obstacle to make graphenes transistor devices. To overcome this obstacle, a lot of researches have been performed on another kind of 2-dimensional materials, such as insulating BN [Dean et al., 2010], $MoS_2$ [Castellanos-Gomez et al., 2010; Lee et al., 2010; Mak et al., 2010; Malard et al., 2013; Molina-Sánchez and Wirtz, 2011; Radisavljevic et al., 2011; Ramakrishna Matte et al., 2010; Splendiani et al., 2010; Tonndorf et al., 2013; Yim et al., 2014; Yin et al., 2014; Zeng et al., 2012], $NbSe_2$ [Castellanos-Gomez et al., 2010], $MoSe_2$ [Larentis et al., 2012; Tonndorf et al., 2013], $WS_2$ [Molina-Sánchez and Wirtz, 2011; Ramakrishna Matte et al., 2010], $WSe_2$ [Tonndorf et al., 2013], borophene [Piazza et al., 2014], phosphorene [Li and Appelbaum, 2014; Liu et al., 2014], etc.. Especially, $MoS_2$, $NbSe_2$, $MoSe_2$, $WS_2$, and $WSe_2$ belong to the family of transition metal dichalcogenides with the common formula of $MX_2$, where M represents the transition metal (M=Mo, W, Nb, Ta, Ti) and X means chalcogen (X=Se, S, Te). The electrical properties of such materials can be changed from semi-conducting to super-conducting depending on the composition of metal and chalcogen [Benameur et al., 2011]. In 2010, the *UC Berkeley* group and *Columbia* group independently published papers about the band-structure of molybdenum disulfide ($MoS_2$) due to the number of layers. They demonstrated that a monolayer $MoS_2$ has 1.9 eV direct band-gap [Mak et al.,

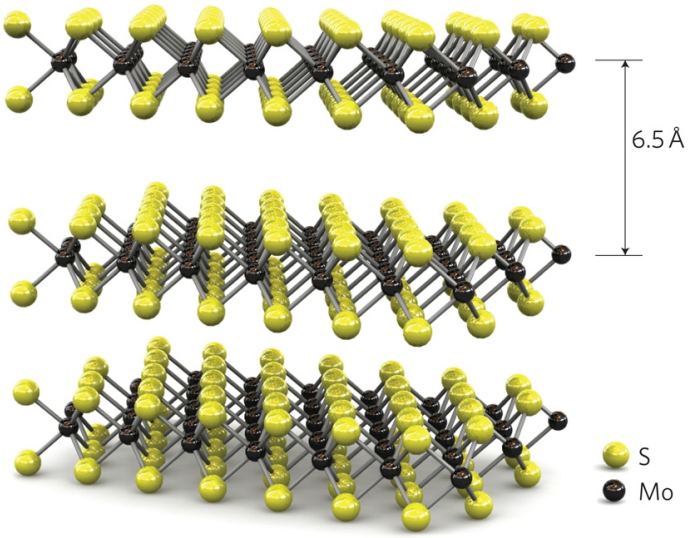


Figure 4-2: Three-dimensional representation of the atomic structure of $MoS_2$ [Radisavljevic et al., 2011].

2010; Splendiani et al., 2010]. These results predict that monolayers $MoS_2$ can be applied for the development of advanced transistor and photoelectric devices.

## 4.2 Electronic State of Graphene: Tight-Binding Model

Figure 4-3 (a) shows the honeycomb lattice of graphene structure. It has a triangular Bravais lattice with lattice vectors,

$$\boldsymbol{a}_1 = \frac{a}{2}\left(3, \sqrt{3}\right) \qquad \boldsymbol{a}_2 = \frac{a}{2}\left(3, -\sqrt{3}\right) \tag{4.1}$$

where $a \approx 1.42$ Å is the nearest-neighbour distance. The nearest-neighbour vectors are

$$\boldsymbol{\delta}_1 = \frac{a}{2}\left(1, \sqrt{3}\right) \qquad \boldsymbol{\delta}_2 = \frac{a}{2}\left(1, -\sqrt{3}\right) \qquad \boldsymbol{\delta}_3 = \frac{a}{2}\left(-1, 0\right) \tag{4.2}$$

which are belong to the different sublattice with the atom. Figure 4-3 (b) shows the reciprocal lattice of a honeycomb lattice. It is also triangular structure. The lattice vectors are

$$\boldsymbol{b}_1 = \frac{2\pi}{3a}\left(1, \sqrt{3}\right) \qquad \boldsymbol{b}_2 = \frac{2\pi}{3a}\left(1, -\sqrt{3}\right) \tag{4.3}$$

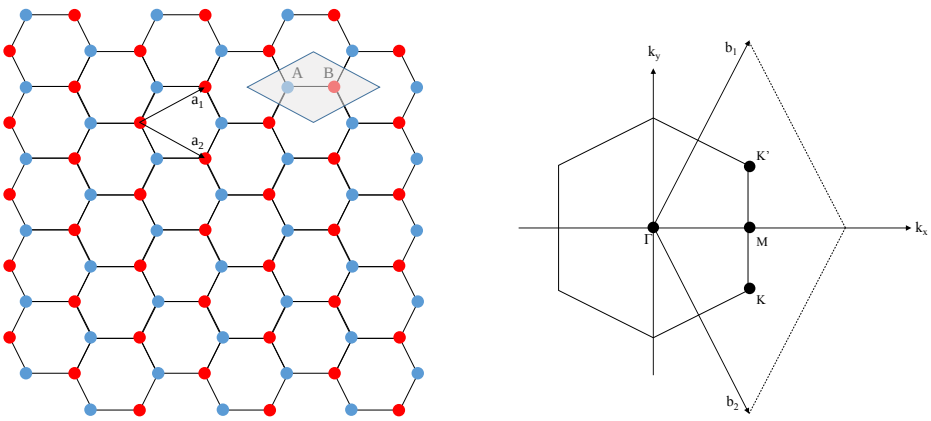


(a) (b)

Figure 4-3: (a) A graphene lattice. The sublattices are distinguished by red and blue dots. (b) Reciprocal lattice.

In addition, the specific symmetry points are (Figure 4-3 (b)),

$$K' = \left(\frac{2\pi}{3a}, \frac{2\pi}{3\sqrt{3}a}\right), \qquad K = \left(\frac{2\pi}{3a}, -\frac{2\pi}{3\sqrt{3}a}\right), \qquad \text{and} \qquad M = \left(\frac{2\pi}{3a}, 0\right) \tag{4.4}$$

Carbon atom has 2 core electrons and four valence electrons. Therefore, the valence electrons occupy $2s, 2p_x, 2p_y$ and $2p_z$ orbitals. Carbon atoms in graphene are densely packed in plane with sp$^2$ hybridization ($\sigma$ states). $p_z$ orbital makes $\pi$ state. The electronic state near Fermi level in graphene can be well described by considering $\pi$ orbitals only. The electronic band structure can be calculated by using tight-binding model [Wallace, 1947]. The detailed explanations are well described in a lot of textbooks [Katsnelson, 2012; McCann, 2012].

In general, the tight-binding model for a system which have $n$ atoms per unit cell, the Bloch functions $\Phi_j(\mathbf{k}, \mathbf{r})$ are given by

$$\Phi_j(\mathbf{k}, \mathbf{r}) = \frac{1}{\sqrt{N}} \sum_{i=1}^{N} e^{i\mathbf{k}\cdot\mathbf{R}_{ji}} \phi_j\left(\mathbf{r} - \mathbf{R}_{ji}\right) \tag{4.5}$$

where $\phi_j$ is the atomic orbital and $j = 1 \ldots n$. The summation is over $N$ different unit cells labeled by $i = 1 \ldots N$ and $\mathbf{R}_{ji}$ denotes the position of $j$th orbital in $i$th unit cell. The electronic wave function $\Psi_j(\mathbf{k}, \mathbf{r})$ is described by a linear superposition of $n$ Bloch functions,

$$\Psi_j(\mathbf{k}, \mathbf{r}) = \sum_{l=1}^{n} c_{jl}(\mathbf{k}) \Phi_l(\mathbf{k}, \mathbf{r}) \tag{4.6}$$

When the Hamiltonian is given by $\mathbb{H}$, the energy of the $j$th band is given by

$$E_j(\mathbf{k}) = \frac{\langle \Psi_j | \mathbb{H} | \Psi_j \rangle}{\langle \Psi_j | \Psi_j \rangle} = \frac{\sum_{i,l}^{n} c_{ji}^* c_{jl} \langle \Phi_i | \mathbb{H} | \Phi_l \rangle}{\sum_{i,l}^{n} c_{ji}^* c_{jl} \langle \Phi_i | \Phi_l \rangle} = \frac{\sum_{i,l}^{n} H_{il} c_{ji}^* c_{jl}}{\sum_{i,l}^{n} S_{il} c_{ji}^* c_{jl}} \tag{4.7}$$

where $H_{il} = \langle \Phi_i | \mathbb{H} | \Phi_l \rangle$ and $S_{il} = \langle \Phi_i | \Phi_l \rangle$. If the differentiation of $E_j$ by specific coefficient $c_{jm}^*$ is zero ($\partial E_j / \partial c_{jm}^* = 0$), the energy $E_j$ can be minimized. From this

calculation,

$$\sum_{i=1}^{n} H_{ml} c_{jl} = E_j \sum_{i=1}^{n} S_{ml} c_{jl} \tag{4.8}$$

or

$$H\Psi_j = E_j S \Psi_j \tag{4.9}$$

is obtained. Therefore, the energy can be calculated by solving

$$det(H - E_j S) = 0 \tag{4.10}$$

Since the graphene has two atoms per unit cell, the case of $n = 2$ should be considered. Graphene $\pi$ state has the unit cell like the grey part in Figure 4-3 (a). Let's assume that the atoms in unit cell are denoted by A and B. For this case,

$$\begin{pmatrix} H_{AA} & H_{AB} \\ H_{BA} & H_{BB} \end{pmatrix} \begin{pmatrix} c_{jA} \\ c_{jB} \end{pmatrix} = E_j \begin{pmatrix} S_{AA} & S_{AB} \\ S_{BA} & S_{BB} \end{pmatrix} \begin{pmatrix} c_{jA} \\ c_{jB} \end{pmatrix} \tag{4.11}$$

Now, let's think about the components of $H$.

$$H_{AA} = \frac{1}{N} \sum_{i=1}^{N} \sum_{j=1}^{N} e^{i\mathbf{k}\cdot(\mathbf{R}_{Aj} - \mathbf{R}_{Ai})} \langle \phi_A(\mathbf{r} - \mathbf{R}_{Ai}) | \mathbb{H} | \phi_A(\mathbf{r} - \mathbf{R}_{Aj}) \rangle \tag{4.12}$$

where $\mathbf{k}$ is the wave vector in the graphene plane. Assuming that $i = j$ contributes dominantly, $H_{AA}$ is approximately,

$$H_{AA} \approx \epsilon_{2p_z} \tag{4.13}$$

where $\epsilon_{2p_z} = \langle \phi_A(\mathbf{r} - \mathbf{R}_{Ai}) | \mathbb{H} | \phi_A(\mathbf{r} - \mathbf{R}_{Ai}) \rangle$ is the energy of $2p_z$ orbital. The same process can be utilized for $H_{BB}$, i.e.,

$$H_{AA} = H_{BB} \approx \epsilon_{2p_z} \tag{4.14}$$

$$S_{AA} = S_{BB} = 1 \tag{4.15}$$

can be easily calculated by the same approximation.

One of the off-diagonal component of $H$ is

$$H_{AB} = \frac{1}{N}\sum_{i=1}^{N}\sum_{j=1}^{N} e^{i\mathbf{k}\cdot(\mathbf{R}_{Bj}-\mathbf{R}_{Ai})}\langle\phi_A(\mathbf{r}-\mathbf{R}_{Ai})|\mathbb{H}|\phi_B(\mathbf{r}-\mathbf{R}_{Bj})\rangle \tag{4.16}$$

For this case, there are three nearest-neighbor B atoms for an A atom. Therefore,

$$H_{AB} \approx \frac{1}{N}\sum_{i=1}^{N}\sum_{j=1}^{3} e^{i\mathbf{k}\cdot(\mathbf{R}_{Bj}-\mathbf{R}_{Ai})}\langle\phi_A(\mathbf{r}-\mathbf{R}_{Ai})|\mathbb{H}|\phi_B(\mathbf{r}-\mathbf{R}_{Bj})\rangle \tag{4.17}$$

Let $t = \langle\phi_A(\mathbf{r}-\mathbf{R}_{Ai})|\mathbb{H}|\phi_B(\mathbf{r}-\mathbf{R}_{Bj})\rangle$ is the hopping energy between A and B atoms. Then,

$$\begin{aligned} H_{AB} &\approx \frac{t}{N}\sum_{i=1}^{N}\sum_{j=1}^{3} e^{i\mathbf{k}\cdot(\mathbf{R}_{Bj}-\mathbf{R}_{Ai})} \\ &= \frac{t}{N}\sum_{i=1}^{N}\sum_{j=1}^{3} e^{i\mathbf{k}\cdot\boldsymbol{\delta}_j} \\ &= t\sum_{j=1}^{3} e^{i\mathbf{k}\cdot\boldsymbol{\delta}_j} = tf(\mathbf{k}) \end{aligned} \tag{4.18}$$

Since $\boldsymbol{\delta}_j$ are the nearest-neighbor vectors in equation (4.2),

$$\begin{aligned} f(\mathbf{k}) &= \sum_{j=1}^{3} e^{i\mathbf{k}\cdot\boldsymbol{\delta}_j} \\ &= 2\exp\left(\frac{iak_x}{2}\right)\cos\left(\frac{\sqrt{3}ak_y}{2}\right) + \exp\left(-iak_x\right) \end{aligned} \tag{4.19}$$

And

$$H_{BA} = tf^*(\mathbf{k}) \tag{4.20}$$

$S_{AB}$ and $S_{BA}$ can be obtained by similar calculation, i.e.,

$$S_{AB} = s_0 f(\mathbf{k}) \qquad S_{BA} = s_0 f^*(\mathbf{k}) \tag{4.21}$$

where $s_0 = \langle \phi_A(\mathbf{r} - \mathbf{R}_{Ai}) | \phi_B(\mathbf{r} - \mathbf{R}_{Bj}) \rangle$. Then we can obtain,

$$H = \begin{pmatrix} \epsilon_{2p_z} & tf(\mathbf{k}) \\ tf^*(\mathbf{k}) & \epsilon_{2p_z} \end{pmatrix} \qquad S = \begin{pmatrix} 1 & s_0 f(\mathbf{k}) \\ s_0 f^*(\mathbf{k}) & 1 \end{pmatrix} \tag{4.22}$$

By substituting this result to equation (4.10), the band structure of graphene can be calculated.

$$E_{\pm} = \frac{\epsilon_{2p_z} \pm t|f(\mathbf{k})|}{1 \pm s_0 |f(\mathbf{k})|} \tag{4.23}$$

$$|f(\mathbf{k})| = \left[ 4\cos^2\left(\frac{\sqrt{3}ak_y}{2}\right) + 4\cos\left(\frac{3ak_x}{2}\right)\cos\left(\frac{\sqrt{3}ak_y}{2}\right) + 1 \right]^{1/2} \tag{4.24}$$

Figure 4-4 shows the low-energy band structure of graphene. The conduction and valence bands meet at the corners of the Brillouin zone (K points). Dispersion of band near these point is linear. It has conical shape and the electrons act like Dirac massless fermions.

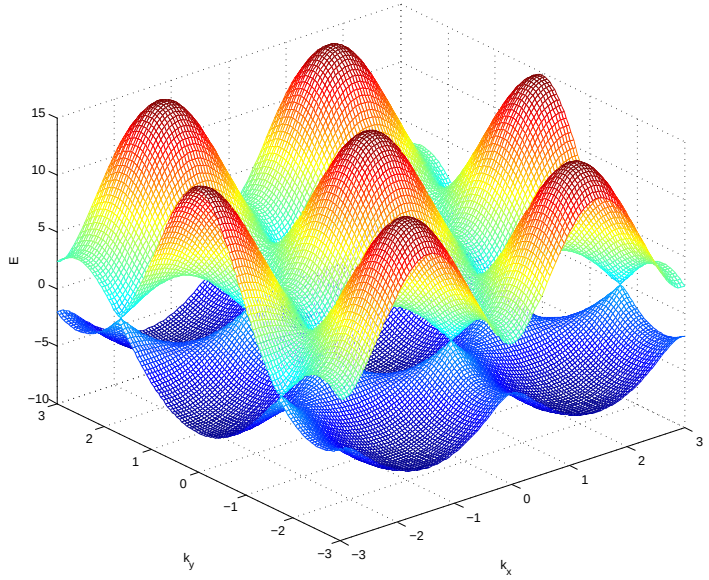


(a)

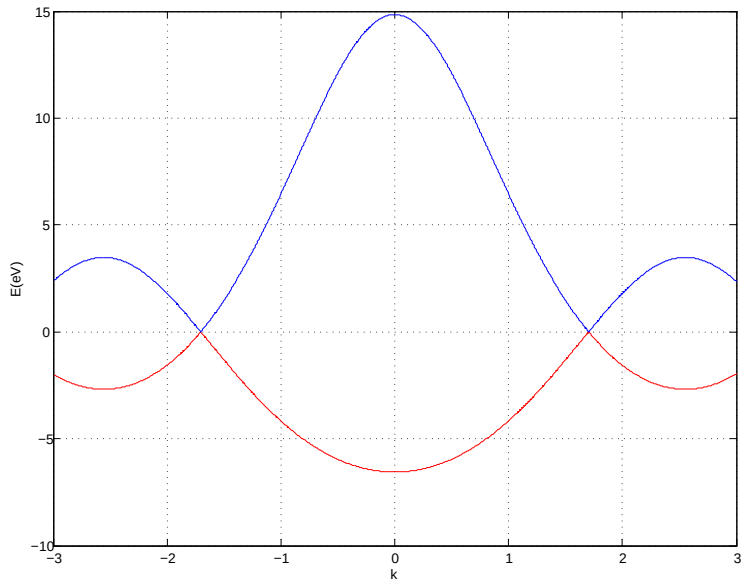


(b)

Figure 4-4: (a) Band structure of graphene. (b) Cross-section of (a) in direction from Γ to K point. Nearest-neighbor hopping with parameter $t = 3.033$ eV, nearest-neighbor overlap parameter $s_0 = 0.129$ and orbital energy $\epsilon_{2p_z} = 0$.

## 4.3 Phase Measurement for 2-dimensional Nanomaterials

### 4.3.1 Graphene

#### (a) Sample Preparation: Fully- and Partially- Grown Graphene

There are several methods to make graphene; mechanical exfoliation [Novoselov et al., 2004; Zhang et al., 2005], chemical exfoliation [Eda et al., 2008; Li et al., 2008], chemical vapor deposition (CVD) method [Kim et al., 2009; Li et al., 2009] and epitaxy method [Sutter et al., 2008; Vázquez de Parga et al., 2008]. Mechanical exfoliation method can make the best high quality graphene but it is difficult to make large scales or specific shapes. On the contrary, CVD method can fabricate scalable sheet and control the number of layers, still with high quality [Bae et al., 2010; Li et al., 2009].

The graphene samples in this thesis are prepared by CVD. A mixture of $CH_4$ and $H_2$ gases is flown onto the dried copper (Cu) foil strip during CVD process. The detailed process can be found in previously published paper [Havener et al., 2012]. Partially grown graphenes with hexagonal shape are fabricated at the upstream of the flow. The grains become a continuous graphene layer as the distance from the upstream edge increases. Grown graphene samples are transferred to quartz substrate as follows [Bae et al., 2010; Li et al., 2009]. ; 1) PMMA is spin-coated on graphene-grown Cu foil. 2) Cu foil is removed by ammonium persulfate solution. 3) The remaining part (PMMA-graphene) is transferred to quartz substrate. 4) The PMMA layer is removed by acetone. Figure 4-5 shows the schematic of transfer process of graphene from Cu foil to quartz substrate.

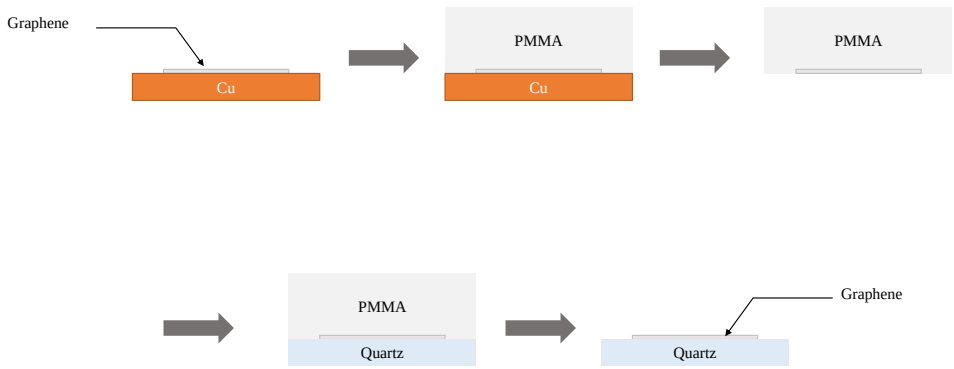


Figure 4-5: Graphene transfer process

### (b) Near-field Measurement

Although graphene has atomic-scale thickness, it can be observed by the optical microscope when it is attached to silicon substrate covered by $SiO_2$ [Blake et al., 2007]. Moreover, it is reported that graphene absorbs $\pi\alpha \approx 2.3\%$ of illuminated white light where $\alpha = e^2/\hbar c \approx 1/137$ is fine structure constant [Nair et al., 2008]. Therefore, optical properties of graphene became an important topic to study. In this section, near-field transmission properties and phase measurements of graphenes are performed by using the NSOI.

#### (i) Fully-Grown Graphene

Figure 4-6 shows the result of fully-grown graphene by using the instrument. Since the PMMA cannot be removed completely, the graphene is covered by PMMA. The surface topography (Figure 4-6 (a)) shows nothing specific except dusts. However, dark lines can be found in Figure 4-6 (b) and (c).

Fabricating large graphene sheet with CVD has an issue on grain boundary. Since grain boundary can alter the electronic transport properties of graphene [Yazyev and Louie, 2010; Yu et al., 2011], a lot of researches are focused on how to visualize it. TEM [Huang et al., 2011; Kim et al., 2011] and STM [Gao et al., 2010; Rasool

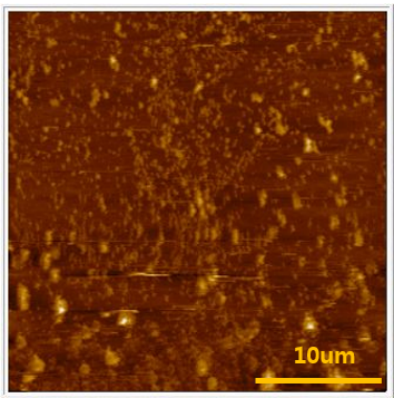


(a)

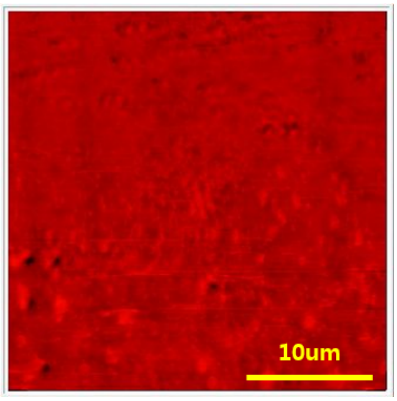


(b)

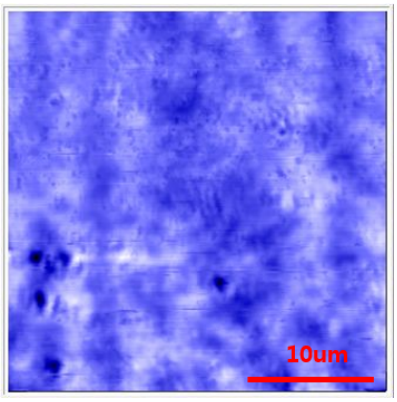


(c)

Figure 4-6: Measured results for fully grown graphene. (a) Surface topography, (b) NSOM collection signals and (c) phase variation.

et al., 2011; Tian et al., 2011; Yu et al., 2011] can directly visualize grain boundary in atomic scale. However, they can see only the boundary but not the whole picture. Duong et al. figured out grain boundray with optical microscope by selectively oxidizing the Cu foil under the graphene sheet [Duong et al., 2012]. NSOM can be also a promising technique to find out the grain boundary [Fei et al., 2013].

The lines which can be found in Figure 4-6 (b) and (c) look like grain boundaries of fully-grown graphene. In previous research, ANSOM can detect grain boundary by using plasmonic effect originated from the interaction between metallic tip and the electrons in graphene [Fei et al., 2013]. They used far infrared (IR) (about 10 μm) wave. In this study, the similar effects are observed by using visible range ($\lambda$ = 632.8 nm) electromagnetic wave.

(ii) Partially-Grown Graphene

Partially-grown graphene shows hexagonal shape feature. Figure 4-7 shows the NSOI measurement result for the sample. Since partially-grown graphene has island structure, the graphene can be distinguished from the quartz substrate. The height of graphene (Figure 4-7 (a)) can be hardly distinct the existence of graphene. However, NSOM and phase measurement show clear images of graphene itself.

In the image of collection mode NSOM, the collected near-field signal of graphene is lower than that of PMMA layer only. Even though graphene layer has atomic scale, the image shows clearly the existence of layer. Previously published research shows the absorption of graphene itself is 2.3 % [Nair et al., 2008]. However, the collection mode NSOM result shows different feature. In other words, the intensity of light decreases about 13.5 % compared to the other part of the sample. Since the near-field characteristic is related to not only the absorption of the material but also other physical phenomena, the result on the absorption can be different. First of all, if the

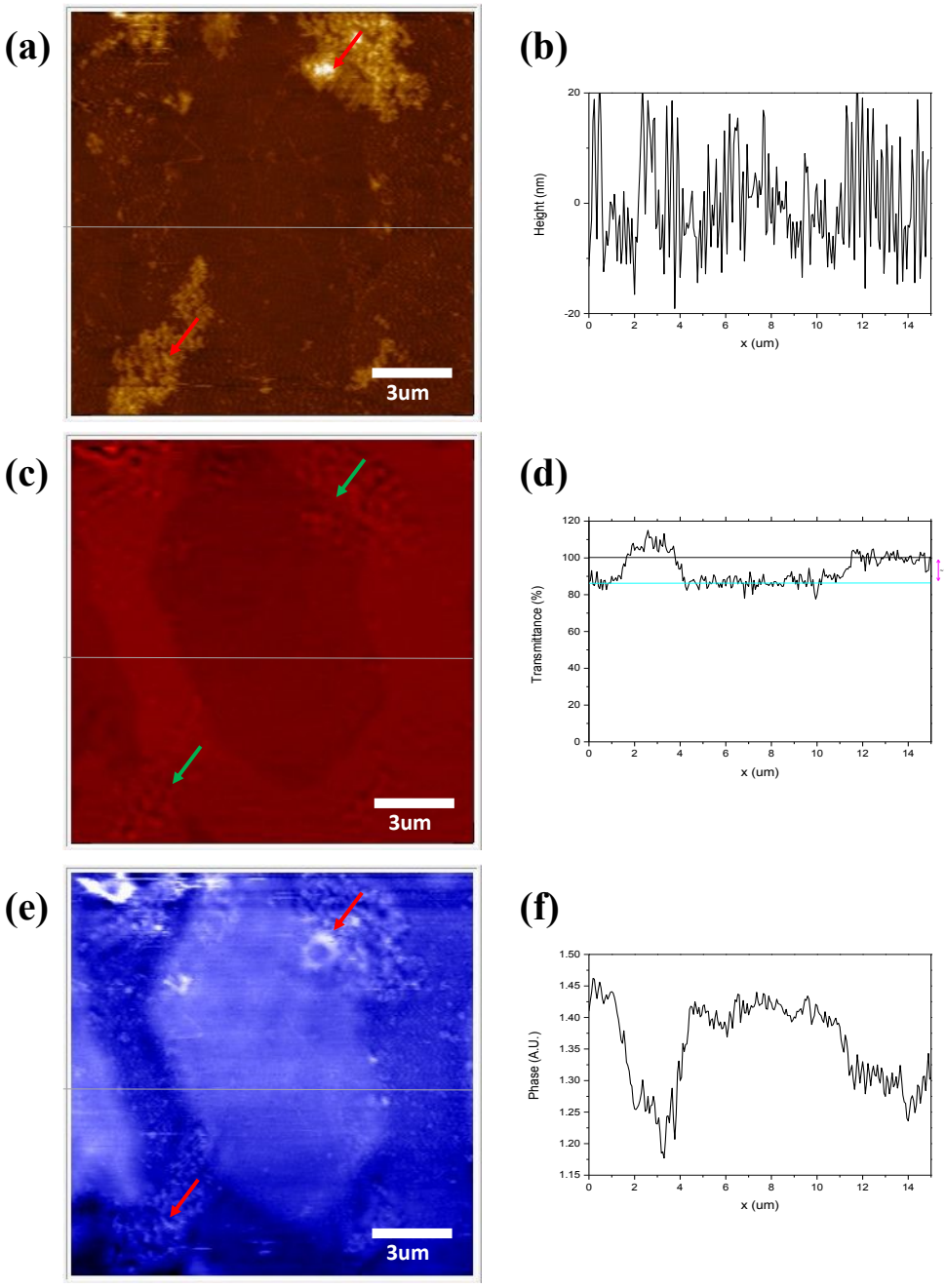


Figure 4-7: Measured results for partially-grown graphene. (a) Surface topography and (b) the cross-sectional view, (c) NSOM collection signals and (d) the cross-sectional view, (e) phase variation and (f) the cross-sectional view.

gap between sample and probe tip make destructive interference, the fiber-collected intensity can be reduced. In addtion, the intensity can be affected by the the transfer process which can make unwanted space between graphene and substrate. Another possibility is the plasmon absorption originated from the tip and the electrons in graphene. The details need to be studied more precisely in the future.

The phase map (Figure 4-7 (e)) has tendency similar to the NSOM image. The phase is more sensitively related to the surface topography, comparing to NSOM image. The covered PMMA layer makes the surface more rough, as also observed in the phase measurement, which is indicated as arrows in the Figures. The height variations do not make clear change in NSOM image but it changes the phase distinctively. The ripples are also observed on the right-up side of graphene's hexagonal shape. This may be considered as the internal stress in the sample during the transfer process.

(iii) Graphite Oxide

A few of the partially grown graphene starts to change the properties few months later from the day they were fabricated. When the sample is immersed into acetone for a few hours, its microscope image shows interesting features. Figure 4-8 displays the images with reflection and transmission type microscopy. Two graphite oxide flakes are partially overlapped. A single flake shows shiny reflection and dark transmission like noble metal. In addition, the interesting phenomena is observed in the overlapped region. The transmission in stacked flakes increases compared to that in single flake. In general cases, the transmission cannot be increased because of the absorption.

The sample is also investigated by NSOM and NSOI. Figure 4-9 shows the results. The flake can be distinguished by the distance regulation system (Figure 4-9

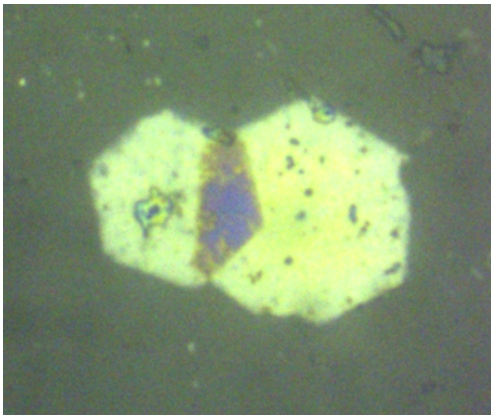

(a)

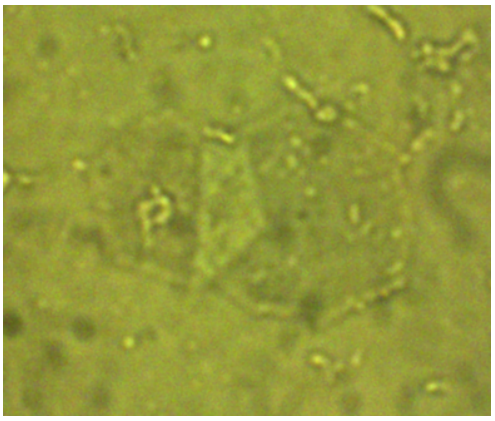

(b)

Figure 4-8: Image of graphite oxide with (a) reflection and (b) transmission type microscopy.

(a)) unlike the result of previous section. Therefore, it can not be considered as a graphene monolayer. Although the sample is covered by unwanted small dusts, the flake is clearly distinguishable.

In Figure 4-9 (b), high throughput is observed in the overlapping area of two flakes. This image shows the high transmission of stacking of the graphite oxide flakes more clearly compared to the microscopy image. This is an abnormal situation but the origin is not revealed yet. We can only guess that the band-gap of

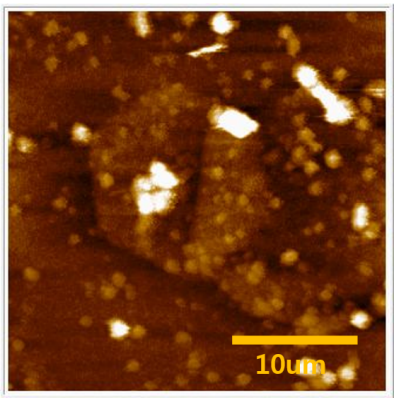


(a)

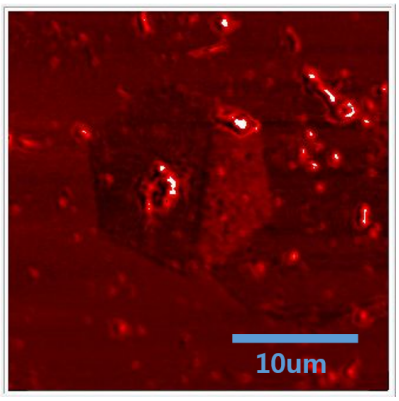


(b)

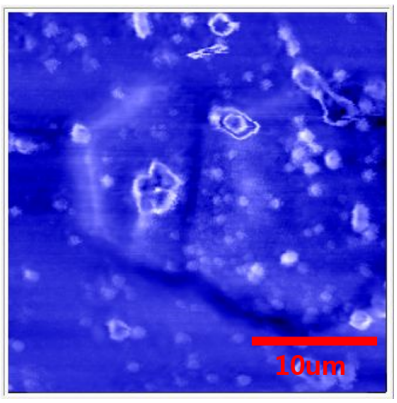


(c)

Figure 4-9: Measured results for graphite oxide. (a) Surface topography, (b) NSOM collection signals and (c) phase variation.

the graphite oxide is changed when there are multiple stacks. In Figure 4-9 (c), the phase variation also can clearly distinguish the flake. Especially, the definite boundary is observed in the left side of the overlapped region. It can be noticed that the right flake covers the left one.

### 4.3.2 Molybdenum Disulfide

$MoS_2$ is one of transition-metal dichalcogenide semiconductor. Monolayer $MoS_2$ has 0.6 nm in thickness [Splendiani et al., 2010; Wieting and Verble, 1971] and 1.9 eV direct band-gap at K-point [Mak et al., 2010; Splendiani et al., 2010]. For this reason, $MoS_2$ is expected to be applied for 2D semiconductor devices.

The sample is prepared by CVD method [Wang et al., 2012]. Sapphire is chosen to be the transparent substrate. The prepared $MoS_2$ shows triangular shape. Figure 4-10 shows the NSOI measurement results for $MoS_2$ in 3-dimensional view.

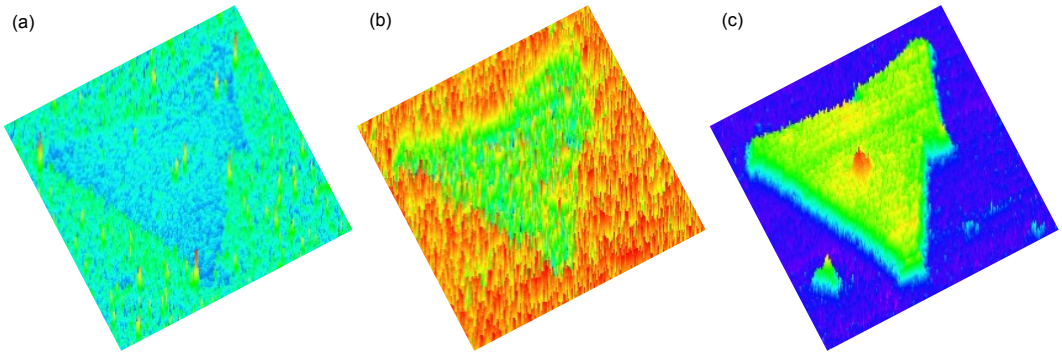


Figure 4-10: 3D view of (a) surface topography, (b) NSOM collection signals and (c) phase variation of $MoS_2$.

In this case, monolayer $MoS_2$ can be distinguished by surface topography (Figure 4-10 (a)) in the noise-level. The height of $MoS_2$ itself is almost the same as the height of the sapphire region. However, the amplitude of tuning fork is maintained more stable. This means that the interaction between the fiber probe tip and $MoS_2$ is stable while scanning and that CVD-grown $MoS_2$ has almost uniform structure.

The contact-mode AFM can measure the atomic thickness of 2-dimensional material [Benameur et al., 2011]. Although shear-force scheme a has lower sensitivity compared to AFM, it can resolve the existence of monolayer $MoS_2$. NSOM collection signal (Figure 4-10 (b)) can also identify $MoS_2$ exactly. The most impressive result is phase image (Figure 4-10 (c)). $MoS_2$ layer can be observed in phase map with high contrast. Especially, the seed only can be clearly defined in phase map.

Figure 4-11 shows this fact more clearly. The seed to make $MoS_2$ sheet is not resolved in surface topography. NSOM signal can clearly shows the seed (blue spot at the center of the triangular sheet in Figure 4-11 (b)), while it is almost impossible to see the seed in the Figure 4-10 (b). However, the phase image can show the existence of the seed with definite red spot at the center of the triangular monolayer $MoS_2$. The cross-sectional view of phase shows definitely the existence of monolayer $MoS_2$ and the seed more. Moreover, small $MoS_2$ flakes can only be seen in at the bottom-right of Figure 4-11 (c).

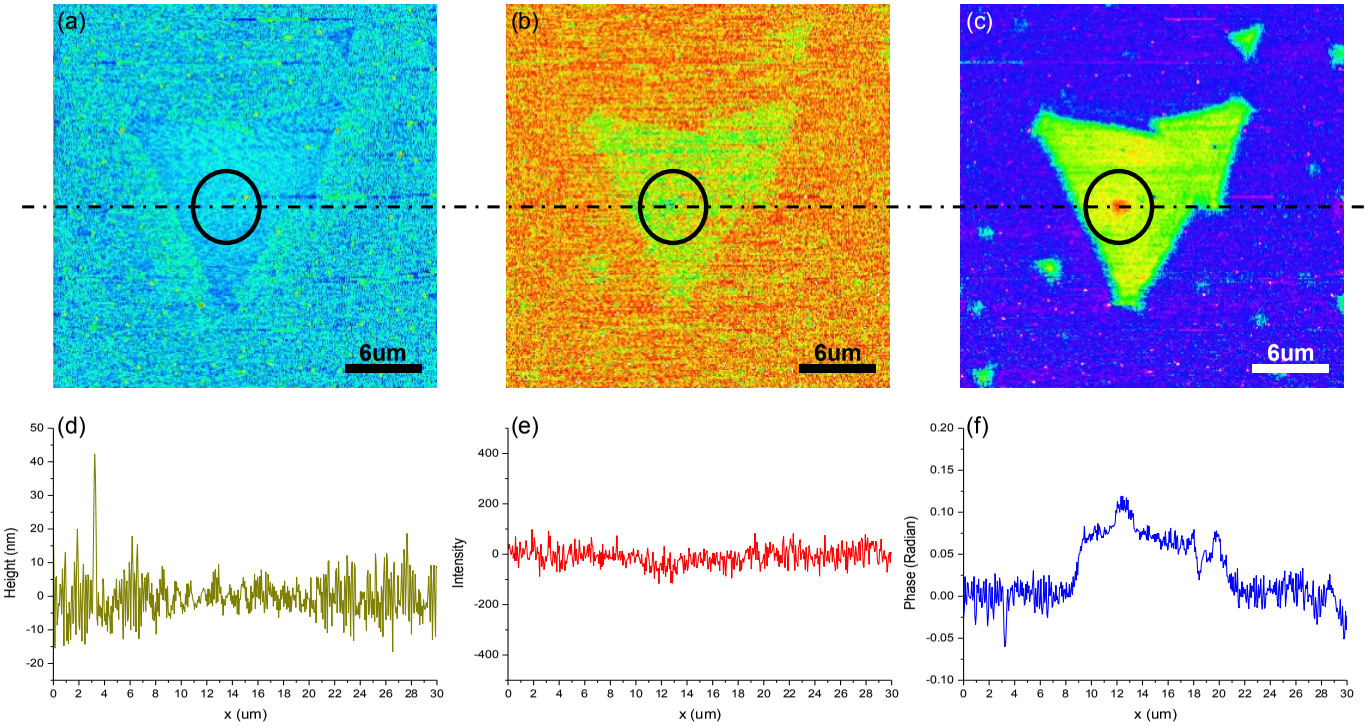


Figure 4-11: Measured results for $MoS_2$. (a) Surface topography, (b) NSOM collection signals and (c) phase variation. (d, e, f) are the cross-sectional view of (a, b, c) for the dotted-line.

## 4.4 Summary

In this chapter, near-field optical investigation is performed for 2-dimensional nanomaterials, especially graphene and monolayer molybdenum disulfide ($MoS_2$).

Graphene is a densely-packed 2D material. Because of its specific properties, graphene becomes one of the most actively researching materials nowadays. Its band structure is calculated by using a tight-binding model. The conduction and valence band meet at $\Gamma$ points in reciprocal lattice. Conical band structure is approximately calculated. Due to this unique structure, graphene has special properties like extremely high electron mobility, high Young's modulus and thermal conductivity.

Graphene is fabricated by CVD growth method. The graphene on Cu foil is transferred to quartz substrate for measurement. Fully- and partially-grown samples are prepared. For the fully-grown one, its grain boundary is imaged by near-field measurements with visible laser light. For the partially-grown one, the atomic layer can be distinguished by collection mode NSOM and NSOI measurements. The atomic-layer thickness can be easily distinguished by the near-field optical signal and the phase. Especially, the internal stress is observed only in the phase map. The graphite oxide is also investigated by NSOM and NSOI. Interesting phenomena are observed in the graphite oxide case. They show metallic reflection properties in single flake. However, the transmission is increased in the doubly stacked flakes. NSOM collection can very precisely detect this phenomena. In addition, even when the flake is covered by unwanted materials, the phase shows he clear image of the flake.

Similar investigation is performed for monolayer $MoS_2$. The sample is fabricated by CVD method on sapphire substrate directly. The $MoS_2$ sheets have triangular shape. Some of them contains seed in the middle of flake. The 6 Å thickness

atomic layer can be distinguished by the shear-force detection, near-field optical signal, and phase. The seed that can not be found in surface topography is observed in near-field optical signal and phase. Moreover, only phase result can resolve the small-size $MoS_2$ flakes.

# Chapter 5

# Localized Fluorescence and Phase Analysis of DLW Ag Structure

## 5.1 Introduction

Femtosecond direct laser writing (DLW) on a transparent material such as glasses or polymers has a various potential applicability on photonic devices: waveguide [Miura et al., 1997; Zoubir et al., 2005], three-dimensional (3D) data storage device [Canioni et al., 2008; Glezer et al., 1996], etc.. High repetition rate (>200 kHz) ultra-short laser pulses cause heat accumulation effects [Eaton et al., 2005]. Thermal energy is generally considered as a negative factor for precise laser processing, because the heat diffusion enlarges the modified volume. The influence of the temperature has been investigated by Shimizu et al., who related the size of fs laser-induced ring structures presenting a high refractive index change to the local temperature gradient [Shimizu et al., 2010]. However the thermal effects may be considered as positive for activating ionic migration or for allowing phase separation mechanisms [Royon et al., 2011]. The local precipitation of crystals within the glass

[Miura et al., 2000] or the modification of the chemical composition distribution around the laser focal volume [Kanehira et al., 2008; Liu et al., 2008] can be monitored to control the physico-chemical properties in glass in 3D. Most of the time, the modification takes place on a micrometric scale. Developing new composite materials with innovating functions is the current big challenge of fs laser structuring. One path is to introduce photosensitive ions inside the glass in which optical properties can be tailored by the interaction with the fs laser [Royon et al., 2011].

In particular, in the case of tailored silver-containing phosphate glass with ion $Ag^{+}$, fluorescent silver clusters $Ag^{+}_{mx}$ can be created under femtosecond near-infrared laser irradiation at fixed position, leading to a hollow-cylindrical spatial distribution of fluorescent silver species [Bellec et al., 2010]. Observed from the top, such hollow fluorescent cylinder appears as a ring, whose thickness can access sub-diffraction sizes while its radius is of the micron-scale. The key mechanisms contributing to this clustering is a combination of photo-reduction ($2Ag^{+} \rightarrow Ag_{0} + Ag^{2+}$), photo-dissociation, and thermal and chemical diffusions, due to heat accumulation resulting from the high repetition rate laser pulses [Bellec et al., 2009]. For structure exhibiting a ring shape, it has been recently demonstrated that silver depletion is occurring at the center of the structure.

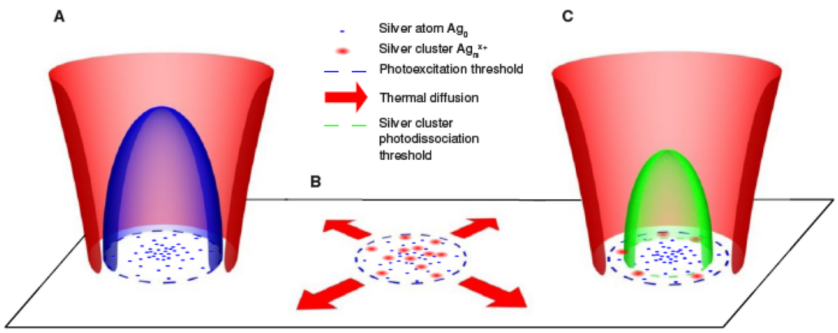


Figure 5-1: Schematic view of the nanostructures formation when DLW is performed in a Ag-containing glass [Bellec et al., 2009].

Permanent static electric fields with circular symmetry are formed in the laser-induced zone of space charge separation, made of hole and electron trapped species. Correlative microscopy studies of both fluorescence and effective second-order non-linear responses has shown that the photo-produced structure exhibits second-order nonlinearity. This nonlinearity was produced in the µm-scale structures by the charge separation and the stabilization consisting of charged silver clusters, inducing an in-homogeneous space charged distribution with an associated permanent static electric field. Fluorescence and EFISHG (electric field induced second-harmonic generation) spatial distributions has been compared, showing a clear anti-correlation of these patterns as shown in Figure 5-2 [Papon et al., 2013].

Fluorescence and SHG phenomena do not appear simultaneously as shown in the Figure 5-3. EFISHG signal appears for moderate irradiance conditions, even if the induced temperature increase does not significantly activate chemical species mobility, which corresponds thus to non-thermally driven diffusion. The EFISHG

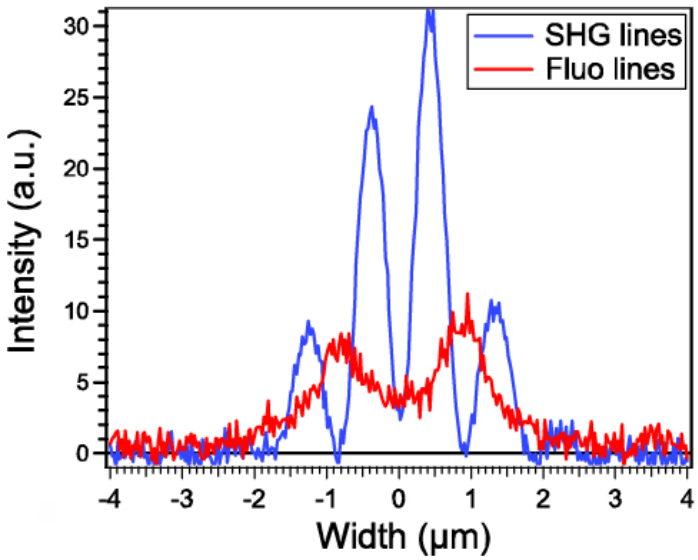


Figure 5-2: Transverse spatial distributions of fluorescence and EFISHG profiles across the structure [Papon et al., 2013].

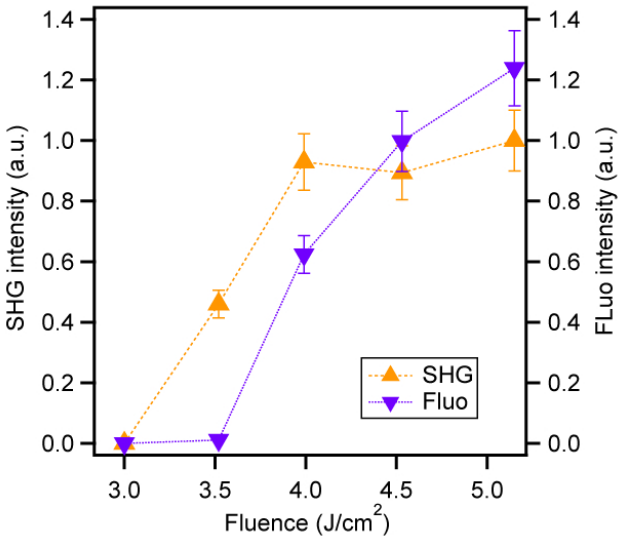


Figure 5-3: Correlative EFISHG and fluorescence relative intensities versus DLW incident fluence for $1.1 \times 10^5$ laser pulses (speed of 180 µm.s$^{-}$1). EFISHG shows a threshold behavior between 3 and 3.5 J/cm$^2$, a very steep increase followed by a plateau above 4 J/cm$^2$ corresponding to the saturation of the buried static electric field [Papon et al., 2013].

signal appears before any visible fluorescence, demonstrating the creation of a net space charge separation without cluster production (due to the initial absence of significant ion mobility). The net space charge separation thus results mainly from the entropic diffusion of free hot electrons followed by their subsequent trapping, resulting in electron migration and in the creation of a buried static electric field $\mathbf{E_{DC}}$, and in a modification of the spatial distribution of the associated electric potential $V_{DC}$. Once it has reached its saturation amplitude, the spatial distribution of given favorable electric potential values are at the root of the subsequent localized chemical stabilization and growth of the silver clusters in such glassy matrix. Therefore, the silver cluster formation is thermally activated but mostly driven by the buried electric field and the chemical stabilization is associated to the local electric potential decrease, corresponding to more favorable oxido-reduction conditions. Figure 5-4 provides a sketch of the build-up behavior of both the space charge separation

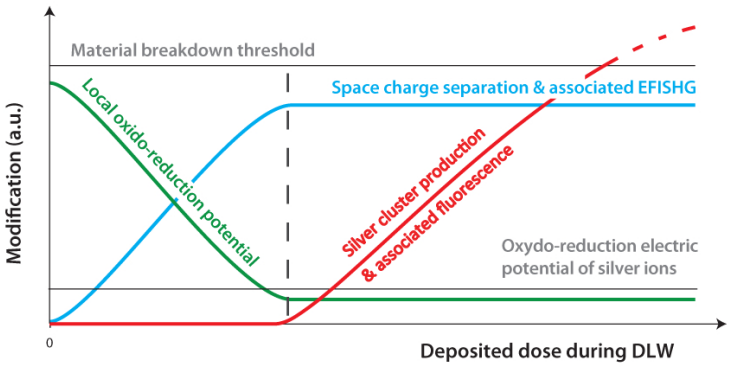


Figure 5-4: Sketch of build-up mechanisms, consisting first in a net space charge separation with a saturation plateau, subsequently followed by the growth and stabilization of silver fluorescent clusters with no visible saturation plateau here. We depict the electric field driven growth of silver clusters, and their reduction/oxidation stabilization with the associated electric potential [Papon et al., 2013].

at the root of the EFISHG, its associated electric potential modification and the subsequent fluorescence, all these mechanisms and phenomena occurring below optical damage threshold.

Indeed, the spatial distributions of distinct laser-induced silver clusters remain challenging to discrimination within the thickness of these rings, both for better understanding the physico-chemical processes at play during such direct laser writing, but also to further provide an enhanced ability in the control of the production of these photonic structures. Thus super-resolution techniques are crucial by now, to deeply enter the inner spatial distributions of these elementary fluorescent bricks. The refractive index modification profile associated to photo-induced structure has not been also determined. NSOM and interferometric NSOM techniques have been deployed in order to clarify these two aspects.

### 5.1.1 Sample Preparation

The glass is a zinc and gallium phosphate glass with silver oxide [Canioni et al., 2008; Choi et al., 2012] of composition (55% ZnO - 40% $P_2O_5$ - 4% $Ag_2O$ - 1%

$Ga_2O_3$) in molar concentration. It is fabricated by thermal melting a mixture of oxyde powders of a $(NH_4)2HPO_4$, ZnO, $AgNO_3$, $Ga_2O_3$ with appropriate ratios, then poured in a brass holder, and finally annealed. It is then cut and optically polished with typically 1 mm thickness.

Direct laser writing (DLW) is performed with a femtosecond laser (T-Pulse 500, *Amplitude Systems*, 1030 nm, 9.1 MHz), with irradiation parameters (irradiance and pulse number) controlled with an acousto-optic modulation, and focused by using an objective lens (*Mitutoyo* NIR 20 $\times$, N.A. – 0.4). Such an objective allows large diameter structures, suitable for further inner optical or chemical analysis. A silver cluster ring which has diameter of 4 μm is constructed at the focusing point. This glass sample is moving along the longitudinal direction of light propagation during DLW, so that 400 μm long fluorescent hollow-cylindrical structures are fabricated inside of the glass. $10 \times 10$ same patterns were recorded. The recorded pattern shows ring-shaped fluorescence due to the photo-reduction, photo-dissociation, and thermal and chemical diffusion [Bellec et al., 2010, 2009; Choi et al., 2012]. Figure 5-1 shows the schematic diagram of nanostructure construction during DLW.

Figure 5-5 shows the fluorescence microscope image of the sample. A commercial inverted wide-field epi-fluorescence optical microscope (*Olympus* IX71) with 20 $\times$ (top, UApo/340) and 100 $\times$ (bottom, LMPlanFI) objective lenses is used. The excitation source is xenon (Xe) lamp and fluorescence filter cube is employed for the measurement. Fluorescence filter cube is combined with 3 different filters; excitation filter, dichroic mirror, and emission filter. To achieve the image, U-MNV2 was employed. In this case, wavelength between 400 nm and 410 nm is used for the excitation, and the wavelength shorter than 455 nm is cut-off by the dichroic mirror and emission filter. Circular fluorescence ring is observed by this microscopic setup.

The highly resolved far-field image can be obtained by confocal microscope.

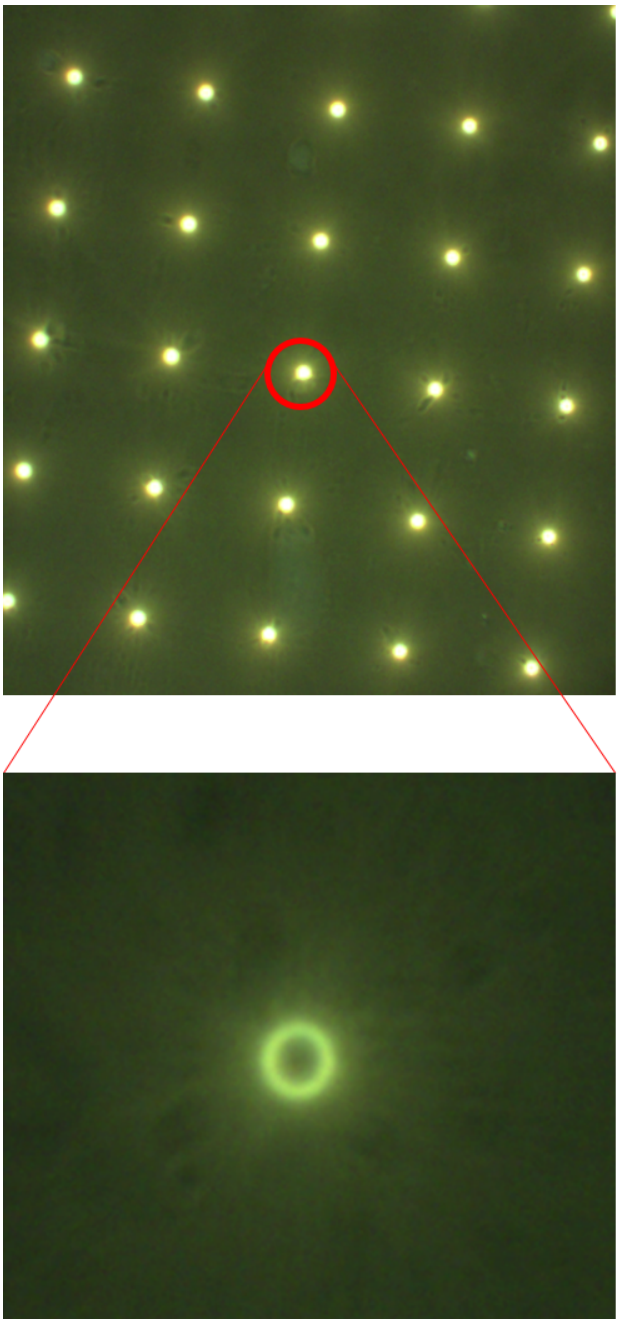

Figure 5-5: Fluorescence image of the directly laser written glass. Microscope: *Olympus* IX71, Objective: (top) UApo/340, 20 ×, N.A. - 0.75 and (bottom) LMPlanFI, 100 ×, N.A. – 0.80. Excitation source: xenon (Xe) lamp. Fluorescence filter cube: U-MNV2.

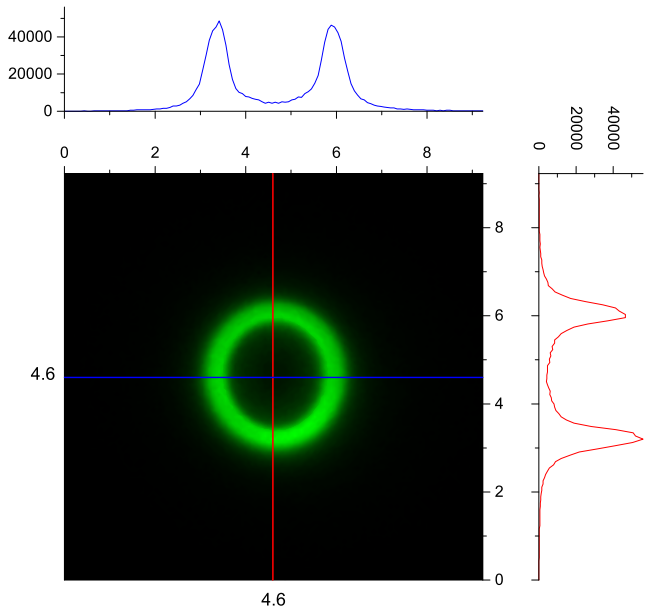


Figure 5-6: Fluorescence image of the sample by using confocal microscope with oil immersion lens (63 ×, NA – 1.4)

Figure 5-6 shows the confocal microscope image with oil immersion type objective lens (63 ×, N.A. – 1.4). The width of the fluorescence ring which can be obtained by fitting the line profiles to gaussian function is about 600 nm.

### 5.1.2 Spectral Properties

Direct laser writing on Ag-containing glass shows fluorescence as Figure 5-5, which means that the near-UV light excite the laser-structured sample and it emits light of energy lower than the source. The emission spectrum of the ring with ultra-violet (UV) (wavelength between 330 nm and 385 nm) and violet (wavelength between 400 nm and 410 nm) excitation are shown in Figure 5-7. These spectra are measured by using the same microscope as Figure 5-5. But an UV-anti reflection coated objective lens (UApo/340, 20 ×, N.A. – 0.75) is used, because the UV light cannot pass the normal optical objective lens. For UV excitation, a different filter cube (U-MWU2: excitation filter BP 330-385, dichroic mirror DM400, emission filter

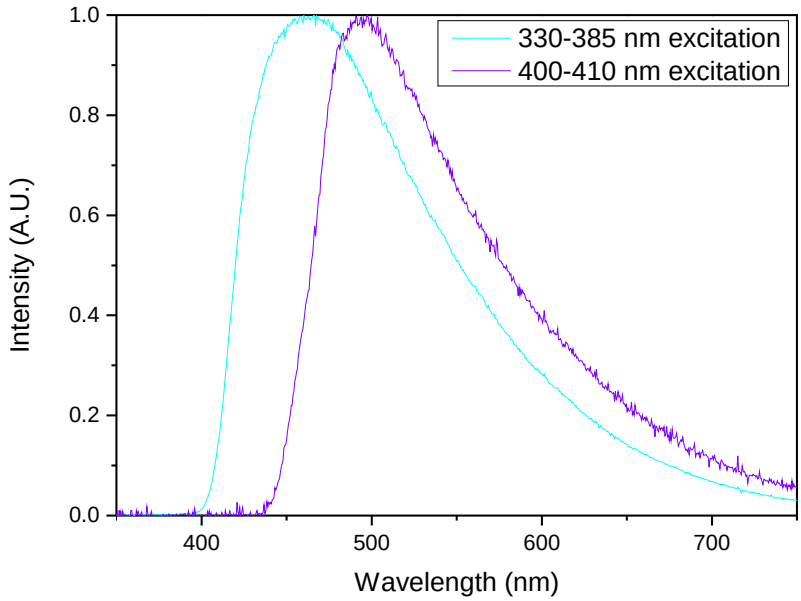


Figure 5-7: Normalized fluorescence spectra with ultra-violet and violet excitation, the short-wavelength part of each plot being affected by the cut-off transmission of the respectively used emission filters.

BA420) is used, and the same cube for Figure 5-5 is used to measure the spectrum of violet excitation.

Intense fluorescence is observed in both cases, but the fluorescence peaks are slightly different. For the case of violet excitation, the fluorescence peak is around the wavelength of 495 nm. On the other hand, the peak is slightly blue-shifted ($\sim$ 460 nm) in the case of UV excitation. Excitation and emission band of the pristine (non-irradiated) silver-containing zinc phosphate glass are around 260 nm and 365 nm [Bourhis et al., 2010], which is not excited at all here neither with the ultra-violet nor with violet excitations. Therefore, these spectra show the emission properties of the laser-irradiated and modified regions. The spectrum of violet excitation has its cut-off near 455 nm by dichroic mirror and emission filter of the cube. This means that the emission band near 460 nm can be affected by the emission filter.

## 5.2 2D Spectral Mapping by using Confocal Spectroscope

Spectrum analysis for the DLW structure was already performed in previous researches [Bourhis et al., 2010, 2013; Maurel et al., 2009]. However, localized spectral properties could not be investigated, because these researches are performed in wide-field. Confocal technique is widely used to find out localized optical property. By using spatial pinhole in front of a detector, out-of-focus light is blocked and optical signal only from the localized space is collected. Figure 5-8 illustrates the principle of confocal technique. In general, confocal technique is used for fluorescence imaging by using laser scanning (this is called CLSM. See Chapter 1) to increase the S/N ratio and resolution.

The resolution depends on the considered wavelength and on the size of pinhole. Combining this technique to spectroscopy, it is possible to focus on spectrum at specific position. In this section, the fluorescence spectrum of a DLW glass are measured in epi-collection by a commercial confocal spectrally-resolved microscope (*Horiba* LabRAM HR800).

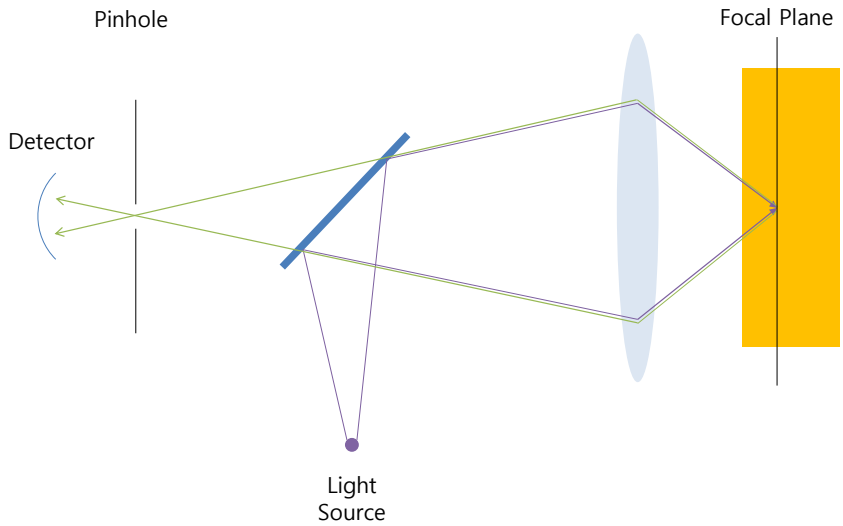


Figure 5-8: Confocal principle

### 5.2.1 Instrument

The schematic diagram for the instrument is illustrated in Figure 5-9. At the incident path, bandpass filter is located to select the excitation wavelength only and block the others. The neutral density (ND) filters control the intensity of the source. And dichroic mirror exists in front of the microscopy and emission filter is also inserted in the system to block the reflection of the excitation source. The pinhole exists for confocal purpose. And the objective lens can be replaced by purpose. The translational stage is automatically controlled by using computer to acquire the two or three dimensional spectral map. The detection is performed with a high-sensitivity CCD camera after the spectrometer stage (considered grating here : 150 grooves/mm). Finally all the operations can be controlled by using the software

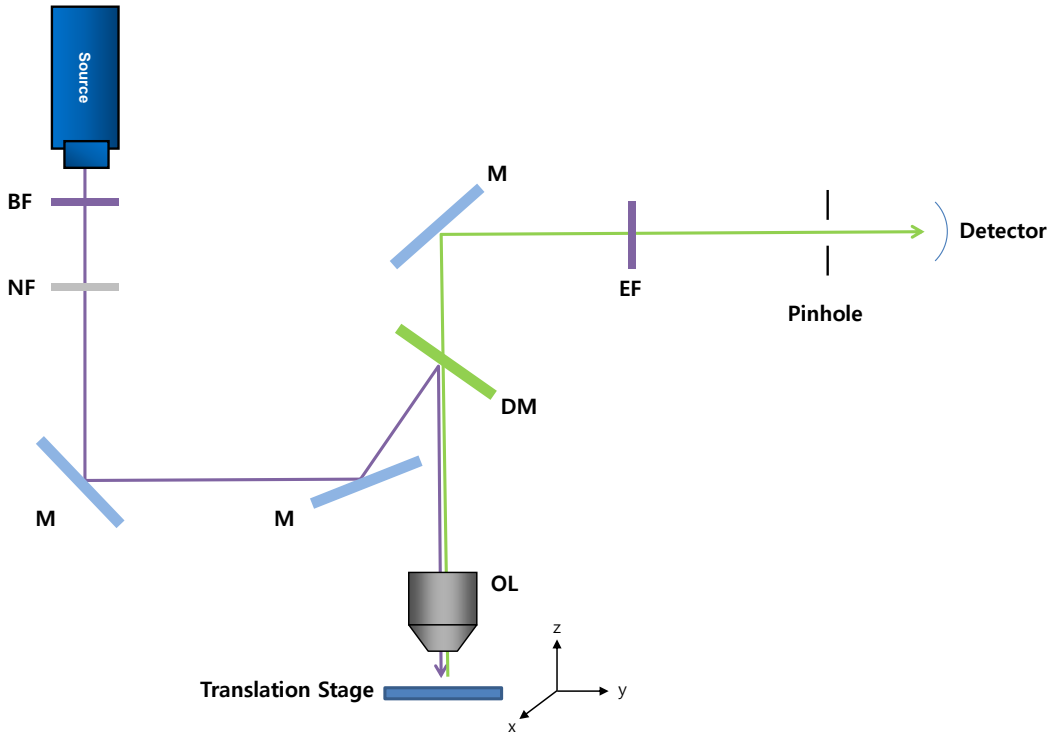


Figure 5-9: Schematic diagram for the confocal spectroscope (*Horiba* LabRAM HR800). BF: bandpass filter, NF: neutral density filter, M: mirror, DM: dichroic mirror, OL: objective lens, EF: emission filter.

called LabSpec which is provided by the manufacturer.

In order to measure the spectrum correctly, the instrument should be calibrated in a proper way. Since the spectral responses of the filters in use are not uniform for the whole range of spectrum, the data should be systematically calibrated. For this purpose, two glasses ($Mn^{2+}$ and $Cu^{+}$ containing glasses) are used as reference samples. The spectrum which are achieved by well-calibrated instrument are already prepared.

In Figure 5-10, the reference and measured spectrum are presented, and the calculated correction factors are also illustrated. $Mn^{2+}$ is used for 405 nm excitation and $Cu^{+}$ is used for 325 nm. The reference data divided by the measured one can be

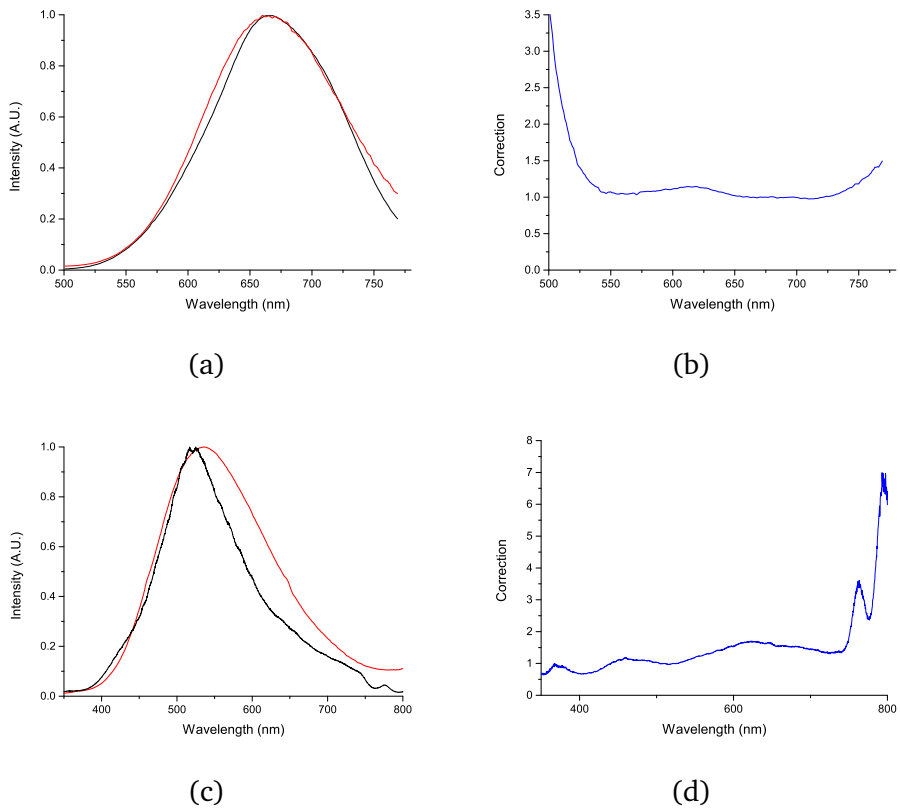


Figure 5-10: (a) Fluorescence spectrum of $Mn^{2+}$ and (b) its correction factors. (c) Fluorescence spectrum of $Cu^{+}$ and (d) its correction factors. In (a) and (c), red lines represent the reference spectrum and black lines are measured one.

the correction factor for the next experiments. If the spectrum are collected by the instruments, the data should be multiplied by the correction factor for each spectral point.

### 5.2.2 Confocal Spectral Mapping

The laterally localized properties of the glass are measured by using the confocal spectrometer. As the spectrum in section 5.1.2 shows, the pattern has the fluorescence peak near 450 nm wavelength. For this confocal measurement, 405 nm laser diode (*Coherent* OBIS 405) is used for an excitation source.

Figure 5-11 shows the fluorescence spectrum of the ring shape. The original spectrum is deformed by filters for the visible range. Therefore, the real spectrum can be found by multiplying the correction factor. The fluorescence mostly exists near 500 nm. The difference between the two spectra can be seen in the Figure 5-11. By observing the real spectrum, the raw measurement shows that the region of

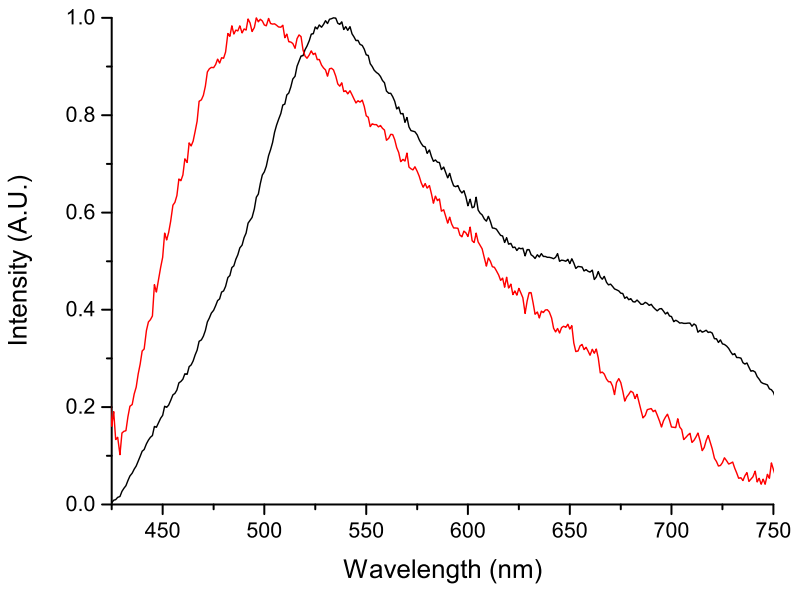


Figure 5-11: Fluorescence spectrum of the ring shape being excited at 405 nm, measured with the confocal micro-spectrometer (black line) and the related calibrated spectrum (red line).

short wavelength (under 550 nm) was initially cut and while the long wavelength was bumped up and deformed. Therefore, we confirm here the need to perform systematic and careful spectral corrections.

In Figure 5-12, the 2D spectral maps are presented. 50 μm pinhole is used for mapping. Since the DLW are performed inside of the glass, the spectrum also should be measured inside. Clear-ring shape can be found in the map, but the image looks blur. The horizontal and vertical cross section of the image clearly shows the poor contrast of the image. By fitting the line profile to the gaussian function, the full-width at half-maximum (FWHM) value and the visibility ($(I_p - I_c)/(I_p + I_c)$ where p:peak, c:center of the ring) can be calculated. In horizontal line, the FWHM are 1.41 μm for the left peak and 1.77 μm for the right. In vertical line, the FWHM are 1.22 μm for the top peak and 1.48 μm for the bottom. The contrasts for the h- and v-line are 0.269 and 0.282 for each other.

The lateral width of the fluorescence pattern is broader than expectation. Comparing to the result of confocal microscope in section 5.1.1, it is about 2.5 times broader. There are a few reasons for this result. First, this setup is not ideal for diffraction-limited imaging while it is highly relevant for highly-resolved spectroscopy, which means that the spatial resolution is not as good as one can expect from an imaging instrument. Second, the objective lens could be one of the reasons. In section 5.1.1, the objective has large numerical aperture and magnification. In general, the image quality depends on these parameters. And third, the additional glass at the top of the pattern can create aberrations on the path of fluorescence to limit the formation of a clear image. Indeed, the glass index is close to 1.6 which differs from the silica index of 1.48 for which objective was designed to compensate aberrations. Since the fluorescence is generated inside of the glass, the resolution may be increased by removing the glass at the top of the pattern. This process can make the pattern to come out at the surface.

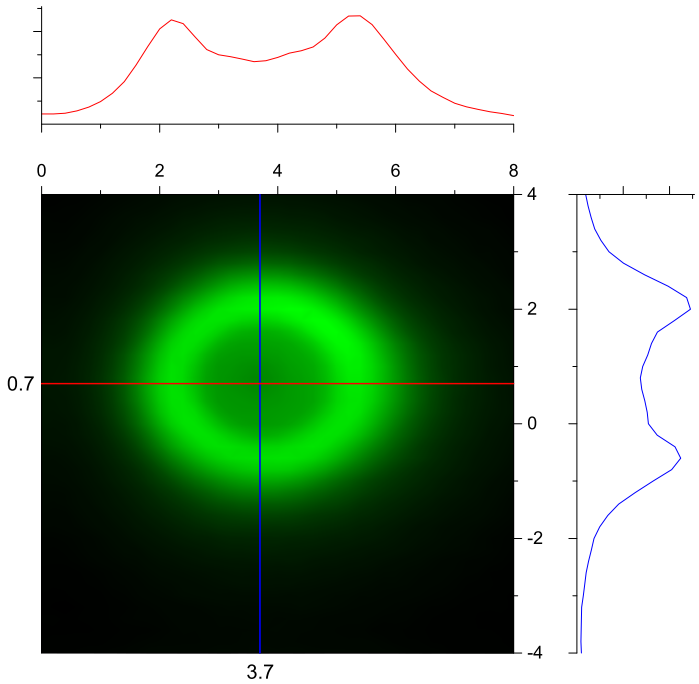


(a)

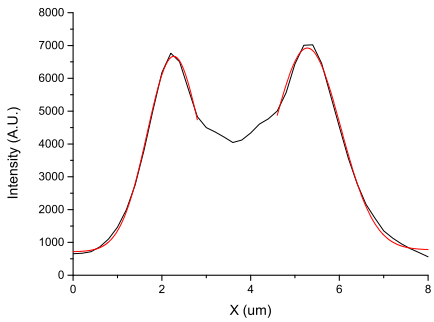


(b)

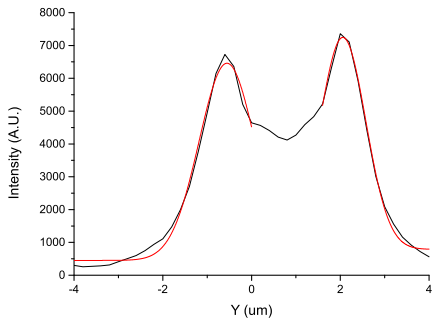


(c)

Figure 5-12: (a) 2D fluorescence mapping near fluorescence peak (∼ 500 nm) of the pattern which exists inside of the glass excited at 405 nm and related cross-sections of (a) in (b) horizontal and (c) vertical direction. 50 μm pinhole is used for mapping.

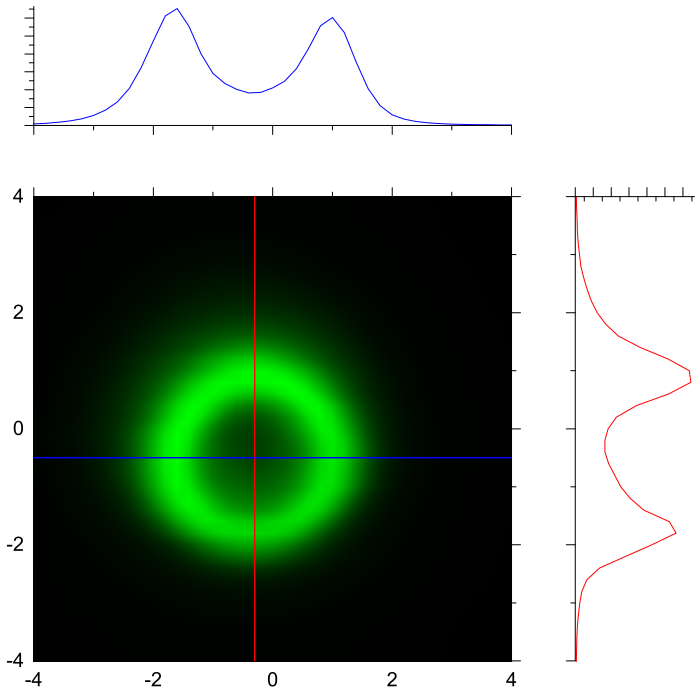


(a)

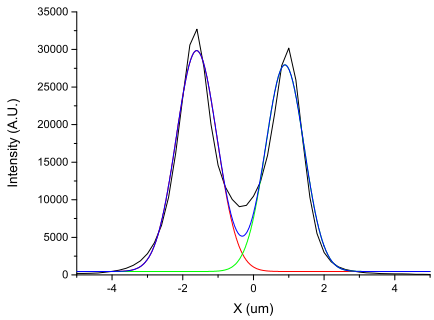


(b)

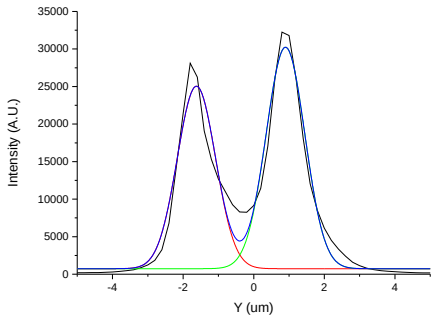


(c)

Figure 5-13: (a) 2D fluorescence mapping of the pattern near fluorescence peak ($\sim$ 500 nm) of the pattern which exists inside of the glass excited at 405 nm and related cross-sections of (a) in (b) horizontal and (c) vertical direction. 50 μm pinhole is used for mapping.

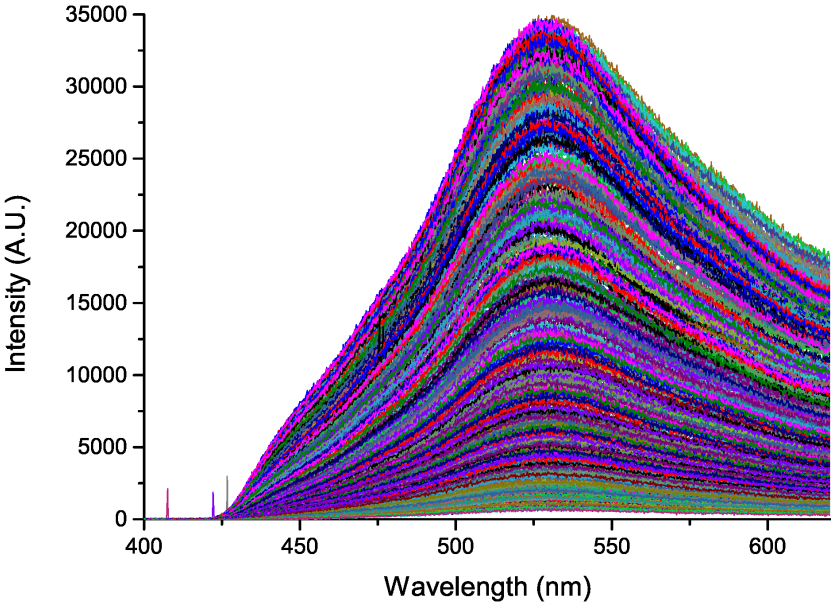


Figure 5-14: The different spectra excited at 405 nm, for each position, to generate the fluorescence map of Figure 5-12.

The glass is polished to make the fluorescence pattern coming out at the surface. The same measurement as Figure 5-12 is performed after the polishing. Figure 5-13 shows the result of the experiment. In this case, the FWHMs of the fluorescence wall decreased and the contrast increased. In horizontal line, the FWHMs are 1.36 μm for the left peak and 1.28 μm for the right. In vertical line, the FWHMs are 1.29 μm for the top peak and 1.28 μm for the bottom. The visibility for the h- and v-line are 0.565 and 0.592 for each other. However, the result are not superior because of the limitation of the instrument.

Figure 5-14 shows all the spectra of the different points in Figure 5-13 near the fluorescence ring. Indeed, all these spectra show a very similar profile and mostly differ only by their amplitude. Therefore, Figure 5-13 is plotted by integrating the whole spectra from Figure 5-14 for each point. All spectra look like similar for recorded positions. A few spectra were chosen at some points and compared in Fig-

ure 5-15. Indeed, 4 points are selected to compare their spectra. They are calibrated by using the correction factor in section 5.2.1. These points are chosen only near the fluorescence ring since the intensity is too weak elsewhere to compare the spectrum. In Figure 5-14, the red and blue lines are for the intense fluorescence region and the pink and black are for the location slightly besides the ring. The peak looks like slightly moved but there are not that big differences. However, the broadening occurs when the points exist out of the fluorescence maximum, which might result from an artificial broadening by the spectral correction in the case of low-intensity spectra.

In the case of DLW glass, it is believed that the fluorescence comes from the composition of silver clusters $Ag_m^{x+}$ ($m < 10$) [Bellec et al., 2010, 2009; Bourhis et al., 2010; Maurel et al., 2009]. The process to make the silver cluster can be described by

$$\begin{aligned}
\text{Matrix} + \hbar\omega &\rightarrow e^- + h^+ \\
Ag^+ + e^- &\rightarrow Ag^0 \\
Ag^0 + Ag^+ &\rightarrow Ag_2^+ \\
Ag_2^+ + Ag^+ &\rightarrow Ag_3^{2+} \\
&\vdots \\
&Ag_m^{x+} \qquad (\text{m} < 10)
\end{aligned}$$

which means that the different kind of clusters make the fluorescence, so the inhomogeneous broadening of the spectrum is inevitable, due to the emission overlap of distinct species. Since the writing irradiance at the border of the fluorescence wall ($x = -2.6$ μm in Figure 5-15) is smaller than at the peak position of the wall ($x = -1.6$ μm in Figure 5-15), the high $m$ ($m \sim 10$), the silver species might have

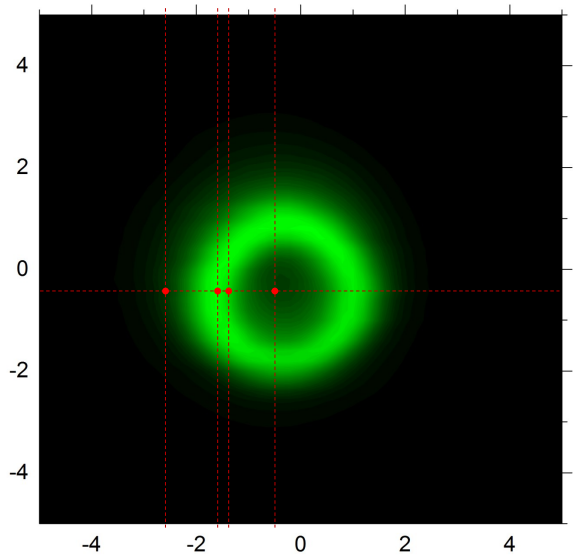


(a)

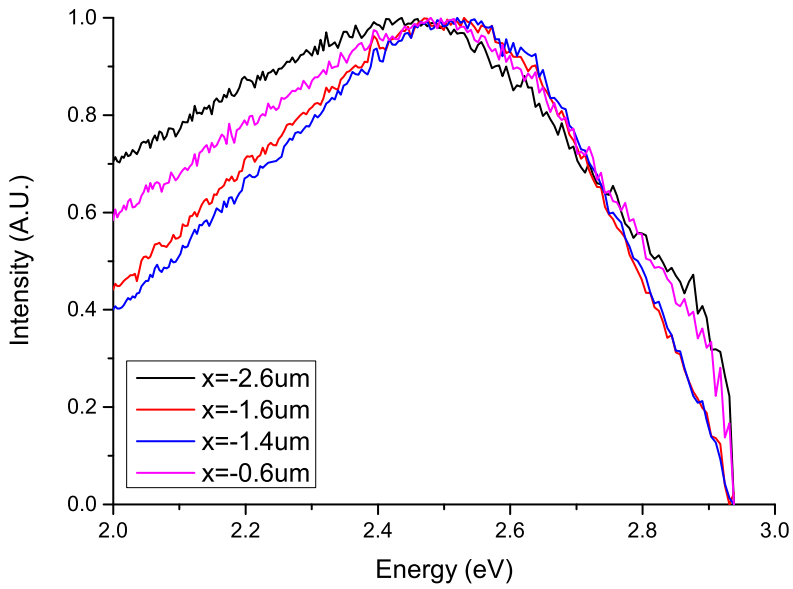


(b)

Figure 5-15: Localized spectra for fluorescence with excitation at 405 nm. (a) Selected points and (b) related normalized spectra.

different radial distributions of concentration in space and thus within the structures. Consequently, this might be observed by means of the highly-resolved spatial imaging of these laser-induced structures. However, up to now, the resolution of confocal instruments did not allow us to get into the structures, to fully resolve them spectroscopically and to observe distinct spatial distributions of distinct silver species. Such lack of information justifies to go further with super-resolution microscopy.

## 5.3 NSOM & NSOI Measurement

The fluorescence imaging [Bellec et al., 2010; Bourhis et al., 2010; Choi et al., 2012] and second harmonic generation (SHG) imaging [Choi et al., 2012; Papon et al., 2014, 2013] on such ring-shaped silver cluster structures were previously observed in far-field region. However, up to now, there is no result for near-field fluorescent properties about these kinds of glasses. NSOM is a high-resolution imaging and spectroscopic instrument for nano-scale optical samples. Sharp optical fiber probe tip with a small aperture (generally less than 100 nm) is approached to the sample surface, allowing the scanning of the surface with higher resolution than typical diffraction limit.

The SEM imaging suggests us that photo-induced silver clusters are accumulated to the 80 nm wall thickness [Bellec et al., 2009], but the ring shows the fluorescence wall thicker than 80 nm (typically from 200 to 300 nm thickness) in the fluorescence confocal microscope image [Bourhis et al., 2010]. The reason may thus be that the system is limited by diffraction (section 1.2.1). Using NSOM, it is expected that some special characteristics, unresolved with far-field approaches, can be observed in near-field regions, in order to access additional understanding about the resulting fluorescent structures and the related silver species distributions.

### 5.3.1 Near-field Fluorescence Image

#### (a) Excitation with Illumination and Collection Modes

For NSOM experiments, the ring pattern should appear at the surface. Therefore, the pristine glass was polished, so that the photo-induced structure intersects the sample surface in order to approach the NSOM fiber tip. Thermally-pulled NSOM fiber probe tip has low intensity throughput to investigate the fluorescence proper-

ties of these nano-ring. Therefore, a 100 nm aperture fiber tip obtained by chemical etching is used for collecting the optical signals and illuminating the sample, in the collection and illumination modes, respectively. The shapes of thermally-pulled and chemically-etched fiber tips can be seen in Figure 5-16.

On the one hand, the thermally-pulled fiber acts as a point-like source because of the continuously narrowing tip-end, but intensity throughput is small because of the geometry. In generally, thermally-pulled NSOM fiber which has 100 nm aperture diameter shows approximately $10^{-7} \sim 10^{-5}$ throughput [Valaskovic et al., 1995].

On the other hand, chemically-etched fiber has different shape of tip-end. This fiber type has complete shape almost at the end of the fiber, and only small needle exists. So, the electromagnetic wave is well-guided almost till the end of the fiber, and the throughput drastically increases compared to the thermally-pulled one. The fiber used in this research has throughput of the order of $10^{-2}$ (based on the manufacturer's measurement), and it has $10^3 \sim 10^5$ orders of magnitude higher than that of thermally-pulled fiber.

NSOM can be operated in various scanning modes. Because of the shape of chemically-etched fiber tip, the fluorescence signals between collection (which means that the sample is illuminated by objective lens and the signal is collected by probe tip, Figure 1-5 (a)) and illumination (which means that the sample is illuminated by probe tip and the signal is collected by objective lens, Figure 1-5 (b)) modes can be different. To verify the difference, both illumination and collection mode of NSOM operation are performed. Figure 5-17 represents the NSOM setup for illumination and collection mode, alternatively.

From spectral measurements (Figure 5-7), it can be seen that the emission band of the pattern is centered around 460 nm wavelength. So a 405 nm laser diode (LD) (*Shanghai Dream Lasers Technology Co., Ltd.*, SDL-405-LM-030T) is used to

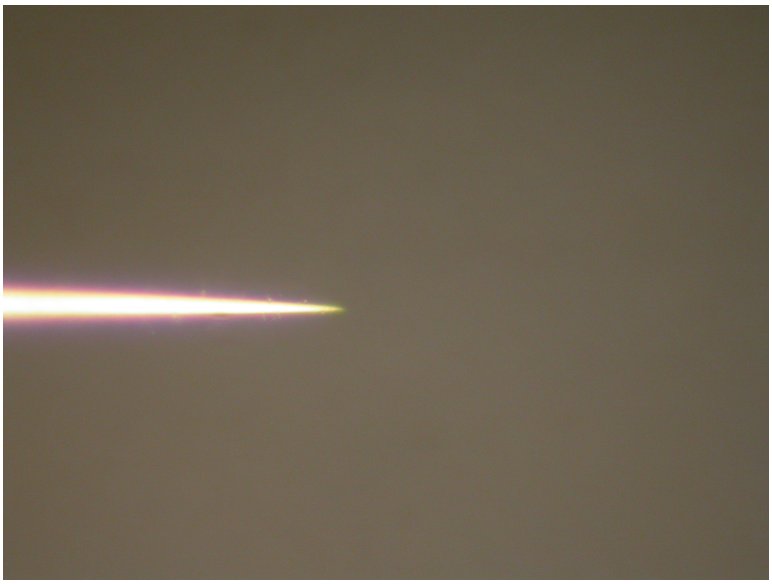

(a)

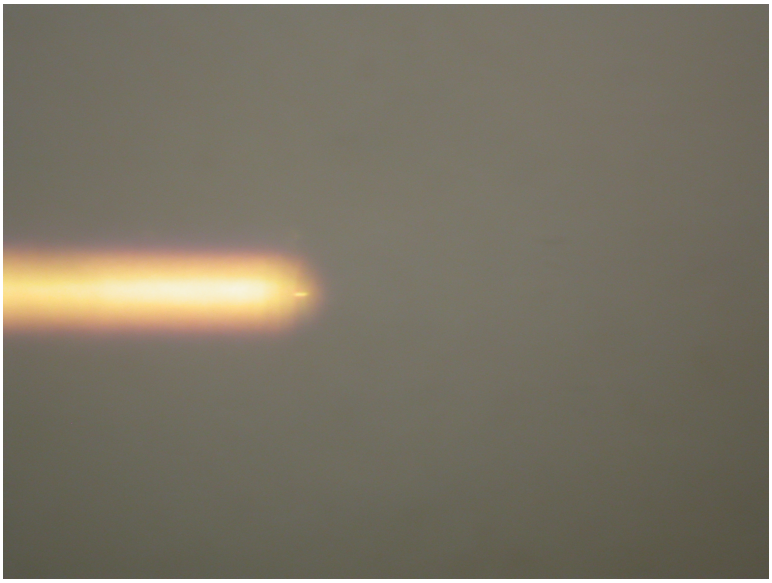

(b)

Figure 5-16: Shapes of (a) thermally-pulled and (b) chemically-etched fiber tips

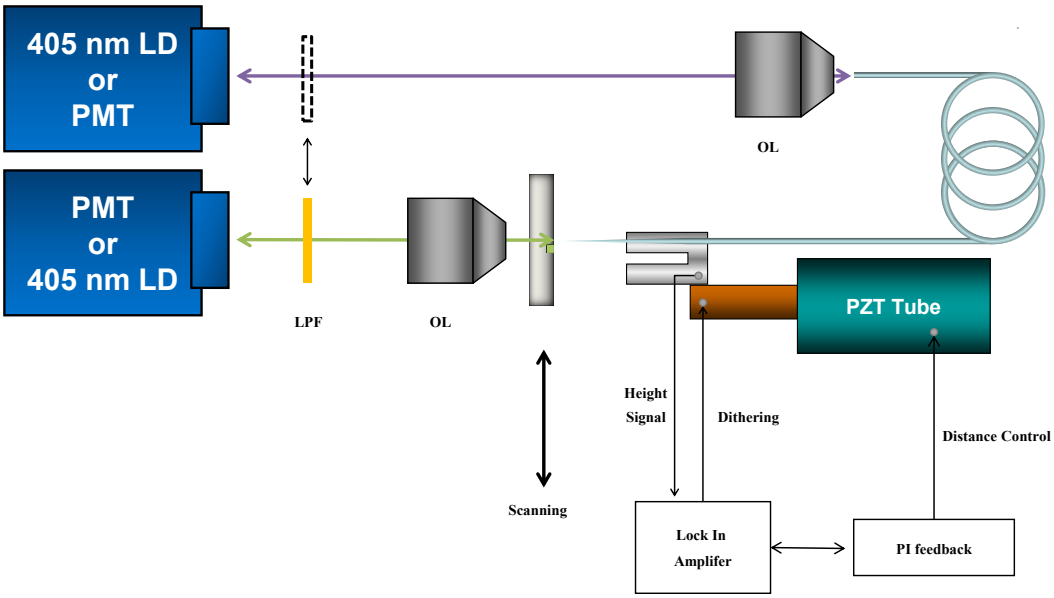


Figure 5-17: NSOM setup for illumination and collection modes. LD: laser diode, OL: objective lens, LPF: long pass filter.

excite the fluorescence, and a PMT is used to collect the fluorescent signals. A 100 nm aperture fiber tip, obtained by chemical etching (*Jasco*), is used for collecting the optical signals and illuminating the sample, in the collection and illumination modes, respectively.

Figure 5-18 (a) is the image observed by using NSOM collection mode, and (b) is the image observed by illumination mode. In both cases, the 425 nm long-pass filter is used for cutting the directly incoming LD signal. In the case of illumination mode, the ring-shaped fluorescence is clearly observed. In contrast, in the case of collection mode, it looks like that the fluorescence may be reflected by the surface of the probe tip, after that it is re-reflected from the sample surface as described in Figure 5-19. Moreover, despite the polishing stage to bring the structure to the surface, the remaining depth of the fluorescent hollow-cylindrical structures is still about several tens of microns below the sample surface. Therefore, such thickness of the fluorescent structures may also contribute to non-trivial imaging features. As

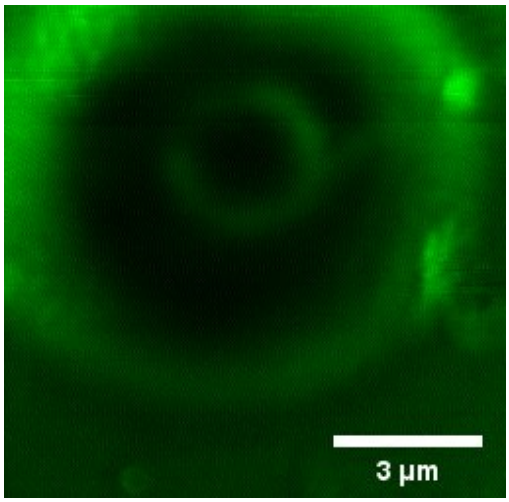


(a)

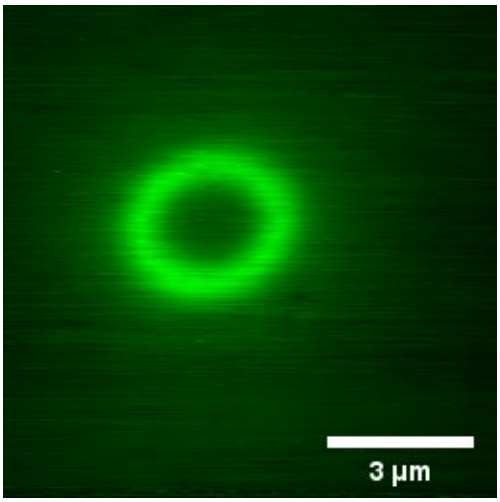


(b)

Figure 5-18: Near-field images of the ring-shape fluorescence pattern by (a) collection and (b) illumination modes.

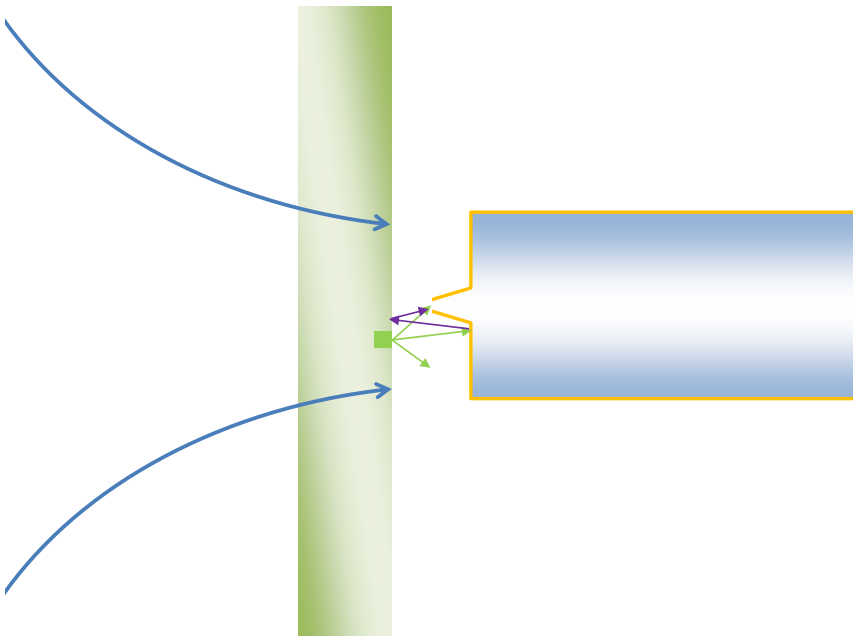

Figure 5-19: Schematic of multiple reflections of fluorescence at the end of the chemically-etched fiber tip.

the result of this experiment, it can be considered that illumination mode is more suitable than collection mode for the fluorescence experiment.

### (b) Excitation with Two Different Source

In this section, the silver cluster nano-ring at the surface on the glass is studied to obtain the fluorescence image by using NSOM with illumination mode. Two different light sources are necessary to compare the near-field characteristics between fluorescence and non-fluorescence situations; shorter and longer wavelengths than 460 nm from the spectra of the sample. A 405 nm LD is used to excite the fluorescence of the sample, and a 632.8 nm He-Ne laser is used for phase shift measurement.

Experiments are operated by illumination mode of NSOM. A schematic diagram of the setup is shown in Figure 5-20. The light sources are coupled to the back-end of the fiber with an objective lens. Then the sources pass though the fiber and stimulate

the sample with small aperture. The nano-positioning stage scans the surface of the sample in the lateral plane, and the optical signals are collected by an objective lens. A PMT is installed for detecting the fluorescent signals. A 425 nm long wavelength cut-off filter is installed to block the excitation light. The point-by-point scanned optical signals are plotted to obtain the 2D image of the fluorescent structured surface.

Figure 5-21 shows the experimental results of near-field illuminations. Figure 5-21 (a) represents the fluorescence image of the ring-shape silver cluster structure illuminated by a 405 nm LD. Ring-shape strong fluorescence is observed, meaning that silver cluster absorbs the 405 nm electromagnetic wave and then radiates photons. The lateral width of the fluorescence wall is not thin as expected. This may be related to the thick longitudinal shape. The remaining depth of the fluorescent hollow-cylindrical structures may thus contribute to non-trivial imaging features.

On the other hand, Figure 5-21 (c) shows something different. This is the result of 632.8 nm excitation. No special fluorescence ring is appeared in this figure, but

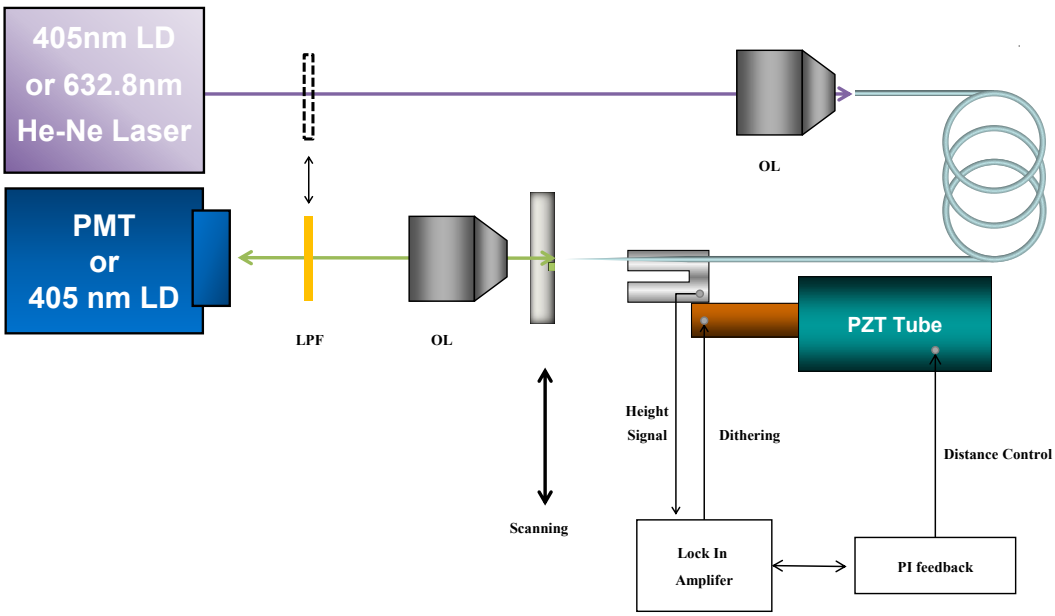


Figure 5-20: NSOM setup for illumination mode. LD: laser diode, OL: objective lens, LPF: long pass filter.

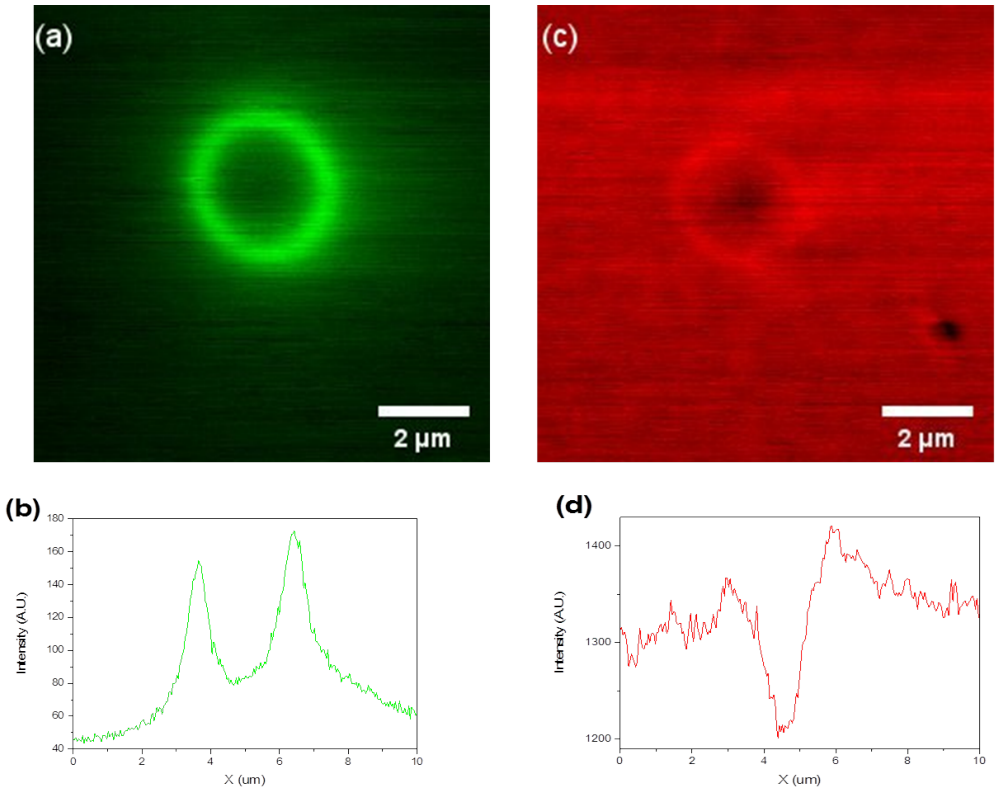


Figure 5-21: Near-field images and line profiles with 405 nm LD (a), (b) and 632.8 nm He-Ne laser (c), (d). These results show that the fluorescence only occurs at 405 nm excitation

a dark spot is observed in the center of the structure. The fluorescence originates from the accumulation of silver clusters. Therefore, the distribution of the silver ions is changed not only in the outer circle, but also in the center of the circle. This process affects the transmission and refractive index of the glass. Figure 5-21 (c) demonstrates the change of optical properties in the center of the ring. The difference between the two images (Figure 5-21 (a), (c)) can be more dramatically seen by viewing the profiles of their horizontal cross-sections (Figure 5-21 (b), (d)).

### 5.3.2 Near-field Phase Properties

The DLW on Ag-contained glass changes the spatial distribution of ions due to the photo-reduction, photo-dissociation, and thermal and chemical diffusion [Bellec et al., 2010, 2009; Choi et al., 2012]. Because of this rearrangement of ions in glass, the optical properties can locally change. The fluorescence is the result of this rearrangement. The writing conditions are important to control the properties of the sample. By using NSOI, the phase variation of the glass can be measured in nano-meter resolution. In this section, the measured laser-induced dephasing at the fluorescent structures are presented with respect to the different writing conditions, namely the incident pump irradiance and the cumulated number of pulses.

#### (a) Sample Preparation

In the previous experimental section, the glass samples had been polished to make the fluorescent structures intersect the surface. This had led to long hollow-cylindrical structures with thicknesses of several tens of microns, which may blur the NSOM imaging. To overcome this limitation, laser writing has been performed directly at the surface for the NSOI experiment, to prevent the drawbacks of long fluorescent tubes. In this section, we depict the related results obtained with struc-

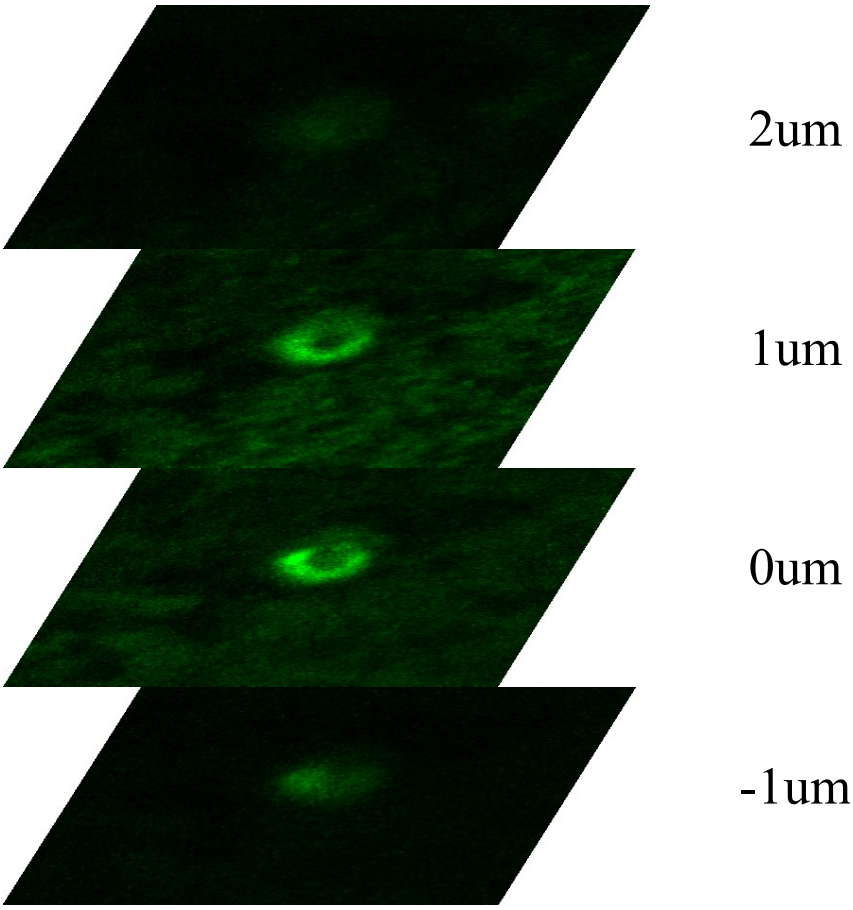


Figure 5-22: Z-stack confocal images of the ring structure, excited at 405 nm, where Z=0 corresponds to the sample's surface while positive Z values correspond to focusing conditions inside the glass sample.

| Applied voltage (V) | Focused irradiance (TW/cm$^2$) |
|---|---|
| 0.31 | 2.35 |
| 0.32 | 2.47 |
| 0.33 | 2.64 |
| 0.34 | 2.81 |
| 0.35 | 2.97 |
| 0.36 | 3.13 |
| 0.37 | 3.28 |
| 0.38 | 3.44 |

Table 5.1: Conversion of laser writing conditions from applied voltages to focused irradiances

tures that did not need to be brought back to surface, since they had been written directly at the surface.

Figure 5-22 shows the confocal fluorescence image of one of the matrix by Z-translation with 1 μm step (*Carl Zeiss* LSM700; excitation source was 405 nm LD), where the Z-axis is oriented along the propagation direction of the light excitation, where Z=0 corresponds to the sample's surface, and where positive Z values correspond to focusing conditions inside the glass sample. These images show that the fluorescence abruptly disappears 1 μm under the surface. Therefore, it can be confirmed that the fluorescent structure only exists at the surface from the Figure 5-22.

As observed with the results from the previous section, it is proved that the chemically-etched fiber tip is not suitable for the phase measurement. Therefore, the

thermally-pulled fiber tip is used in this experiment. For this experiment, interaction matrix of 24 different dots were written on Ag-doped zinc phosphate glass using femtosecond laser which has the wavelength of 1031 nm and repetition rate of 9.1 MHz (*Amplitude Systems* T-Pulse 500). The 24 conditions are composed of 8 values of irradiances (which were obtained by controlling applied voltages from 0.31 V to 0.38 V by steps of 0.01 V) and 3 values of the number of pulses ($10^4, 10^5$, and $10^6$). This corresponds to focused irradiances spanning of 2.35, 2.47, 2.64, 2.81, 2.97, 3.13, 3.28, and 3.44 TW/cm$^2$, respectively (Table 5.1). The laser profile is $TEM_{00}$ gaussian, and writing objective is *Mitutoyo* NIR 20 $\times$, N.A. – 0.4.

Figure 5-23 is the fluorescence image of the DLW glass using confocal microscope (*Carl Zeiss* LSM700; excitation source was 405 nm LD) and transmission mode optical image by inverted microscope (*Olympus* IX71; Objective was LMPlanFI, 100 $\times$, N.A. – 0.80. Three shots of pictures are combined to see the whole different dots). In Figure 5-23, the irradiances increase from bottom to top, and the number of pulses increase from left to right. By the research of Canioni et al. performed for bulk DLW [Bellec et al., 2010; Bourhis et al., 2010; Canioni et al., 2008], the fluorescence of laser-induced structure tends to increase as the irradiance and the number of pulses increase. However, in our study of laser surface structuring, the considered experimental conditions are not as distinct (especially for the range of irradiances) as those previously addressed for bulk DLW. Therefore, the fluorescence tendency in our case here is not so clear as previously. Additionally, the optical image shows that the optical property (mostly likely related to the refractive index) is more affected while the irradiance are stronger. The bottom line (irradiance = 2.35 TW/cm$^2$) shows almost nothing in this image, but the top line (irradiance = 3.44 TW/cm$^2$) shows black dots, mostly related to refractive index modifications and altered imaging conditions. The dots become darker and bigger as the irradiance increases.

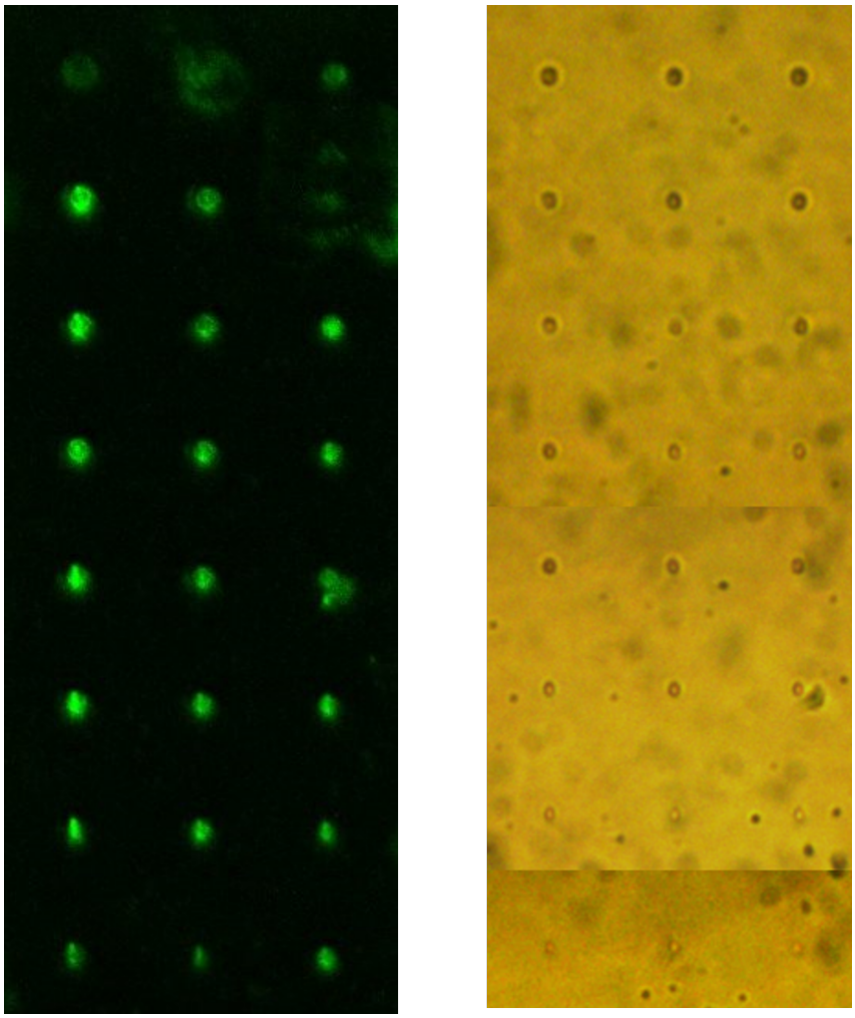

Figure 5-23: The fluorescence image of the glass using confocal microscope and optical microscope image. The excitation source for confocal image is 405 nm LD.

**(b) Phase Measurement**

Phase depends on the path-length in which the light propagates. As described in Chapter 3, OPD has the major role for phase variations. If the relative phase has the value of 0.1 radian, the related OPD(=$\Delta$(nl)) is $0.1 \times \lambda/2\pi$. In the case of 632.8 nm He-Ne laser, the value is about 10 nm. Since the material under modified pattern is not affected by DLW, we can only consider the sample near the surface. If the laser-induced pattern has the thickness of 2 μm, the related $\Delta$n may be about $5 \times 10^{-3}$.

Local modifications of the refractive index can contribute to the local variation of the light phase. Since the light reflected at the fiber tip is spherical wave, the dephasing is mainly contributed by the modification of surface. The phase detection of our system is very sensitive to OPD. When the material is homogeneous, the depth difference also can make an influence to the dephasing. However, the dephasing resulting from the surface topography is negligible as compared to the dephasing due to the index change at the surface.

For modified glass structure due to the DLW, phase of 632.8 nm He-Ne laser light is measured by using NSOI. Figure 5-24 shows 2D phase distribution (left) and surface topography (right) of the sample which are the irradiance between 2.35 to 3.44 TW/cm$^2$ (from 0.31 V to 0.38 V). The surface are pitted and the depth of pits are increased with the laser writing irradiance. Up to now, we have no clue whether such pits were directly induced by the laser irradiation, or if they appeared in time (between the laser writing process and the NSOM measurements) due to the local glass alteration and thus to a resulting differential enhancement of the glass sensitivity of corrosion by the ambient atmosphere. However, the phase images clearly show different trend compared to the surface profiles. The phase variations occur not only at the center of the ring but also near the circular boundaries. Especially,

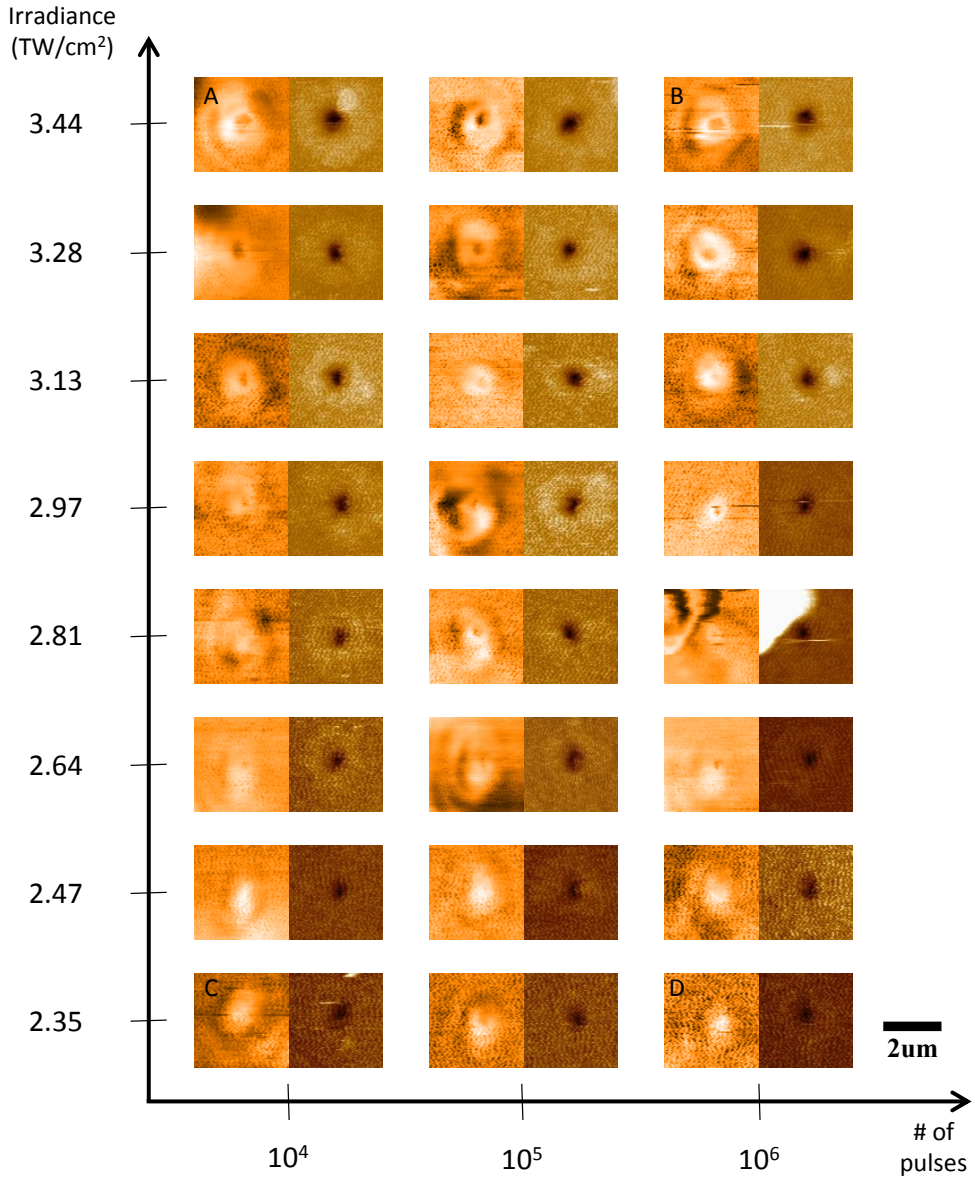


Figure 5-24: The 2D near-field mapping of phase distribution (left) and of the surface topography (right) of the structured glass.

they have changed abruptly at the center of the pattern.

In Figure 5-25, depth and phase line profiles across the laser-induced structures are presented, the related experimental conditions corresponding to the four extreme conditions displayed in Figure 5-24 (selected images of the four corners Figure 5-24). It shows different trends of both the surface and the phase profiles. Surface simply becomes indented at the center, with a much greater influence of irradiance that of the number of pulses in this range of experimental conditions. In the case of phase, irradiance also seems to play the major role. For moderate irradiances (typically from 2.35 to 2.47 TW/cm$^2$, one observes the apparition of a flat bell-shaped modification of the phase, positioned at the center of the laser-induced structure, even before a significant topological height modification (see bottom cases of Figure 5-25). Then, a threshold with respect to irradiance is observed at 2.64 TW/cm$^2$ since significant phase modifications appear. Indeed, the phase distribution reveals the creation of an additional feature, that corresponds to a sharp annular shape also centered on the laser-induced structures. Such additional phase distribution nicely overlaps with the fluorescent hollow-pipe cylindrical structures made of silver clusters. For higher irradiances (above 2.64 TW/cm$^2$), the annular distribution of phase typically increases and starts to become the dominant contribution to the phase profile while the flat bell-shaped distribution rather gradually decreases.

### (c) Correlation with Fluorescence

Figure 5-26 shows the evolution of the laser-induced phase modification versus incident irradiances, for the 3 different numbers of cumulated pulses. Such phase measurements show a non-trivial behavior. Indeed, for the highest irradiances at 3.28 and 3.44 TW/cm$^2$, the phase follows a non-monotonic evolution in the cases of N = $10^5$ and $10^6$, while phase undergoes an abrupt increase at 3.44 TW/cm$^2$. In

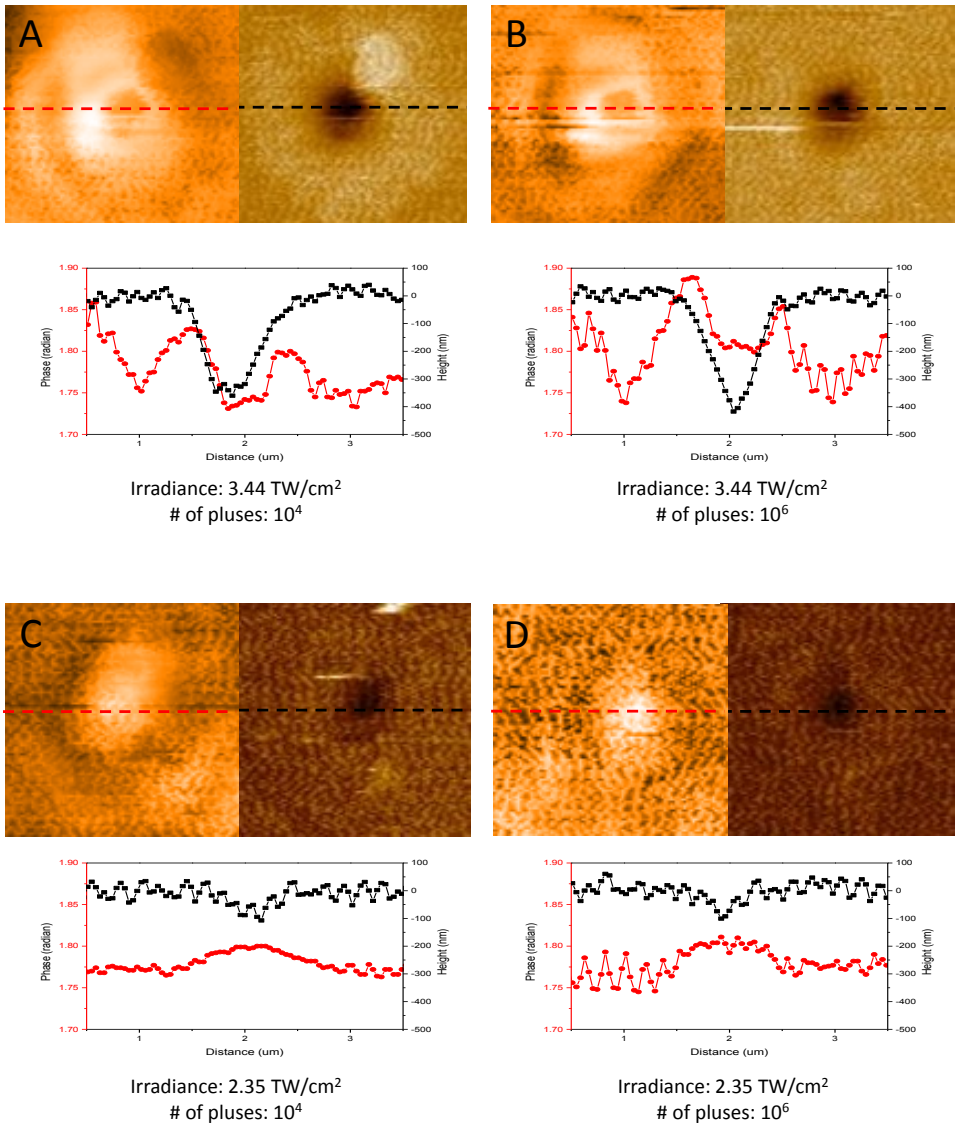


Figure 5-25: 1D horitzontal cross-sections of the 2D mapping the structured glass, showing depth (black squares) and phase (red dots) line profiles. A, B, C and D represents the same characters in Figure 5-24

this framework, the associated averaged phase behavior (for N = $10^4$, $10^5$ and $10^6$) is depicted, showing a rather continuously increasing phase modification with irradiance. Moreover, as claimed previously, one should keep in mind that the profile of the phase modification starts to differ at the irradiance threshold of 2.64 TW/cm$^2$, above which the phase profile becomes annular, similarly to the profile of the fluorescent ring structures. As visible in Figure 5-26, especially with the average phase profile, one can observe that the slope of the phase evolution gets stronger above the irradiance threshold of 2.64 TW/cm$^2$, where the annular phase profile dominates the global phase profile, which authorizes to make the direct correlation between the strong increase of the annular phase and the increase of the fluorescence signal, as seen in Figure 5-27.

For irradiances below the threshold of 2.64 TW/cm$^2$, Figure 5-27 shows that

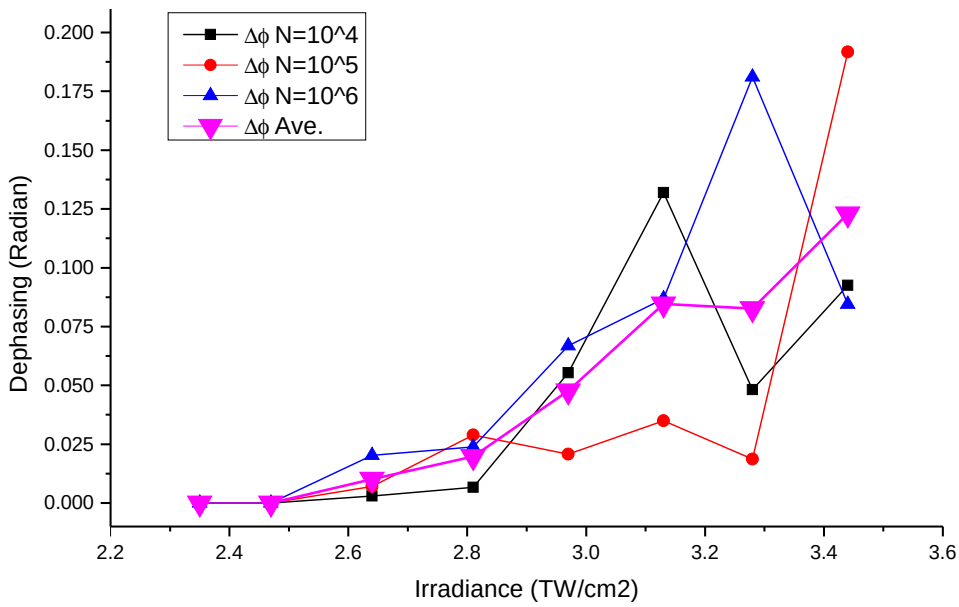


Figure 5-26: Evolution of the laser-induced phase modification versus incident irradiances, for the 3 different numbers of cumulated pulses and the associated average phase plot. Note that the profile of the phase modification differs at the irradiance threshold of 2.64 TW/cm$^2$, above which the phase profile becomes annular, similarly to the profile of the fluorescent ring structures.

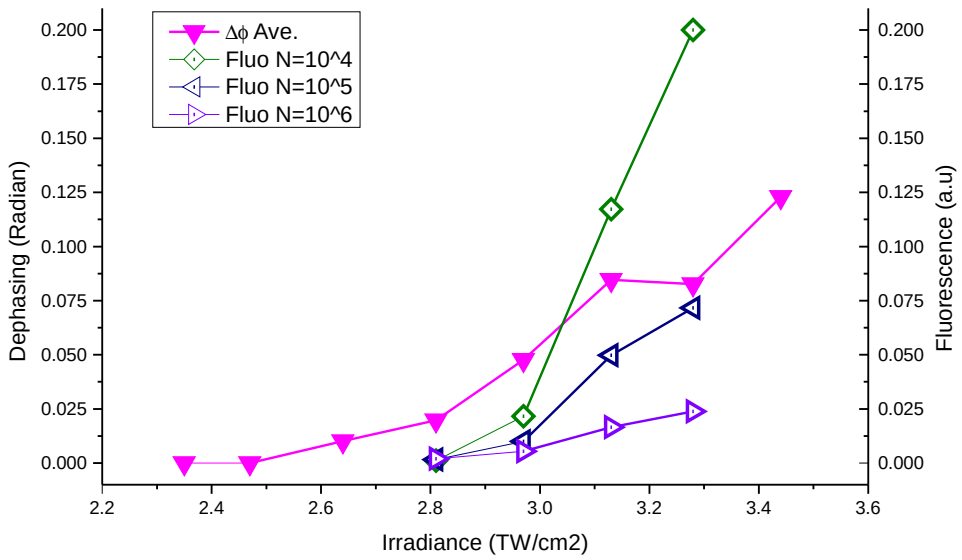


Figure 5-27: Evolution of the laser-induced mean phase modification (see Figure 5-26) and related fluorescent intensity versus incident irradiances. Note the correlation of the irradiance threshold around 2.64 TW/cm$^2$, above which the fluorescence intensity significantly grows while both phase and fluorescence profiles show an annular ring.

direct laser writing leads moderate amplitude of the phase (with a bell-shaped profile), while no significant fluorescent structures are produced. Such behavior may be attributed to limited rearrangements of the glass matrix and potentially local changes in the density. Since the sign of the dephasing can not be defined yet, it still be an open question that DLW can generate guiding structures in a glass.

Above the irradiance threshold of 2.64 TW/cm$^2$, Figure 5-27 shows that fluorescent intensities increase in a monotonic way with irradiances (the more number of pulses, the more intense fluorescence), which looks rather similar to the evolution of the phase amplitude (dominated by the annular shaped profile). Such correlative phase and fluorescence analysis leads to the following interpretation, that the local phase modification is mostly related to the local creation of silver clusters. Indeed, for such irradiances above 2.64 TW/cm$^2$, laser structuring significantly activates the thermal mobility of silver atomic species, to grow the silver clusters at the periph-

ery of the laser beam and the subsequent phase and index changes. These aspects corroborate some very recent results measured elsewhere, that have demonstrated the significant depletion of the silver ions in the central part of the irradiated spot and the related growth of silver clusters at the periphery of the beam. Finally, the bell-shaped contribution of the phase change (dominant profile below the irradiance threshold) tends to decay and disappear for high irradiances. This means that such kind of phase and index modifications tends to vanish for high irradiances. This may be related to significant thermal effects being cumulated for high irradiances, which could globally affect the glass network and thus relax the initial phase modification.

The observations from Figures 5-28 and 5-26 provide correlative information that give way to the following interpretation of the sequence of mechanisms at play during DLW. Indeed, Figure 5-28 qualitatively depicts the sketch of the modification ranges for DLW at the sample's surface, with a deposited dose that allows modifications without ionic mobilities (Figure 5-28, area A.), followed by a higher deposited dose that activates ionic mobilities, as notably silver ion or silver atoms, (Figure 5-28, area B.). The proposed sketch of mechanisms complete here the description of Papon et al., 2013 [Papon et al., 2013], where space charge separation and the associated electric field second harmonic generation occurred prior the creation of fluorescent silver clusters. One should note here that the phase profiles (both the bell-shaped profile above the modification profile and below the ionic mobility activation, and the annular-shaped profile above the latter) differ from the EFISHG profile, demonstrating that the refractive index modification is more related to the charge separation and also to the ionic redistribution (especially from silver species) than from an electro-optic modification due to the laser-induced frozen static electric field.

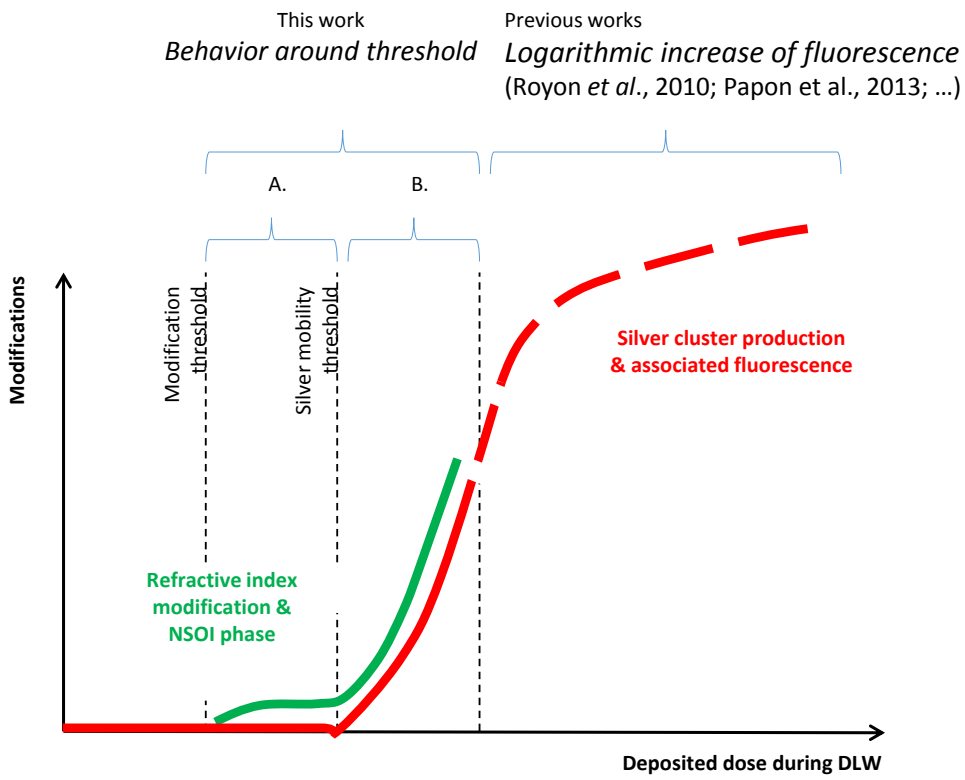


Figure 5-28: Sketch of the modification mechanisms for DLW at the sample's surface, consisting first in a bell-shaped modification without significant ionic mobility (area A.), and second in an annular-shaped modification where phase modifications are dominated by the creation of silver clusters related to the thermal activation of the ionic mobility (area B.), while the bell-shape contribution decreases due to such ionic motions.

## 5.4 Summary

In this chapter, the objective was to use super-resolution approaches to overcome the diffraction limitation of confocal fluorescence microscopy. Therefore, near-field optical microscopy and interferometric near-field optical microscopy are performed to investigate the inner structures of laser-induced modifications in a photosensitive glass.

In the first section, the concept of direct laser writing is explained. Silver-contained glass is prepared by thermal treatment of powders mixture and standard annealing method. Direct laser writing is performed in the bulk of the glass by using near-IR femtosecond laser, which makes ring-shape modification at focused point. This sample emits fluorescence near 450 nm for a near-UV excitation at 405 nm.

The 2D spectral mapping of the pattern is performed by using confocal spectroscope. The instrument is calibrated first, and a silver-containing photosensitive glass (of molar composition 55% ZnO - 40% $P_2O_5$ - 1% $Ga_2O_3$ - 4% $Ag_2O$) is investigated. For such glass composition, a 405 nm LD is used to excite the fluorescence, to make confocal fluorescence images of the fluorescent walls of the hollow-pipe laser-induced cylindrical structures.

Bulk DLW in the photosensitive glass is studied by using near-field instrument. To intersect the pattern to surface, the sample is prepared by polishing the glass. First, fluorescence properties are investigated. In order to excite the fluorescence by sub-wavelength aperture, chemically-etched fiber tip is necessary. Because of the geometrical shape of the fiber tip, illumination mode NSOM is better than collection mode. The thickness of the fluorescence wall is not thin as expected, but the optical property change in the center of the ring pattern is observed. Despite the near-field approach, the remaining thickness of the structures appear as a limiting factor for

the imaging resolution.

In a final part, the DLW is only performed to the surface, to reduce the thickness of the structures. The patterns have been prepared for various writing conditions. Near-field phase for DLW glass is measured by NSOI. From the phase map, the writing irradiance threshold can be observed, while no significant ionic mobility is thermally activated by cumulative effects, leading to a bell-shaped profile. For higher irradiances, ionic mobility is activated, which leads to the creation of a ring-shaped profile related to the creation of fluorescent silver clusters. Such high irradiances and subsequent ionic mobilities tend to reduce the initial bell-shaped profile. From these results, a reasonable interpretation about the laser-induced phase is that such an annular phase profile is built-up by the creation of fluorescent silver clusters, once irradiances are higher than the related threshold. Therefore, the annular distribution of the phase follows the space charge separation and the distribution of silver ions that locally combine to create the silver clusters at the periphery of the laser beam thanks to thermal effect accumulation. Such demonstration contributes to consider that the phase profile is related to the modifications of charge densities and new chemical species. Finally, this highlights that these phase profiles do not show predominant static Kerr-like electro-optic effects induced by the buried static electric field that results from DLW in these glasses.

# Chapter 6

# Conclusion

Near-field detection is one of the super-resolution optical imaging techniques, which can overcome the diffraction limit around $0.61\lambda/\mathrm{N.A.}$. The phase of light has significant information about material's property. NSOI is a phase detection instrument which combine NSOM with interferometry. By using NSOI, surface topography, collection mode near-field optical signal and phase variation can be detected simultaneously. The unwanted background signal can be removed by using 2-step scanning method, which is based on basic interference theory.

The details of NSOM system is explained in Chapter 2. The distance regulation is the most important scheme to construct a NSOM setup. The tuning fork based shear-force detection scheme is selected to regulate the distance between surface and probe tip. Various electronic devices and instruments are necessary to construct the NSOM system. All the components should be controlled by computer. The operating software is coded by LabVIEW programming language. The details are interpreted in Chapter 2.

In Chapter 3, a new phase detection method, which is called NSOI, is explained. The details to detect phase signal with high lateral resolution is described. Moreover,

a formula to remove the background signal is proposed and illustrated. The feasibility of the method can be determined by a *figure of merit*, OPD. To test the feasibility, phase measurements for SNG01 and specially prepared optical discs (CD, DVD and blu-ray disc) are performed by the constructed NSOM instrument. The difference in the optical properties of the materials can be clearly distinguished by phase of SNG01. In addition, 95 nm depth resolution can be demonstrated by the results obtained from optical discs in OPD. In particular, laterally resolved phase variation of sub-diffraction limit can be found in blu-ray disc measurement.

By using this instrument, optical properties of various nano-materials are investigated. In Chapter 4, 2-dimensional nanomaterials are investigated. Phase variations of monolayer graphenes are studied. Graphene is a 2D honeycomb lattice monolayer sheet composed of carbon element. Fully- and partially-grown sample are studied. The lines which are attributed to grain boundaries are observed in fully-grown sample in the near-field images. From the results of partially-grown graphene, thickness of atomic scale can be resolved by near-field investigation. The internal stress are also revealed in the phase map. An aged sample immersed into acetone for few hours shows property changes. High reflection of hexagonal shape flakes can be found from this process. The overlapped area of the two flakes is investigated by NSOM and NSOI. The high transmission is observed in the overlapped region. Moreover, the phase image gives the information about which flake covers the other one. Similar investigation is performed for monolayer $MoS_2$. The atomic layer can be observed by shear-force detection, near-field optical signal and phase. The seed that can not be found in surface topography is observed in near-field optical signal and phase. Moreover, only phase result can resolve some small-size $MoS_2$ flakes.

Chapter 5 talks about the direct laser writing (DLW) in silver-containing glass. Femtosecond laser can make a ring shape fluorescence pattern at the focused point.

Fluorescence properties of laser-induced silver clusters in a non-commercial silver-containing zinc phosphate glass (of molar composition 55% ZnO - 40% $P_2O_5$ - 1% $Ga_2O_3$ - 4% $Ag_2O$) investigated by using confocal spectrometer. Bulk DLW in the photosensitive glass is studied by using NSOM and NSOI. The fluorescence are measured by illumination and collection mode NSOM. The thickness of the fluorescence wall is not thin as expected, but the optical property change in the center of the ring pattern is observed. Moreover, writing threshold is observed in the phase image by using NSOI, correlatively to what observed in fluorescence measurements. The result demonstrates that, above the fluorescence laser writing threshold, the dominant ring-shaped phase profile is related to the modifications of charge densities and new chemical species, namely the fluorescent silver clusters. Finally, this highlights that these phase profiles do not show predominant static Kerr-like electro-optic effects induced by the buried static electric field that results from DLW in these glasses.

In conclusion, a novel technique to measure the phase with ultra-sensitivity and high-resolution is proposed in this thesis. In particular, it is demonstrated that new information on the materials can be obtained with this technique. NSOI can be expected as a promising and versatile instrument for investigating nano-materials.

In terms of perspectives, we have shown that NSOI opens new abilities and approaches for correlative super-resolution imaging. NSOI should further provide optical information of various materials, including biological and chemical structures, which cannot be obtained by conventional microscope, or even NSOM. The sign of dephasing should bring new insight, to finalize the complete analysis and exploitation of the measurements that can be achieved by NSOI. In this framework, such retrieval of the dephasing sign may lead in some cases to more specific information about the considered material, which cannot be obtained by other techniques. Additionally, NSOI can be improved by taking advantage of multi-wavelength alignment and polarization-dependent systems, or by combining other special optical

techniques such as photo-acoustic detection, high-order harmonic generation and spectroscopy.

# Bibliography


Aigouy, L., P. Prieto, A. Vitrey, J. Anguita, A. Cebollada, M. U. Gonzalez, A. Garcia-Martin, J. Labeguerie-Egea, and M. Mortier (2011). Strong near-field optical localization on an array of gold nanodisks. *Journal of Applied Physics 110*(4), 044308. [page 5]

Akamine, S., H. Kuwano, and H. Yamada (1996). Scanning near-field optical microscope using an atomic force microscope cantilever with integrated photodiode. *Applied Physics Letters 68*(5), 579–581. [page 5, 19]

Ash, E. A. and G. Nicholls (1972). Super-resolution aperture scanning microscope. *Nature 237*(5357), 510–512. [page 4]

Bae, S., H. Kim, Y. Lee, X. Xu, J.-S. Park, Y. Zheng, J. Balakrishnan, T. Lei, H. Ri Kim, Y. I. Song, Y.-J. Kim, K. S. Kim, B. Özyilmaz, J.-H. Ahn, B. H. Hong, and S. Iijima (2010). Roll-to-roll production of 30-inch graphene films for transparent electrodes. *Nature Nanotechnology 5*(8), 574–578. [page 91]

Bai, C. (2000). *Scanning Tunneling Microscopy and Its Application* (2nd ed.). Berlin ; New York: Springer. [page 3]

Balandin, A. A., S. Ghosh, W. Bao, I. Calizo, D. Teweldebrhan, F. Miao, and C. N. Lau (2008). Superior thermal conductivity of single-layer graphene. *Nano Letters 8*(3), 902–907. [page 83]

Balistreri, M. L. M., J. P. Korterik, L. Kuipers, and N. F. van Hulst (2000). Local observations of phase singularities in optical fields in waveguide structures. *Physical Review Letters 85*(2), 294–297. [page 15]

Bellec, M., A. Royon, K. Bourhis, J. Choi, B. Bousquet, M. Treguer, T. Cardinal, J.-J. Videau, M. Richardson, and L. Canioni (2010). 3D patterning at the nanoscale of fluorescent emitters in glass. *The Journal of Physical Chemistry C 114*(37), 15584–15588. [page 106, 110, 122, 125, 133, 136]

Bellec, M., A. Royon, B. Bousquet, K. Bourhis, M. Treguer, T. Cardinal, M. Richardson, and L. Canioni (2009). Beat the diffraction limit in 3D direct laser writing in photosensitive glass. *Optics Express 17*(12), 10304–10318. [page xxvi, 106, 110, 122, 125, 133]

Benameur, M. M., B. Radisavljevic, J. S. Héron, S. Sahoo, H. Berger, and A. Kis (2011). Visibility of dichalcogenide nanolayers. *Nanotechnology 22*(12), 125706. [page 83, 100]

Betzig, E., P. L. Finn, and J. S. Weiner (1992). Combined shear force and near-field scanning optical microscopy. *Applied Physics Letters 60*(20), 2484–2486. [page 19, 20]

Betzig, E., A. Lewis, A. Harootunian, M. Isaacson, and E. Kratschmer (1986). Near field scanning optical microscopy (NSOM): Development and biophysical applications. *Biophysical Journal 49*(1), 269–279. [page 4]

Blake, P., E. W. Hill, A. H. C. Neto, K. S. Novoselov, D. Jiang, R. Yang, T. J. Booth, and A. K. Geim (2007). Making graphene visible. *Applied Physics Letters 91*(6), 063124. [page 92]

Bolotin, K. I., K. J. Sikes, Z. Jiang, M. Klima, G. Fudenberg, J. Hone, P. Kim, and H. L. Stormer (2008). Ultrahigh electron mobility in suspended graphene. *Solid State Communications 146*(9–10), 351–355. [page 83]

Born, M. and E. Wolf (1999). *Principles of Optics: Electromagnetic Theory of Propagation, Interference and Diffraction of Light* (7th ed.). Cambridge University Press. [page 6]

Bostwick, A., F. Speck, T. Seyller, K. Horn, M. Polini, R. Asgari, A. H. MacDonald, and E. Rotenberg (2010). Observation of plasmarons in quasi-freestanding doped graphene. *Science 328*(5981), 999–1002. [page 83]

Bourhis, K., A. Royon, M. Bellec, J. Choi, A. Fargues, M. Treguer, J.-J. Videau, D. Talaga, M. Richardson, T. Cardinal, and L. Canioni (2010). Femtosecond laser structuring and optical properties of a silver and zinc phosphate glass. *Journal of Non-Crystalline Solids 356*(44–49), 2658–2665. [page 113, 114, 122, 125, 136]

Bourhis, K., A. Royon, G. Papon, M. Bellec, Y. Petit, L. Canioni, M. Dussauze, V. Rodriguez, L. Binet, D. Caurant, M. Treguer, J.-J. Videau, and T. Cardinal (2013). Formation and thermo-assisted stabilization of luminescent silver clusters in photosensitive glasses. *Materials Research Bulletin 48*(4), 1637–1644. [page 114]

Canioni, L., M. Bellec, A. Royon, B. Bousquet, and T. Cardinal (2008). Three-dimensional optical data storage using third-harmonic generation in silver zinc phosphate glass. *Optics Letters 33*(4), 360–362. [page 105, 109, 136]

Carney, P. S., B. Deutsch, A. A. Govyadinov, and R. Hillenbrand (2012). Phase in nanooptics. *ACS Nano 6*(1), 8–12. [page 15]

Castellanos-Gomez, A., N. Agraït, and G. Rubio-Bollinger (2010). Optical identification of atomically thin dichalcogenide crystals. *Applied Physics Letters 96*(21), 213116. [page 83]

Chen, J., M. Badioli, P. Alonso-González, S. Thongrattanasiri, F. Huth, J. Osmond, M. Spasenović, A. Centeno, A. Pesquera, P. Godignon, A. Zurutuza Elorza, N. Camara, F. J. G. de Abajo, R. Hillenbrand, and F. H. L. Koppens (2012). Optical nano-imaging of gate-tunable graphene plasmons. *Nature 487*(7405), 77–81. [page 83]

Cho, E.-H., S.-M. Kang, J. B. Leen, S.-D. Suh, J.-S. Sohn, C.-Y. Moon, N.-C. Park, L. Hesselink, and Y.-P. Park (2010). Polymeric light delivery via a C-shaped metallic aperture. *Journal of the Optical Society of America B 27*(7), 1309–1316. [page 5]

Choi, J., M. Bellec, A. Royon, K. Bourhis, G. Papon, T. Cardinal, L. Canioni, and M. Richardson (2012). Three-dimensional direct femtosecond laser writing of second-order nonlinearities in glass. *Optics Letters 37*(6), 1029–1031. [page 109, 110, 125, 133]

Courjon, D., K. Sarayeddine, and M. Spajer (1989). Scanning tunneling optical microscopy. *Optics Communications 71*(1-2), 23–28. [page 4]

Creath, K. and G. Goldstein (2012). Dynamic quantitative phase imaging for biological objects using a pixelated phase mask. *Biomedical Optics Express 3*(11), 2866–2880. [page 15]

Ctistis, G., E. H. Frater, S. R. Huisman, J. P. Korterik, J. L. Herek, W. L. Vos, and P. W. H. Pinkse (2011). Controlling the quality factor of a tuning-fork resonance between 9 and 300 K for scanning-probe microscopy. *Journal of Physics D: Applied Physics 44*(37), 375502. [page 31]

Dean, C. R., A. F. Young, I. Meric, C. Lee, L. Wang, S. Sorgenfrei, K. Watanabe, T. Taniguchi, P. Kim, K. L. Shepard, and J. Hone (2010). Boron nitride substrates for high-quality graphene electronics. *Nature Nanotechnology 5*(10), 722–726. [page 83]

Deutsch, B., R. Hillenbrand, and L. Novotny (2008). Near-field amplitude and phase recovery using phase-shifting interferometry. *Optics Express 16*(2), 494–501. [page 15]

Deutsch, B., R. Hillenbrand, and L. Novotny (2010). Visualizing the optical interaction tensor of a gold nanoparticle pair. *Nano Letters 10*(2), 652–656. [page 15]

Dorfmuller, J., D. Dregely, M. Esslinger, W. Khunsin, R. Vogelgesang, K. Kern, and H. Giessen (2011). Near-field dynamics of optical Yagi-Uda nanoantennas. *Nano Letters 11*(7), 2819–2824. [page 5]

Duong, D. L., G. H. Han, S. M. Lee, F. Gunes, E. S. Kim, S. T. Kim, H. Kim, Q. H. Ta, K. P. So, S. J. Yoon, S. J. Chae, Y. W. Jo, M. H. Park, S. H. Chae, S. C. Lim, J. Y. Choi, and Y. H. Lee (2012). Probing graphene grain boundaries with optical microscopy. *Nature 490*(7419), 235–239. [page 94]

Eaton, S., H. Zhang, P. Herman, F. Yoshino, L. Shah, J. Bovatsek, and A. Arai (2005). Heat accumulation effects in femtosecond laser-written waveguides with variable repetition rate. *Optics Express 13*(12), 4708–4716. [page 105]

Eda, G., G. Fanchini, and M. Chhowalla (2008). Large-area ultrathin films of reduced graphene oxide as a transparent and flexible electronic material. *Nature Nanotechnology 3*(5), 270–274. [page 91]

Eisele, D. M., J. Knoester, S. Kirstein, J. P. Rabe, and D. A. Vanden Bout (2009). Uniform exciton fluorescence from individual molecular nanotubes immobilized on solid substrates. *Nature Nanotechnology 4*(10), 658–663. [page 5]

Erni, R., M. D. Rossell, C. Kisielowski, and U. Dahmen (2009). Atomic-resolution imaging with a sub-50-pm electron probe. *Physical Review Letters 102*(9), 096101. [page 3]

Fei, Z., A. S. Rodin, G. O. Andreev, W. Bao, A. S. McLeod, M. Wagner, L. M. Zhang, Z. Zhao, M. Thiemens, G. Dominguez, M. M. Fogler, A. H. C. Neto, C. N. Lau, F. Keilmann, and D. N. Basov (2012). Gate-tuning of graphene plasmons revealed by infrared nano-imaging. *Nature 487*(7405), 82–85. [page 83]

Fei, Z., A. S. Rodin, W. Gannett, S. Dai, W. Regan, M. Wagner, M. K. Liu, A. S. McLeod, G. Dominguez, M. Thiemens, A. H. C. Neto, F. Keilmann, A. Zettl, R. Hillenbrand, M. M. Fogler, and D. N. Basov (2013). Electronic and plasmonic phenomena at graphene grain boundaries. *Nature Nanotechnology 8*(11), 821–825. [page 83, 94]

Gao, L., J. R. Guest, and N. P. Guisinger (2010). Epitaxial graphene on Cu(111). *Nano Letters 10*(9), 3512–3516. [page 92]

Geim, A. K. and K. S. Novoselov (2007). The rise of graphene. *Nature Materials 6*(3), 183–191. [page xxv, 81, 82]

Gleyzes, P., A. Boccara, and R. Bachelot (1995). Near field optical microscopy using a metallic vibrating tip. *Ultramicroscopy 57*(2-3), 318–322. [page 5]

Glezer, E. N., M. Milosavljevic, L. Huang, R. J. Finlay, T.-H. Her, J. P. Callan, and E. Mazur (1996). Three-dimensional optical storage inside transparentmaterials. *Optics Letters 21*(24), 2023–2025. [page 105]

Goodman, J. (2004). *Introduction to Fourier Optics* (3rd ed.). Englewood, Colo: Roberts and Company Publishers. [page xxxi, 8, 10]

Griffiths, D. J. (2012). *Introduction to Electrodynamics* (4th ed.). Boston: Addison-Wesley. [page 54]

Havener, R. W., S.-Y. Ju, L. Brown, Z. Wang, M. Wojcik, C. S. Ruiz-Vargas, and J. Park (2012). High-throughput graphene imaging on arbitrary substrates with widefield raman spectroscopy. *ACS Nano 6*(1), 373–380. [page 91]

Hayazawa, N., Y. Inouye, Z. Sekkat, and S. Kawata (2000). Metallized tip amplification of near-field raman scattering. *Optics Communications 183*(1-4), 333–336. [page 5]

Hillenbrand, R. and F. Keilmann (2000). Complex optical constants on a subwavelength scale. *Physical Review Letters 85*(14), 3029. [page 15]

Huang, P. Y., C. S. Ruiz-Vargas, A. M. v. d. Zande, W. S. Whitney, M. P. Levendorf, J. W. Kevek, S. Garg, J. S. Alden, C. J. Hustedt, Y. Zhu, J. Park, P. L. McEuen, and D. A. Muller (2011). Grains and grain boundaries in single-layer graphene atomic patchwork quilts. *Nature 469*(7330), 389–392. [page 92]

Iijima, S. (1991). Helical microtubules of graphitic carbon. *Nature 354*(6348), 56–58. [page 81, 82]

Kanehira, S., K. Miura, and K. Hirao (2008). Ion exchange in glass using femtosecond laser irradiation. *Applied Physics Letters 93*(2), 023112. [page 106]

Karrai, K. and R. D. Grober (1995). Piezoelectric tip-sample distance control for near field optical microscopes. *Applied Physics Letters 66*(14), 1842–1844. [page 5, 19, 20, 36]

Kasarova, S. N., N. G. Sultanova, C. D. Ivanov, and I. D. Nikolov (2007). Analysis of the dispersion of optical plastic materials. *Optical Materials 29*(11), 1481–1490. [page 74]

Katsnelson, M. I. (2012). *Graphene: Carbon in Two Dimensions* (1st ed.). New York: Cambridge University Press. [page 86]

Kawata, S., Y. Inouye, and T. Sugiura (1994). Near-field scanning optical microscope with a laser trapped probe. *Japanese Journal of Applied Physics 33*, L1725–L1727. [page 5]

Kihm, H.-w., Q. H. Kihm, D. S. Kim, K. J. Ahn, and J. H. Kang (2010). Phase-sensitive imaging of diffracted light by single nanoslits: measurements from near to far field. *Optics Express 18*(15), 15725–15731. [page 15]

Kim, K., Z. Lee, W. Regan, C. Kisielowski, M. F. Crommie, and A. Zettl (2011). Grain boundary mapping in polycrystalline graphene. *ACS Nano 5*(3), 2142–2146. [page 92]

Kim, K. S., Y. Zhao, H. Jang, S. Y. Lee, J. M. Kim, K. S. Kim, J.-H. Ahn, P. Kim, J.-Y. Choi, and B. H. Hong (2009). Large-scale pattern growth of graphene films for stretchable transparent electrodes. *Nature 457*(7230), 706–710. [page 91]

Kim, T., R. Zhou, L. Goddard, and G. Popescu (2014). Breakthroughs in photonics 2013: Quantitative phase imaging: Metrology meets biology. *IEEE Photonics Journal 6*(2), 1–9. [page 15]

Kinzel, E. C., J. C. Ginn, R. L. Olmon, D. J. Shelton, B. A. Lail, I. Brener, M. B. Sinclair, M. B. Raschke, and G. D. Boreman (2012). Phase resolved near-field mode imaging for the design of frequency-selective surfaces. *Optics Express 20*(11), 11986. [page 15]

Kroto, H. W., J. R. Heath, S. C. O'Brien, R. F. Curl, and R. E. Smalley (1985). C60: Buckminsterfullerene. *Nature 318*(6042), 162–163. [page 81]

Larentis, S., B. Fallahazad, and E. Tutuc (2012). Field-effect transistors and intrinsic mobility in ultra-thin $MoSe_2$ layers. *Applied Physics Letters 101*(22), 223104. [page 83]

Lee, C., X. Wei, J. W. Kysar, and J. Hone (2008). Measurement of the elastic properties and intrinsic strength of monolayer graphene. *Science 321*(5887), 385–388. [page 83]

Lee, C., H. Yan, L. E. Brus, T. F. Heinz, J. Hone, and S. Ryu (2010). Anomalous lattice vibrations of single- and few-layer $MoS_2$. *ACS Nano 4*(5), 2695–2700. [page 83]

Lee, K. (2013). *Measurement of Photoacoustic Signals from Nanostructures Using a High-Resolution Photoacoustic Microscope*. Ph. D. thesis, Yonsei University. [page xxxi, 25, 32]

Lewis, A., M. Isaacson, A. Harootunian, and A. Muray (1984). Development of a 500 Å spatial resolution light microscope: I. light is efficiently transmitted through $\lambda/16$ diameter apertures. *Ultramicroscopy 13*(3), 227–231. [page 4]

Li, P. and I. Appelbaum (2014). Electrons and holes in phosphorene. *Physical Review B 90*(11), 115439. [page 83]

Li, X., W. Cai, J. An, S. Kim, J. Nah, D. Yang, R. Piner, A. Velamakanni, I. Jung, E. Tutuc, S. K. Banerjee, L. Colombo, and R. S. Ruoff (2009). Large-area synthesis of high-quality and uniform graphene films on copper foils. *Science 324*(5932), 1312–1314. [page 91]

Li, X., G. Zhang, X. Bai, X. Sun, X. Wang, E. Wang, and H. Dai (2008). Highly conducting graphene sheets and langmuir–blodgett films. *Nature Nanotechnology 3*(9), 538–542. [page 91]

Li, X., Y. Zhu, W. Cai, M. Borysiak, B. Han, D. Chen, R. D. Piner, L. Colombo, and R. S. Ruoff (2009). Transfer of large-area graphene films for high-performance transparent conductive electrodes. *Nano Letters 9*(12), 4359–4363. [page 91]

Lipson, A., S. G. Lipson, and H. Lipson (2010). *Optical Physics* (4th ed.). Cambridge ; New York: Cambridge University Press. [page 6]

Liu, H., A. T. Neal, Z. Zhu, Z. Luo, X. Xu, D. Tománek, and P. D. Ye (2014). Phosphorene: An unexplored 2D semiconductor with a high hole mobility. *ACS Nano 8*(4), 4033–4041. [page 83]

Liu, Y., B. Zhu, L. Wang, J. Qiu, Y. Dai, and H. Ma (2008). Femtosecond laser induced coordination transformation and migration of ions in sodium borate glasses. *Applied Physics Letters 92*(12), 121113. [page 106]

Mak, K. F., L. Ju, F. Wang, and T. F. Heinz (2012). Optical spectroscopy of graphene: From the far infrared to the ultraviolet. *Solid State Communications 152*(15), 1341–1349. [page 83]

Mak, K. F., C. Lee, J. Hone, J. Shan, and T. F. Heinz (2010). Atomically thin $MoS_2$: A new direct-gap semiconductor. *Physical Review Letters 105*(13), 136805. [page 83, 99]

Mak, K. F., M. Y. Sfeir, Y. Wu, C. H. Lui, J. A. Misewich, and T. F. Heinz (2008). Measurement of the optical conductivity of graphene. *Physical Review Letters 101*(19), 196405. [page 83]

Malard, L. M., T. V. Alencar, A. P. M. Barboza, K. F. Mak, and A. M. de Paula (2013). Observation of intense second harmonic generation from $MoS_2$ atomic crystals. *Physical Review B 87*(20), 201401. [page 83]

Malmqvist, L. and H. M. Hertz (1992). Trapped particle optical microscopy. *Optics Communications 94*(1-3), 19–24. [page 5]

Maurel, C., T. Cardinal, M. Bellec, L. Canioni, B. Bousquet, M. Treguer, J. J. Videau, J. Choi, and M. Richardson (2009). Luminescence properties of silver zinc phosphate glasses following different irradiations. *Journal of Luminescence 129*(12), 1514–1518. [page 114, 122]

McCann, E. (2012). Electronic properties of monolayer and bilayer graphene. In H. Raza (Ed.), *Graphene Nanoelectronics*, NanoScience and Technology, pp. 237–275. Springer Berlin Heidelberg. [page 86]

Minovich, A., A. E. Klein, N. Janunts, T. Pertsch, D. N. Neshev, and Y. S. Kivshar (2011). Generation and near-field imaging of airy surface plasmons. *Physical Review Letters 107*(11), 116802. [page 5]

Miura, K., J. Qiu, H. Inouye, T. Mitsuyu, and K. Hirao (1997). Photowritten optical waveguides in various glasses with ultrashort pulse laser. *Applied Physics Letters 71*(23), 3329–3331. [page 105]

Miura, K., J. Qiu, T. Mitsuyu, and K. Hirao (2000). Space-selective growth of frequency-conversion crystals in glasses with ultrashort infrared laser pulses. *Optics Letters 25*(6), 408–410. [page 106]

Molina-Sánchez, A. and L. Wirtz (2011). Phonons in single-layer and few-layer $MoS_2$ and $WS_2$. *Physical Review B 84*(15), 155413. [page 83]

Morozov, S. V., K. S. Novoselov, M. I. Katsnelson, F. Schedin, D. C. Elias, J. A. Jaszczak, and A. K. Geim (2008). Giant intrinsic carrier mobilities in graphene and its bilayer. *Physical Review Letters 100*(1), 016602. [page 83]

Müller, D. J. and Y. F. Dufrêne (2011). Force nanoscopy of living cells. *Current Biology 21*(6), R212–R216. [page 5]

Nair, R. R., P. Blake, A. N. Grigorenko, K. S. Novoselov, T. J. Booth, T. Stauber, N. M. R. Peres, and A. K. Geim (2008). Fine structure constant defines visual transparency of graphene. *Science 320*(5881), 1308–1308. [page 83, 92, 94]

Novoselov, K. S., A. K. Geim, S. V. Morozov, D. Jiang, Y. Zhang, S. V. Dubonos, I. V. Grigorieva, and A. A. Firsov (2004). Electric field effect in atomically thin carbon films. *Science 306*(5696), 666–669. [page 81, 91]

Novotny, L. (2007). The history of near-field optics. In E. Wolf (Ed.), *Progress in Optics*, Volume 50, pp. 137–184. Elsevier. [page 2]

Palik, E. D. (1997). *Handbook of Optical Constants of Solids* (1st ed.). San Diego: Academic Press. [page 65]

Papon, G., N. Marquestaut, Y. Petit, A. Royon, M. Dussauze, V. Rodriguez, T. Cardinal, and L. Canioni (2014). Femtosecond single-beam direct laser poling of stable and efficient second-order nonlinear optical properties in glass. *Journal of Applied Physics 115*(11), 113103. [page 125]

Papon, G., Y. Petit, N. Marquestaut, A. Royon, M. Dussauze, V. Rodriguez, T. Cardinal, and L. Canioni (2013). Fluorescence and second-harmonic generation correlative microscopy to probe space charge separation and silver cluster stabilization during direct laser writing in a tailored silver-containing glass. *Optical Materials Express 3*(11), 1855–1861. [page xxvi, 107, 108, 109, 125, 144]

Piazza, Z. A., H.-S. Hu, W.-L. Li, Y.-F. Zhao, J. Li, and L.-S. Wang (2014). Planar hexagonal B36 as a potential basis for extended single-atom layer boron sheets. *Nature Communications 5*. [page 83]

Pohl, D. W., W. Denk, and M. Lanz (1984). Optical stethoscopy: Image recording with resolution $\lambda/20$. *Applied Physics Letters 44*(7), 651–653. [page 4]

Polini, M., R. Asgari, G. Borghi, Y. Barlas, T. Pereg-Barnea, and A. H. MacDonald (2008). Plasmons and the spectral function of graphene. *Physical Review B 77*(8), 081411. [page 83]

Popescu, G., L. P. Deflores, J. C. Vaughan, K. Badizadegan, H. Iwai, R. R. Dasari, and M. S. Feld (2004). Fourier phase microscopy for investigation of biological structuresand dynamics. *Optics Letters 29*(21), 2503–2505. [page 15]

Radisavljevic, B., A. Radenovic, J. Brivio, V. Giacometti, and A. Kis (2011). Single-layer $MoS_2$ transistors. *Nature Nanotechnology 6*(3), 147–150. [page xxv, 83, 84]

Ramakrishna Matte, H. S. S., A. Gomathi, A. Manna, D. Late, R. Datta, S. Pati, and C. N. R. Rao (2010). $MoS_2$ and $WS_2$ analogues of graphene. *Angewandte Chemie 122*(24), 4153–4156. [page 83]

Rasool, H. I., E. B. Song, M. Mecklenburg, B. C. Regan, K. L. Wang, B. H. Weiller, and J. K. Gimzewski (2011). Atomic-scale characterization of graphene grown on copper (100) single crystals. *Journal of the American Chemical Society 133*(32), 12536–12543. [page 92]

Reddick, R., R. Warmack, and T. Ferrell (1989). New form of scanning optical microscopy. *Physical Review B 39*(1), 767–770. [page 4]

Royon, A., Y. Petit, G. Papon, M. Richardson, and L. Canioni (2011). Femtosecond laser induced photochemistry in materials tailored with photosensitive agents [invited]. *Optical Materials Express 1*(5), 866–882. [page 105, 106]

Ruiter, A. G. T., J. A. Veerman, K. O. van der Werf, and N. F. van Hulst (1997). Dynamic behavior of tuning fork shear-force feedback. *Applied Physics Letters 71*(1), 28–30. [page 5, 20, 21]

Sasaki, Y. and H. Sasaki (2000). Heterodyne detection for the extraction of the probe-scattering signal in scattering-type scanning near-field optical microscope. *Japanese Journal of Applied Physics 39*(Part 2, No. 4A), L321–L323. [page 15]

Schermelleh, L., R. Heintzmann, and H. Leonhardt (2010). A guide to super-resolution fluorescence microscopy. *The Journal of Cell Biology 190*(2), 165–175. [page 3]

Schnell, M., A. Garcia-Etxarri, A. J. Huber, K. B. Crozier, A. Borisov, J. Aizpurua, and R. Hillenbrand (2010). Amplitude- and phase-resolved near-field mapping of infrared antenna modes by transmission-mode scattering-type near-field microscopy. *The Journal of Physical Chemistry C 114*(16), 7341–7345. [page 15]

Shimizu, M., M. Sakakura, M. Ohnishi, Y. Shimotsuma, T. Nakaya, K. Miura, and K. Hirao (2010). Mechanism of heat-modification inside a glass after irradiation with high-repetition rate femtosecond laser pulses. *Journal of Applied Physics 108*(7), 073533. [page 105]

Smith, A. D., M. R. F. Siggel-King, G. M. Holder, A. Cricenti, M. Luce, P. Harrison, D. S. Martin, M. Surman, T. Craig, S. D. Barrett, A. Wolski, D. J. Dunning, N. R. Thompson, Y. Saveliev, D. M. Pritchard, A. Varro, S. Chattopadhyay, and P. Weightman (2013). Near-field optical microscopy with an infra-red free electron laser applied to cancer diagnosis. *Applied Physics Letters 102*(5), 053701–053701–4. [page 5]

Splendiani, A., L. Sun, Y. Zhang, T. Li, J. Kim, C.-Y. Chim, G. Galli, and F. Wang (2010). Emerging photoluminescence in monolayer $MoS_2$. *Nano Letters 10*(4), 1271–1275. [page 83, 84, 99]

Stauber, T., N. M. R. Peres, and A. K. Geim (2008). Optical conductivity of graphene in the visible region of the spectrum. *Physical Review B 78*(8), 085432. [page 83]

Sutter, P. W., J.-I. Flege, and E. A. Sutter (2008). Epitaxial graphene on ruthenium. *Nature Materials 7*(5), 406–411. [page 91]

Synge, E. H. (1928). A suggested method for extending microscopic resolution into the ultra-microscopic region. *Philosophical Magazine Series 7 6*(35), 356. [page 2]

Synge, E. H. (1932). An application of piezo-electricity to microscopy. *Philosophical Magazine Series 7 13*(83), 297. [page 2]

Taylor, M. A., J. Janousek, V. Daria, J. Knittel, B. Hage, H.-A. Bachor, and W. P. Bowen (2013). Biological measurement beyond the quantum limit. *Nature Photonics 7*(3), 229–233. [page 15]

Thongrattanasiri, S., F. H. L. Koppens, and F. J. García de Abajo (2012). Complete optical absorption in periodically patterned graphene. *Physical Review Letters 108*(4), 047401. [page 83]

Tian, J., H. Cao, W. Wu, Q. Yu, and Y. P. Chen (2011). Direct imaging of graphene edges: Atomic structure and electronic scattering. *Nano Letters 11*(9), 3663–3668. [page 94]

Toledo-Crow, R., P. C. Yang, Y. Chen, and M. Vaez-Iravani (1992). Near-field differential scanning optical microscope with atomic force regulation. *Applied Physics Letters 60*(24), 2957–2959. [page 20]

Tonndorf, P., R. Schmidt, P. Böttger, X. Zhang, J. Börner, A. Liebig, M. Albrecht, C. Kloc, O. Gordan, D. R. T. Zahn, S. Michaelis de Vasconcellos, and R. Bratschitsch (2013). Photoluminescence emission and raman response of monolayer $MoS_2$, $MoSe_2$, and $WSe_2$. *Optics Express 21*(4), 4908–4916. [page 83]

Uma Maheswari, R., S. Mononobe, H. Tatsumi, Y. Katayama, and M. Ohtsu (1996). Observation of subcellular structures of neurons by an illumination mode near-field optical microscope under an optical feedback control. *Optical Review 3*(6), A463–A467. [page 19]

Vaez-Iravani, M. and R. Toledo-Crow (1993). Phase contrast and amplitude pseudoheterodyne interference near field scanning optical microscopy. *Applied Physics Letters 62*(10), 1044–1046. [page 15]

Valaskovic, G. A., M. Holton, and G. H. Morrison (1995). Parameter control, characterization, and optimization in the fabrication of optical fiber near-field probes. *Applied Optics 34*(7), 1215–1228. [page 126]

Volder, M. F. L. D., S. H. Tawfick, R. H. Baughman, and A. J. Hart (2013). Carbon nanotubes: Present and future commercial applications. *Science 339*(6119), 535–539. [page 82]

Vázquez de Parga, A. L., F. Calleja, B. Borca, M. C. G. Passeggi, J. J. Hinarejos, F. Guinea, and R. Miranda (2008). Periodically rippled graphene: Growth and spatially resolved electronic structure. *Physical Review Letters 100*(5), 056807. [page 91]

Wallace, P. R. (1947). The band theory of graphite. *Physical Review 71*(9), 622–634. [page 86]

Wang, J. and W. Zhou (2010). Experimental investigation of focusing of gold planar plasmonic lenses. *Plasmonics 5*(4), 325–329. [page 5]

Wang, Q. H., K. Kalantar-Zadeh, A. Kis, J. N. Coleman, and M. S. Strano (2012). Electronics and optoelectronics of two-dimensional transition metal dichalcogenides. *Nature Nanotechnology 7*(11), 699–712. [page 99]

Wangsness, R. K. (1986). *Electromagnetic fields* (2nd ed.). New York: Wiley. [page 54]

Wieting, T. and J. Verble (1971). Infrared and raman studies of long-wavelength optical phonons in hexagonal $MoS_2$. *Physical Review B 3*(12), 4286–4292. [page 99]

Yazyev, O. V. and S. G. Louie (2010). Electronic transport in polycrystalline graphene. *Nature Materials 9*(10), 806–809. [page 92]

Yim, C., M. O'Brien, N. McEvoy, S. Winters, I. Mirza, J. G. Lunney, and G. S. Duesberg (2014). Investigation of the optical properties of $MoS_2$ thin films using spectroscopic ellipsometry. *Applied Physics Letters 104*(10), 103114–103114–5. [page 83]

Yin, X., Z. Ye, D. A. Chenet, Y. Ye, K. O'Brien, J. C. Hone, and X. Zhang (2014). Edge nonlinear optics on a $MoS_2$ atomic monolayer. *Science 344*(6183), 488–490. [page 83]

Yoo, J.-H., J.-H. Lee, S.-Y. Yim, S.-H. Park, M.-D. Ro, J.-H. Kim, I.-S. Park, and K. Cho (2004). Enhancement of shear-force sensitivity using asymmetric response of tuning forks for near-field scanning optical microscopy. *Optics Express 12*(19), 4467–4475. [page 31]

Yu, Q., L. A. Jauregui, W. Wu, R. Colby, J. Tian, Z. Su, H. Cao, Z. Liu, D. Pandey, D. Wei, T. F. Chung, P. Peng, N. P. Guisinger, E. A. Stach, J. Bao, S.-S. Pei, and Y. P. Chen (2011). Control and characterization of individual grains and grain boundaries in graphene grown by chemical vapour deposition. *Nature Materials 10*(6), 443–449. [page 92, 94]

Zeng, H., J. Dai, W. Yao, D. Xiao, and X. Cui (2012). Valley polarization in $MoS_2$ monolayers by optical pumping. *Nature Nanotechnology 7*(8), 490–493. [page 83]

Zenhausern, F., Y. Martin, and H. K. Wickramasinghe (1995). Scanning interferometric apertureless microscopy: Optical imaging at 10 angstrom resolution. *Science 269*(5227), 1083–1085. [page 5, 15]

Zenhausern, F., M. P. O'Boyle, and H. K. Wickramasinghe (1994). Apertureless near-field optical microscope. *Applied Physics Letters 65*(13), 1623–1625. [page 15, 19]

Zhang, Y., J. P. Small, W. V. Pontius, and P. Kim (2005). Fabrication and electric-field-dependent transport measurements of mesoscopic graphite devices. *Applied Physics Letters 86*(7), 073104. [page 91]

Zhang, Y., Y.-W. Tan, H. L. Stormer, and P. Kim (2005). Experimental observation of the quantum hall effect and berry's phase in graphene. *Nature 438*(7065), 201–204. [page 82]

Zhong, L., Z. Zhang, X. Lu, D. Huang, C. Y. Chen, R. Wang, and Z. W. Chen (2011). NSOM/QD-based fluorescence–topographic image fusion directly reveals nano-spatial peak–valley polarities of CD69 and CD71 activation molecules on cell-membrane fluctuations during t-cell activation. *Immunology Letters 140*(1–2), 44–51. [page 5]

Zhu, X., G. S. Huang, H. T. Zhou, and Y. D. Dai (1996). A novel ultrasonic resonance sample-tip distance regulation for near field optical microscopy and shear force microscopy. *Solid State Communications 98*(7), 661–664. [page 5, 20, 36]

Zoubir, A., M. Richardson, L. Canioni, A. Brocas, and L. Sarger (2005). Optical properties of infrared femtosecond laser-modified fused silica and application to waveguide fabrication. *Journal of the Optical Society of America B 22*(10), 2138–2143. [page 105]

# Appendix A

# Bessel function

Bessel functions are the canonical solutions for the Bessel's differential equation.

$$x^2 \frac{d^2y}{dx^2} + x\frac{dy}{dx} + (x^2 - n^2)y = 0 \tag{A.1}$$

The integral form of Bessel functions of the first kind $J_n$are

$$J_n(x) = \frac{1}{2\pi}\int_0^{2\pi} \exp\left[i(x\cos\theta + n\theta)\right] d\theta \tag{A.2}$$

Power series of $J_n$ are

$$J_n(x) = \left(\frac{x}{2}\right)^n \sum_{j=0}^{\infty} \frac{(-1)^j}{j!(j+n)!}\left(\frac{x}{2}\right)^{2j} \tag{A.3}$$

Integration for circular aperture which has the radius of $w$,

$$F_1(\xi) = 2\pi\int_0^w J_0(\xi a) a \mathrm{d}a = \frac{2\pi}{\xi^2}\int_0^w \xi a\, J_0(\xi a)\mathrm{d}(\xi a) \tag{A.4}$$

Integrating $x^{n+1}J_n(x)$ by using equation A.3,

$$\begin{aligned}\int_0^{\kappa} x^{n+1}J_n(x)dx &= \int_0^{\kappa} x^{n+1}\left(\frac{x}{2}\right)^n \sum_{j=0}^{\infty}\frac{(-1)^j}{j!(j+n)!}\left(\frac{x}{2}\right)^{2j}dx \\ &= \kappa^{n+1}J_{n+1}(\kappa) \qquad \text{(A.5)}\end{aligned}$$

Therefore, equation A.4 can be rewritten as,

$$F_1(\xi) = \frac{2\pi w}{\xi}J_1(\xi w) = 2\pi w^2\frac{J_1(\xi w)}{\xi w} \qquad \text{(A.6)}$$